Discovering and Understanding High Performance Materials using Density Functional Theory: Quantum Mechanical Simulations and the Consequences of Symmetry

Olivia Pavlic

Dissertation submitted
to the Eberly College of Arts and Sciences
at West Virginia University
in partial fulfilment of the requirement for the degree of

Doctor of Philosophy
in
Physics

Mikel B. Holcomb, Ph.D., Chair
Alan D. Bristow, Ph.D.
Aldo H. Romero, Ph.D.
Timothy Morgan, Ph.D.

Department of Physics and Astronomy
Morgantown, West Virginia
2023
Keywords: Lead Chalcogenide, metavalent bonding, quantum dot, infrared detectors, electron localization function, density of states, magnesium alloys, elastic properties

Abstract

Discovering and Understanding High Performance Materials using Density Functional Theory: Quantum Mechanical Simulations and the Consequences of Symmetry
Olivia Pavlic

There are two primary ways that atomic level modeling data is used: materials prediction and understanding materials properties. This dissertation work encompasses two studies, each of which explore one application. Both studies rely on the highly successful density functional theory (DFT) formalism but differ in that two different implementations of DFT are used on two different high performance materials. The first study on bulk magnesium (Mg) metal alloys explores materials prediction and relies on VASP, a commercially maintained plane-wave DFT code which has been used extensively to successfully study a wide range of materials. [1] The approach used in this first study is to 'experiment' within computational quantum mechanical simulations to improve the elastic properties of bulk Mg by altering its HCP lattice structure. We systematically study the influence of adding lithium (Li) as an alloy for two reasons: to maintain the lightweight benefits of Mg, and Li naturally occurs in a body centered cubic (BCC) crystal structure. The hypothesis is that an alloy with a more symmetric crystal structure will show improved properties, however we do not place any symmetry restrictions on the results of the structure search. We find that the addition of Li to Mg does improve the elastic properties of the resulting alloys; however it does not necessarily increase the symmetry. Five structures are found which belong to the convex hull, three of which are previously unreported. The second DFT study seeks to understand the electronic environment within lead sulfur (PbS) semiconductor nano-structures and utilizes the open-source Octopus code, designed for electron-ion dynamics in finite systems using time-dependent DFT in real time and real space and which has also been bench-marked extensively [2]. The aim of the second study is to understand at the most fundamental levels the impact reduced symmetry has on the electronic states and transitions at the level of the individual IR-light-absorbing quantum dot. We employ three toy models to isolate the impacts of reduced coordination, Pb-rich structures, and Peierls distortions. An in-depth analysis of the bonding through the charge density and electron localization function shows that the metavalent bonding observed in bulk PbS persists in the nanoscale regime. Changing the stoichiometry too far away from Pb:S = 1:1 results in the loss of semiconducting character and an overall metallic character prevails. When we place particular attention on the effects of atomic coordination, we observe enhanced electron localization clustered around the lowest coordinated atoms. Peierls distortions intensify the clustering behavior which lowers the energy of the occupied electronic states and increases the energy

of the unoccupied states as deduced from density of states plots. The change in the electron localization is substantial only for a significant amount of low-coordinated atoms. A conclusion is made with an outlook to future work.

To Butters and Bella

Acknowledgements

My PhD research has been supported by the Naval Surface Warfare Center Crane PhD Fellowship, the Naval Innovative Science and Engineering Program, and the Department of Defense SMART Scholarship. I have utilized the Super Computing System (Mountaineer, Spruce, and Thorny Flats) at West Virginia University. The work in chapter 3 used the Extreme Science and Engineering Discovery Environment (XSEDE), which is supported by National Science Foundation grant number OCI-1053575.

Atomic structure visualizations in chapters 3, 4, and 5 were generated with the open source VESTA software [3].

Plots of raw data in chapters 3, 4, and 5 were produced with matplotlib software.

Contents

List of Figures

Chapter 1

Introduction

There are many hard problems society faces today which are related to the physical objects we depend on and the materials of which they are made. Luckily for society, there are also many bright individuals developing methods and tools and using them to develop solutions to those problems. Let us focus our studies on the basic components of matter, which are connected atoms and their behavior, and we find ourselves at the intersection of three fields of research: physics, chemistry, and materials science engineering. This broad field consists of an enormous research and development complex with countless specialties and sub-specialties. Regardless of which category this work is placed under, the aim is to understand the fundamental mechanisms behind some of the most desirable properties of matter and to use this knowledge to find better ways for humans to function. To place into context the work done here, the real world problem and application of the current work is outlined. One may wonder what the probability density of finding an electron could possibly have to do with airplanes or quality control within manufacturing. Although theoretical physics approaches may seem far away from the problem, let alone the solution, exploring these quantities and understanding their behavior gives us more tools in the proverbial tool belt and better control over how we can respond to a challenge. Benefits of employing modeling and simulation software lie with the ability to predict, with fair accuracy, whether is it worth the time and resources to try something in the real world. Therefore materials modeling is fundamentally

important and beneficial to the greater research community. Integrating it into the broader research and development complex can greatly improve results while reducing the cost and time of the development process.

We will begin by considering the theoretical approach taken in this work and the computational tools employed. During this study two implementations of the highly successful density functional theory (DFT) formalism have been used: the commercial Vienna Ab initio Simulation Package (VASP) [4] [5], and the open source Octopus code [6] [7] [8] [9]. Both of these codes calculate the ground-state properties of materials at the atomic level using first principles quantum mechanical calculations. This means that the only required information inputs are the species of atom and the positions of the atoms (or crystallographic information). From there a plethora of properties can be determined, including the optimal geometric structure, the energies of the electron states and the electronic band structure, the density of electron states, the localization of the electrons, and the spacial distribution of the electron density. The benefits and challenges of these two codes will be discussed in appendix A.

There are two primary ways that atomic level modeling data is used: to predict and to understand. In the first use case there is a desired goal but unclear path forward. For example, in chapter 3 of this work, the desired goal is a magnesium alloy with cubic crystal structure. Magnesium is a very low density metal which makes it desirable for use in the automobile and aerospace industries. It naturally exhibits a hexagonal close packed structure, which gives it characteristics that are unsuitable for use as a structural material. Metals with cubic symmetry, however, show much better structural characteristics. Here we ask: is a cubic Magnesium alloy possible? A traditional method to find the answer would be to take samples of magnesium to a laboratory, combine it with various ratios of cubic metals, perform analytical surveys on the products, and see if one of the tests was successful. However, we can do effectively the same thing with atomistic modeling software much quicker and much cheaper. We can conduct many 'experiments' at the same time in digital

space, and compare all of the results to narrow down which are the best candidates to then make in reality in the laboratory.

The second use case of atomic level modeling is to understand. Again, using for example the work in chapter 4 this dissertation, researchers have observed excellent infrared (IR) light absorption in nanoscale crystalline lead sulfur (PbS), called quantum dots (QDs). The root cause of exactly what it is about these QDs that make them such great IR light absorbers is still intensely researched and debated. [10] [11] [12] [13] [14] [15] To understand how the light is absorbed and how the material responds, atomistic simulations can determine the arrangements and bonding of the atoms, the energy levels of the electrons that are most likely (because of the arrangement of the atoms) to absorb the energy of the light, and how the excited electrons are most likely to get rid of that excess energy. Once the essential processes are understood then detector architectures can be optimized to enhance the most advantageous properties.

In this dissertation magnesium (Mg) metal alloys and their applications in industry, most notably to more efficient road and space vehicles, and lead chalcogenide (PbX) semiconductor nanocrystals and their application to low Size Weight Power and Cost (SWAP-C) infrared (IR) detectors are studied in detail. In chapter 2, a brief overview of the density functional theory formalism is given along with information on the specifics of DFT calculations and approximations which are used to make them efficient. Chapter 2 also includes an introduction to the two primary tools used in conjunction with DFT: the Minima Hopping Method, which is a search algorithm interfaced with VASP; as well as the electron localization function (ELF), which is the primary analysis tool in the PbS study. Specifics about the VASP code and the Octopus code are also detailed. Chapter 3 consists of a literature review of Mg alloys and the results of the structure search. Chapter 4 gives an overview of the properties of PbX (X= S, Se, Te) and infrared detectors, followed by the results of the electronic environment study in PbS nanostructures. In chapter 5, the major findings as well as the future outlook are given. Appendix A examines the strengths

and weaknesses of using open source code.

Chapter 2

Methods

2.1 Density Functional Theory

Let us start by recognizing that a majority of material properties are a result of electron interactions and dynamics; specifically the interactions of the highest energy bound electrons which are commonly referred as the valence electrons. Typically, these electrons also have the largest orbit and are therefore the outermost electrons. In general, the greater the number of core electrons an atom has, the higher in energy the valence electrons are and the farther away from the nucleus they are. In DFT implementations, almost always, the core electrons are not explicitly treated but instead approximated using pseudopotentials - covered in more detail in the section below (section 2.1.5). Thus the analysis is on the valence electrons only.

To mathematically treat the system of valence electrons, let us start with the non-relativistic, time-independent Schrödinger equation which describes the behavior of electrons. Written in the most compact form it reads:

$$\hat{H}\Psi = E\Psi \tag{2.1}$$

Where the Hamiltonian operator $\hat{H}$, acts on the wave function Ψ to give the energy E of that state. The wave function, Ψ, is a state vector that represents the state of the system - the states of the electrons. In general, Ψ contains all the

needed information about a physical system and specifies the state at each time t; it depends on the positions and spins of the N electrons.

In this treatment we have not ignored the nucleus. All physical properties of the electrons depend parametrically on the positions of the nuclei. Since electrons are much smaller and much faster than nuclei, inside an atom we can make the Born-Oppenheimer approximation, which allows us to consider the nuclei in the atoms as frozen in space. This simplifies the calculation by allowing us to account for the nuclei as constant terms in the external potential of the electrons.

The Hamiltonian is designed to capture the characteristics of the system under investigation. To find the ground state energy it takes the form:

$$\hat{H} = \sum_{N} [\hat{T} + \hat{V}] + \sum_{N} [\hat{U}], \tag{2.2}$$

Where the sum of the kinetic energy operator $\hat{T}$, external potential energy operator $\hat{V}$, and the sum of the Coulombic interactions $\hat{U}$ between the electrons are summed over all the electrons in the system, N. As N becomes large, the equation 2.1 becomes impossible to solve due to the exponential scaling of these quantities. To overcome this problem, we turn to a different parameter of the system: the density of electrons. The operators then become functionals of the density, which itself is a function of the spatial coordinates of the electrons, although we do not need to know what those coordinates are to operate with the functional.

The following are the foundational statements of The Hohenberg-Kohn formulation of Density Functional Theory: [16]

- The ground-state density of a bound system of interacting electrons in some external potential determines the potential uniquely.
- The Hohenberg-Kohn Minimum Principle: The density which minimizes the energy of the system, for a particular external potential, is the ground-state density.

These statements lead to the Hohenberg-Kohn theorem: given a ground-state

density it is possible to calculate the corresponding ground-state wave function Ψ, and therefore all ground-state observables. The ground-state wave function must not only reproduce the ground-state density, but also minimize the energy.[17]. This theorem tells us that it is possible to find the ground-state density by minimizing the energy in equation 2.1.

With the shift to functionals of the density, n, and a mapping from the many-body problem to single particle wave functions, $\Phi[n]$, the Hamiltonian now takes the form

$$\hat{H} = \hat{T} + \hat{V} + \hat{U} = T_s[\Phi[n]] + E_{xc}[n] + V[n] + U_h[n] \tag{2.3}$$

The exact form of $\hat{T}$ is unknown, and so is broken into two pieces. To get the best description possible we calculate the parts that can be written exactly (contained in T_s) and approximate the rest (within E_{xc}).

DFT is mathematically exact, but does not explicitly account for electron-electron interactions which leaves a small, but significant, unknown term which propagates through the results. There are numerous different methods for dealing with this term, known as the exchange-correlation functional (E_{xc}), and they will be discussed in more detail in section 2.1.4 below. The exchange-correlation functional is only one of many places where approximations are made and exact accuracy is sacrificed for computational efficiency. In this dissertation, great pains have been taken to reduce the numerical errors through rigorous testing and parameter optimization. However, DFT is a first-principles method, which means that the only information needed to run a calculation is the number of atoms, the type of atoms, and the positions of the atoms or the structure of the material (crystal structure for periodic systems and atomic positions for molecules). We need this information to determine the external potential V[n].

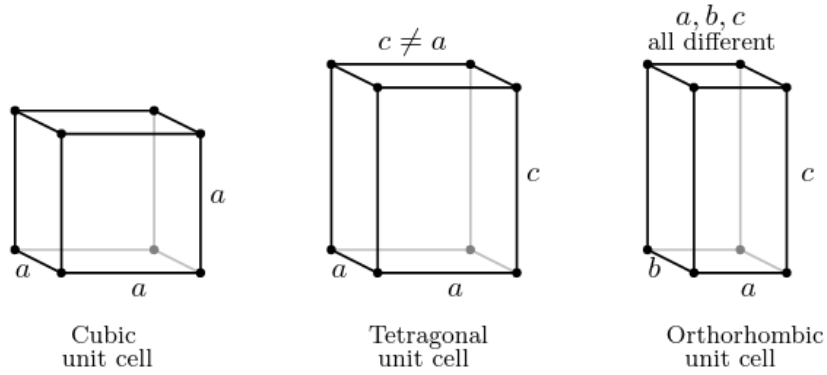

Figure 2.1: Conventional 3D unit cells for the cubic, tetragonal, and orthorhombic lattices. The a, b, and c vectors are labelled. Reproduced from [18] with permission through PLSclear

2.1.1 Periodicity, Unit Cells, and Bloch's Theorem

The materials which are studied here are crystalline: the atoms form a rigid structure and follow a specific arrangement which is repeated throughout the entire solid, similar to a pattern you might see on wallpaper but in all three dimensions. Mathematically these systems are called periodic and are constructed from a set of points, called lattice points, and are related to each other by a vector. The collection of points that have these properties are called Bravais lattices. There are 14 different Bravais lattices possible in three dimensional space. The translation operator is defined as:

$$\mathbf{t} = n_1\mathbf{t_1} + n_2\mathbf{t_2} + n_3\mathbf{t_3} \tag{2.4}$$

where n_1, n_2, and n_3 are integers and $\mathbf{t_1}, \mathbf{t_2}$, and $\mathbf{t_3}$ are the fundamental translation vectors of the lattice. This operator defines how to move from one lattice point to another lattice point and uniquely determines the structure of the lattice. However, in real atomic systems it is not necessary for there to be a Bravais lattice point at the center of every atom nor for Bravais lattice points to be occupied by atoms. A lattice can also be characterized by rotations about any single point within the lattice, and a set of such rotations are known as the point group of the lattice, a group here being the mathematical set of numbers obeying specific axioms. The

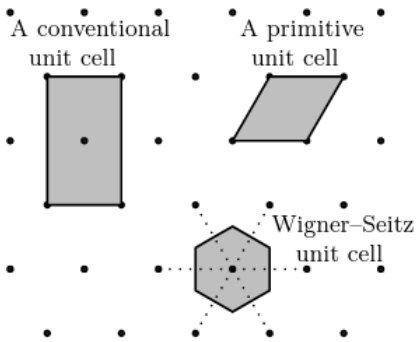

Figure 2.2: The 2D triangular lattice with three different choices of unit cell drawn and labelled. Reproduced from [18] with permission through PLSclear

translation vectors and the point group rotations together define the space group. There exist numerous notation conventions for the 230 space groups. The simplest convention, called the International number [19], numbers them from 1-230 in order of increasing symmetry. for example, space groups 195-230 are cubic.

Within a lattice, a unit cell can be defined which contains all of the unique information of the complete lattice. In other words a unit cell is an area containing one iteration of the pattern that when repeated reproduces the complete lattice. The unit cell is specified by three non-coplanar vectors, labelled a, b, and c, which form the edges of a parallelepiped (see figure 2.1). There are in principle an infinite number of choices of unit cell in a periodic system, and three choices for the 2D triangular lattice are shown in figure 2.2. Commonly it is the primitive unit cell or the conventional unit cell which are used in materials modeling. The primitive cell is constructed on the three basic vectors $\mathbf{t_1}, \mathbf{t_2}$, and $\mathbf{t_3}$, contains only one lattice point, and is the smallest single unit of the periodic arrangement. The conventional unit cell, constructed to clearly exhibit the symmetry of the lattice, has been chosen for each lattice type and is denoted in the International Tables for Crystallography.[19] Another important type of unit cell worth noting is the Wigner-Seitz cell and is constructed in the following way. Any one of the lattice points is chosen to be the Origin, O, and lines are drawn connecting this point to the nearest neighbor points. These lines are then bisected perpendicularly by planes. The area (or volume in 3D) which is contained within the planes is the Wigner-Seitz unit cell. An important

feature which is shared by periodic systems is that boundary conditions can be imposed, in other words that when the pattern is repeated there are no variations, or that a given parameter is the same at the boundaries of every unit cell.

Whichever type of unit cell is used, within the unit cell of an atomic system each electron is represented by a wave function. One school of thought for solving the Schrödinger equation is to take the real space wave functions, which are periodic and obey boundary conditions, and expand them via plane wave basis functions using Bloch's Theorem [20]:

*The wave function of a particle or quasi-particle that moves in a periodic potential V(**r**), with periodicity defined by **t** (the translation operator), can be written in the form*

$$\Psi_{\mathbf{k}}\mathbf{r} = exp(i\mathbf{k}\cdot\mathbf{r})u_{\mathbf{k}}(\mathbf{r})$$

*where $u_{\mathbf{k}(\mathbf{r})} = u_{\mathbf{k}(\mathbf{r}+\mathbf{t})}$ has the same periodicity as V(**r**) and where **k** is a vector in reciprocal space.*

This theorem says that in a periodic potential with periodic boundary conditions, the wave function can be written as a plane wave $exp(i\mathbf{k}.\mathbf{r})$ multiplied by a periodic function of the same periodicity as the lattice, $u_{\mathbf{k}}(\mathbf{r})$. Bloch's theorem is a huge advantage because all of the electrons in the entire material can be represented with just a single unit cell, and actually are defined by points in the Brillouin zone (next section). Most DFT codes specifically exploit periodicity to be able to calculate the properties of bulk materials very efficiently. However the problem has now moved from real space coordinates to reciprocal space k vectors.

2.1.2 Reciprocal Space and the Brillouin Zone

Reciprocal space, often called k-space, is a direct mapping from real space and is used extensively in x-ray and neutron diffraction as well as to express the electronic

and vibrational energy of crystals. It is defined in the following way:

$$\mathbf{g}_i \cdot \mathbf{t}_j = 2\pi\delta_{ij} \qquad (i, j = 1, 2, 3) \tag{2.5}$$

where $\mathbf{g_1}, \mathbf{g_2}$ and $\mathbf{g_3}$ are reciprocal space vectors and can be written explicitly as:

$$\mathbf{g}_1 = \frac{2\pi(\mathbf{t}_2 \times \mathbf{t}_3)}{\mathbf{t}_1 \cdot (\mathbf{t}_2 \times \mathbf{t}_3)} \tag{2.6}$$

$$\mathbf{g}_2 = \frac{2\pi(\mathbf{t}_3 \times \mathbf{t}_1)}{\mathbf{t}_2 \cdot (\mathbf{t}_3 \times \mathbf{t}_1)} \tag{2.7}$$

$$\mathbf{g}_3 = \frac{2\pi(\mathbf{t}_1 \times \mathbf{t}_2)}{\mathbf{t}_3 \cdot (\mathbf{t}_1 \times \mathbf{t}_2)} \tag{2.8}$$

and finally the position vector of any reciprocal lattice point in terms of $\mathbf{g_1}, \mathbf{g_2}$ and $\mathbf{g_3}$ can be written:

$$\mathbf{g} = n_1\mathbf{g}_1 + n_2\mathbf{g}_2 + n_3\mathbf{g}_3 \tag{2.9}$$

The $\mathbf{g}$ vectors are specific vectors tied to the particular lattice of the system. However in general a reciprocal space vector is often written:

$$\mathbf{k} = k_1\mathbf{g_1} + k_2\mathbf{g_2} + k_3\mathbf{g_3} \tag{2.10}$$

Just as $\mathbf{x}$, $\mathbf{y}$, and $\mathbf{z}$ are used for coordinates in real space, $\mathbf{k_x}, \mathbf{k_y}$, and $\mathbf{k_z}$ are coordinates in reciprocal space after the traditional labelling of reciprocal space vectors as $\mathbf{k}$ vectors due to their connection with wavenumber k. In general the reciprocal lattice can be considered as a Fourier transform of the real space lattice. [18] The Fourier transform is a set of equations that translates quantities from real space to frequency space:[21]

$$f(x) = \int F(k)e^{2\pi ikx}dk \tag{2.11}$$

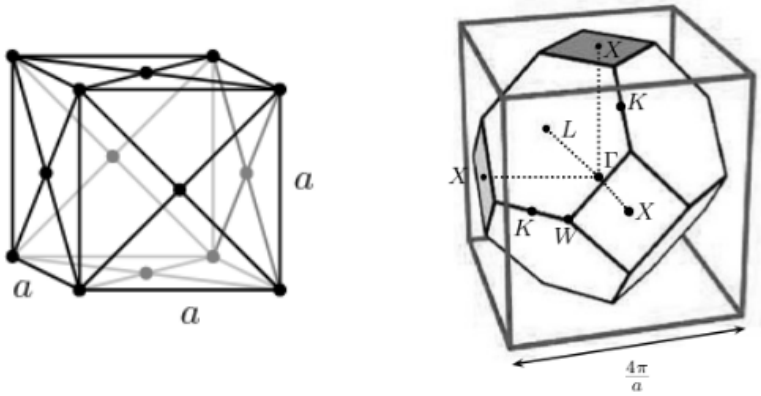

Figure 2.3: The conventional unit cell and Brillouin zone of the FCC lattice. Reproduced from [18] with permission through PLSclear

$$F(k) = \int f(x) e^{-2\pi i k x} dx \tag{2.12}$$

The wavenumber, $k = \frac{2\pi}{\lambda}$, is the magnitude of the wave vector, measured in cycles per unit distance or reciprocal meters (1/m). Similar to temporal frequency (number of waves per unit time), spatial frequency (or wave number) is the number of waves per unit distance. Reciprocal space is the space of wave vectors. The wavenumber multiplied by the reduced Plank's constant is the canonical momentum.

Analogous to how an infinite periodic crystal is reduced to the unit cell, all of reciprocal space is reduced to the Brillouin zone (BZ). Calculating it is similar to finding the Wigner-Seitz unit cell in real space, but uses the reciprocal space lattice. Many of the relevant quantities under study are discussed in terms of points in the Brillouin zone, and this is sufficient to describe the global behavior because two k-vectors are equivalent if the only difference between them is a reciprocal lattice vector $\mathbf{g}$. Most commonly the BZ is seen when describing the electronic band structure. The allowed electron energy states are calculated along a 1D path between specific points in the BZ. The end results shows a dispersion curve, or how the energy of electronic states changes as you move through k-space. It is important to carefully select the 1D path to follow high-symmetry points and lines within the BZ as these high-symmetry vectors are related to planes in real space. The vector in k-space is perpendicular to the plane in real space to which it corresponds. For example, the

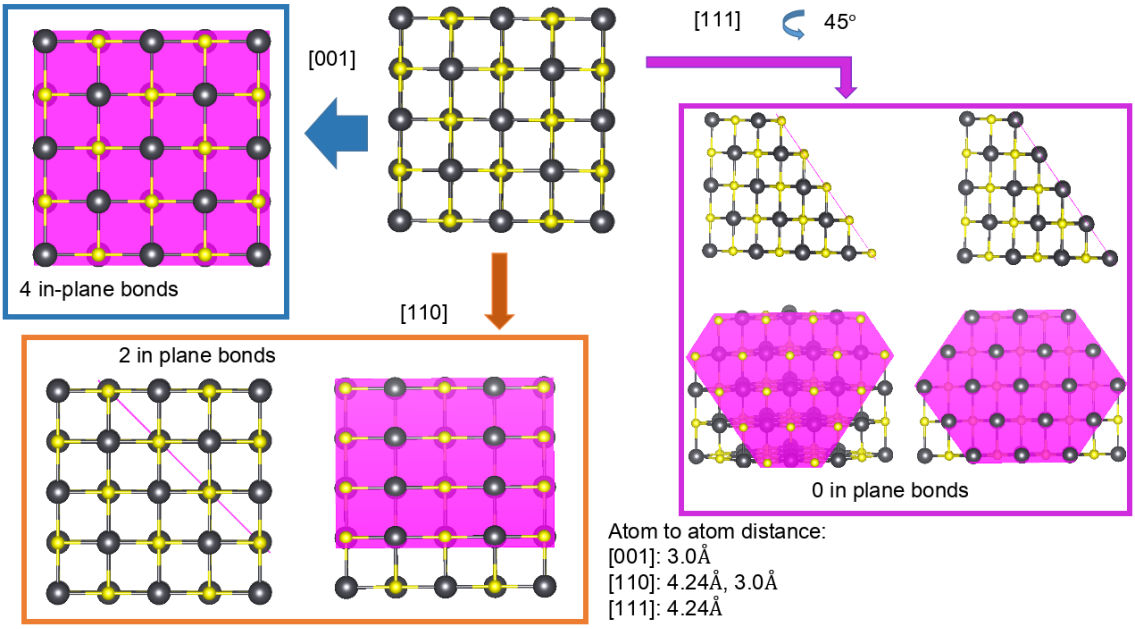

Figure 2.4: For bulk PbS which has the FCC structure, three planes are highlighted.

cubic FCC space group unit cell and BZ is shown in Figure 2.3. In k-space within the BZ, the k-vector going from Gamma to L is in the [111] direction, and corresponds to the [111] plane of atoms in real space. Examples of three of these planes and the reciprocal space directions they correspond to are shown in figure 2.4 This is an essential concept in optical phenomena because absorption of a photon or any other optical process depends crucially on the difference in energy of the electronic states and where these differences occur.

Even in the nano-scale PbX structures the atomic arrangement is crystalline; however, the structure becomes truncated and distorted. Since truncation and distortions do not allow the atoms to extend periodically, Bloch's theorem does not apply. There is however a work-around to be able to expand the wave functions in terms of plane waves. Consider two unit cells, cell A and cell B placed next to each other (see figure 2.5). If an identical arrangement of atoms are placed in the center of each cell but surrounded with sufficient empty space, when the unit cell is repeated the atoms in cell A will not interact with atoms in cell B. It is then possible to repeat the unit cell in 3 dimensions and use the plane wave method on this system. This is indeed how results for 2D, 1D and 0D structures are generated

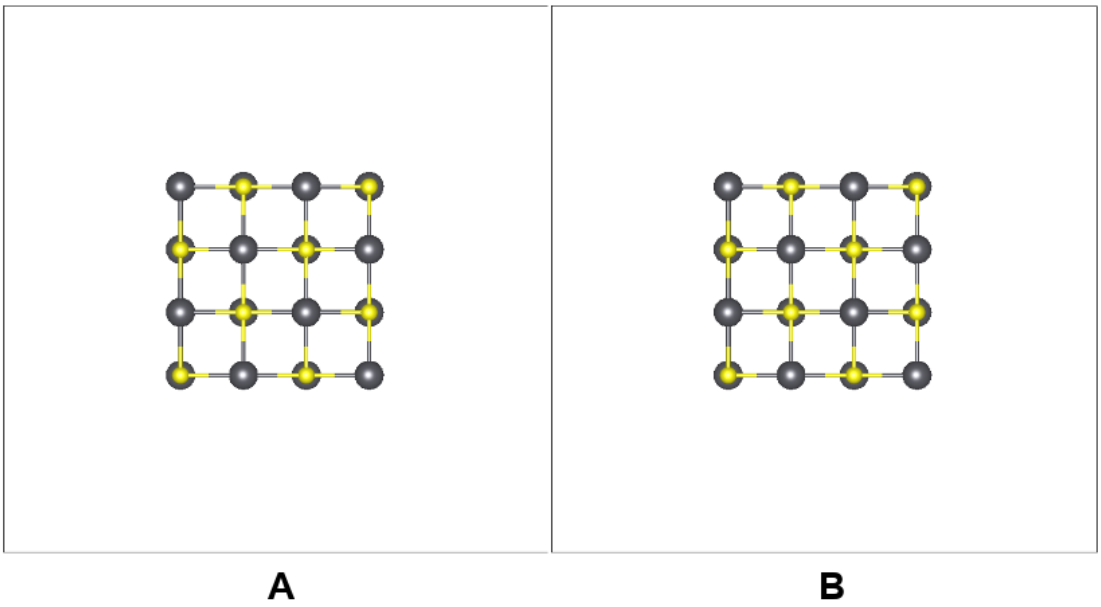

Figure 2.5: Two unit cells with empty space surrounding the atoms inside next to each other. If there is enough empty space between the atoms in different cells the atoms in cell A will not effect the atoms in cell B and the two structures are effectively isolated.

within plane-wave codes such as VASP. However it is computationally expensive and restricts the number of atoms which can be studied.

2.1.3 Grids

Grids are another theoretical tool which are ubiquitous across computational simulation packages. While both real space and reciprocal space are continuous, producing a result for every point in space is impractical. Instead the simulation space is broken up into a set of discreet grid points or a mesh, which samples the entire simulation space. In reciprocal space these are called k-points. The accuracy of the data produced from a calculation is highly dependent on the choice of grid spacing. The smaller the spacing between grid points, or equivalently the larger the number of points included in the calculation, the more accurate the results will be. However, including a larger number of points drives up the computational cost of the calculations. A method that is often implemented is to choose the grid to correspond to high symmetry points within the geometry of a rigid system. This enables the calculations to be run with fewer operations. However, it is always important to

find the optimal number of points, or the optimal grid spacing, at the beginning of a study.

In the Mg study with VASP, the mesh used is in reciprocal space. The k-points were optimized through a series of ground-state calculations. In each calculation, the number of k-points varied from a 2x2 mesh up to a 8x8 mesh to guarantee a numerical accuracy of the total energy to less than 2meV/atom. In the PbS study with Octopus, there are two parameters to optimize: the radius of the simulation space around each atom and the grid spacing. Again a series of ground-state calculations were performed, varying first the radius and then the spacing to ensure the total energy is minimized and accurate to within 0.1 eV.

2.1.4 Exchange-Correlation Functionals

The exchange and correlation functionals describe all the quantum weirdness that happens when electrons are put in a room together. There are multiple levels of approximations that give results ranging from low to high accuracy at the expense of more computationally demanding calculations. In the computational community this is referred to as the Jacob's ladder of chemical accuracy [22] (see figure 2.6).

Below the ladder in figure 2.6 is Hartree World, where electrons do not interact at all. Making this assumption can be useful in a limited number or cases, but for a vast majority of systems it is crucial to account for electron interaction on some level. On the lowest rung is the Local Density Approximation (LDA). These functionals contain terms which mimic a homogeneous electron gas of the same density of the system. LDAs have been shown to be effective for bulk metallic systems and for determining bond lengths and the ground-state geometric configuration, but because all the electrons are the same distance from each other (constant density), using LDAs often suffer from over-binding which results in incorrect electronic energy levels.

One step above the LDA are the Generalized Gradient Approximation (GGA) functionals. These functionals include terms that are dependent on the gradient of

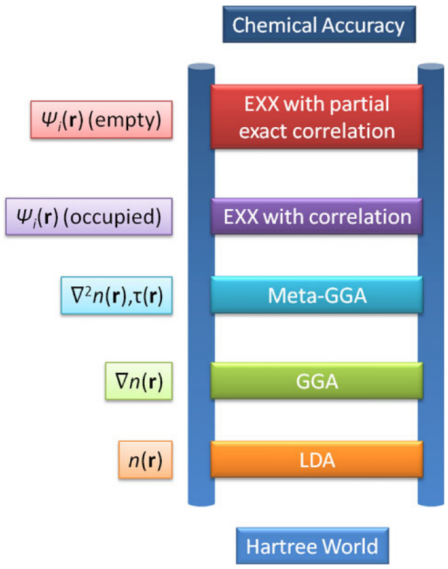

Figure 2.6: Jacob's ladder of DFT with the different approximations linking the Hartree World of Independent Electrons and the Heaven of Chemical Accuracy. [23] EXX stands for the exact exchange, n for the density, τ for the kinetic terms and Ψ for the orbitals. Notice that no comparison to computational Chemical methods is presented and only from rung 4 upwards exact exchange (i.e. Hartree-Fock form) is taken into account. [22]

the density and consequently are more computationally expensive than calculations done with LDAs. They do not over-bind as LDAs do and can sometimes over-correct and under-bind. GGAs are widely used because they give more accurate results for semiconductor systems and chemical reaction calculations. They do suffer from self-interaction errors, which come from an electron interacting with its own density, and cause excessively narrow band gaps among other problems.

The next step up on the ladder includes terms in the functionals which depend on the kinetic energy density, or ∇^2 of the density. These are called meta-GGA functionals and can make significant improvements to optical properties calculations in semiconductor systems. Unfortunately they do not provide a systematic improvement over GGA functionals for most other properties while being more computationally expensive. The next two steps up on the ladder seek to improve upon the description of the electronic behavior by combining part of the already mentioned functionals with an exact description of the exchange (EXX stands for exact exchange). Thereby named hybrid functionals, they have been shown to reliably give

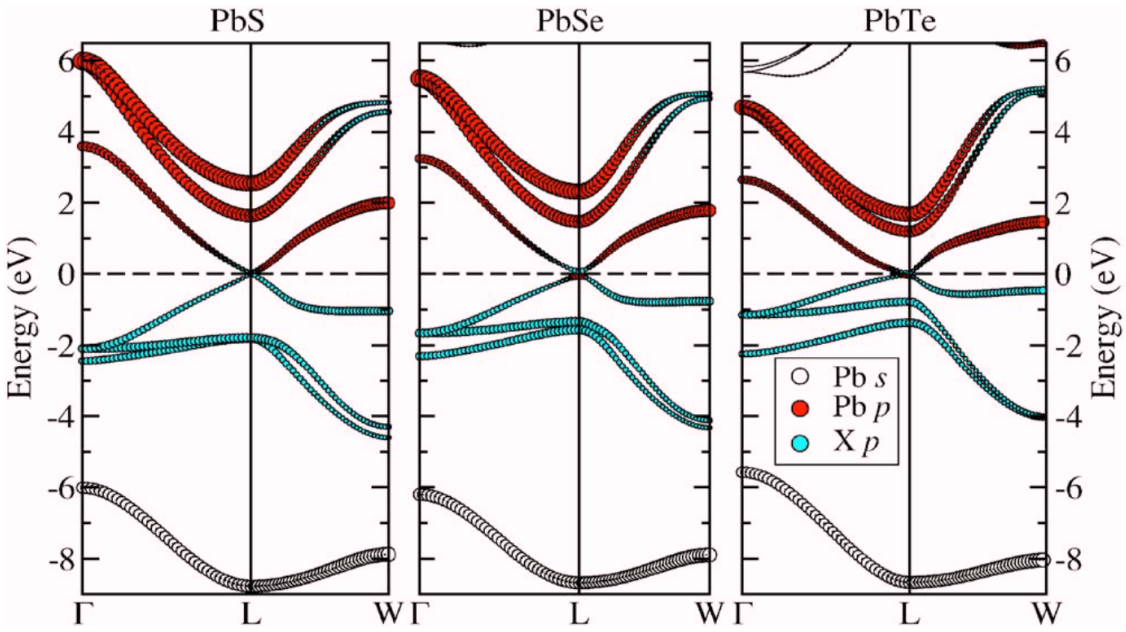

Figure 2.7: Standard DFT-PBE band structures of PbS, PbSe, and PbTe along Γ*LW* including SOC. The band character is indicated by circles, where the size correlates with the amount of Pb-s, Pb-s, and X-p characters, respectively. The Fermi level is indicated by a dashed line. Reprinted with permission from [24]

results that match very well with experimental results. However, these functionals are prohibitively expensive, as is stressed by the authors which have published studies using them. Likewise, the present author can confirm that reproducing the data of the PbS study with a hybrid functional would take more than one year of real time computing hours vs the approximately 3 months of computing time with the GGA functional.

In the PbS work presented in Chapter 4 it was necessary to perform a survey of various XC functionals that were reported in the literature to be successful for studying semiconductor systems. As the PbX family is well known for anomalous behavior, and hence being very difficult to properly describe with standard theoretical methods, what works for other semiconductors has to be examined thoroughly before accepted as right for this work.

It has been reported in the literature that standard treatments of the PbX bulk system provide a poor description of the band edges, which are of the highest importance for optical phenomena. In 2007, Hummer et. al. [24] studied the PbX system

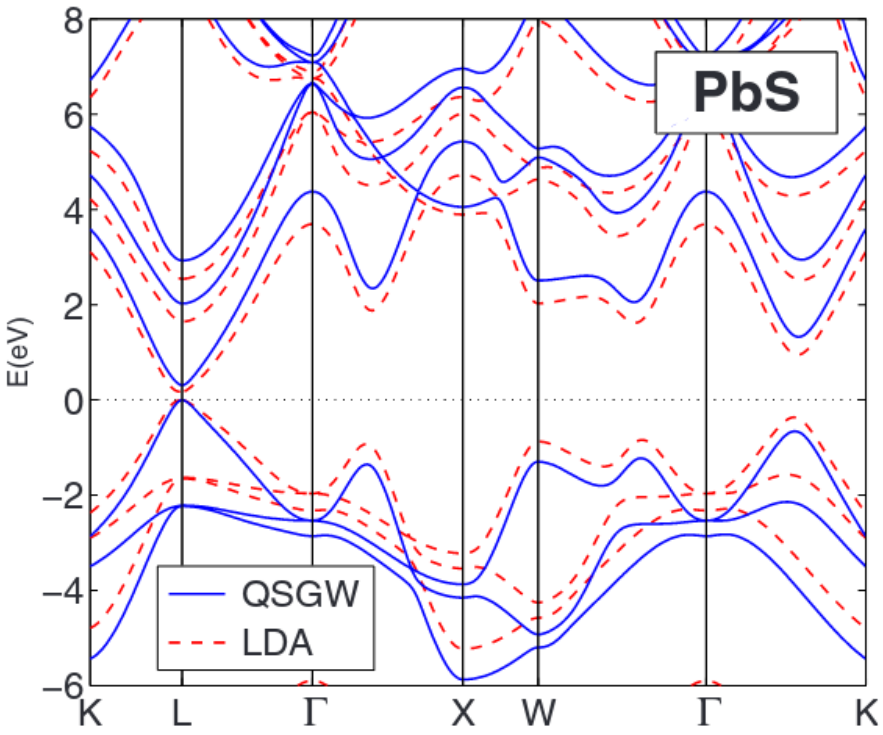

Figure 2.8: Electronic band structure of PbS calculated with LDA (dashed red line) and the quasiparticle self consistent GW approximation (QSGW, blue line). The zero of energy is placed at the valence-band maximum. Reprinted with permission from [25]

with the projector augmented wave (PAW) method and showed that when using the lowest rung exchange correlation functionals (LDA and GGA), the band gaps and effective charge-carrier masses are not correctly described including inverted bands at the band edge and therefore the calculations produce a negative band gap (figure 2.7). They used the orbital character of individual bands as evidence of the band inversion. They found significant improvement using more accurate methods such as a screened hybrid functional or the partially self-consistent GW method, but note that the computational cost is significantly higher with these two methods.

In 2010, Svane and coworkers studied the PbX electronic band structure with the quasiparticle self consistent GW (QSGW) approximation [25]. They note that the QSGW band structures show only minor differences from the LDA structures, with the major exception being the inversion of the CBM and VBM states at the band gap (figure 2.8). They cite that the group symmetry of the VBM and CBM bands has been reversed at the L point.

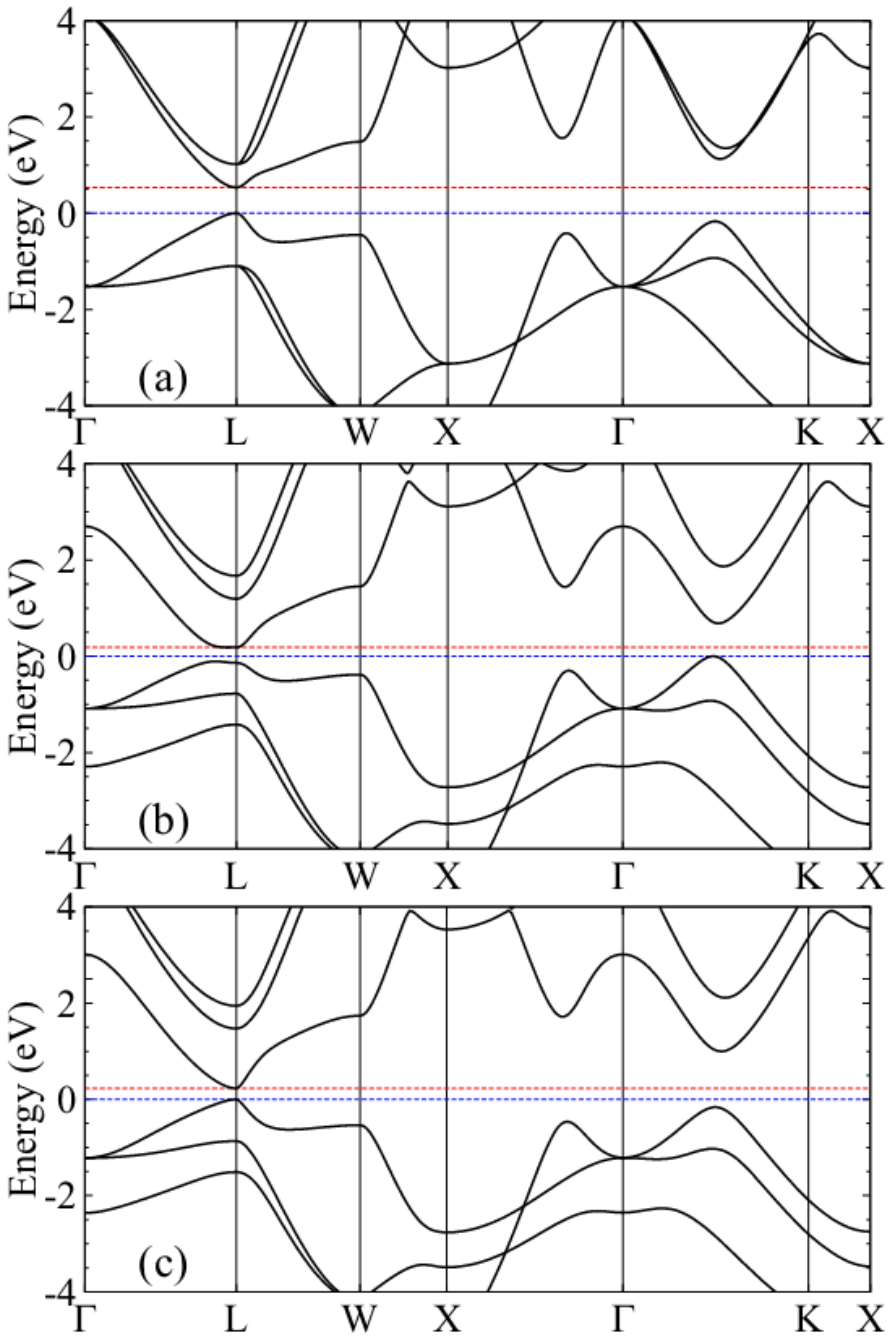

Figure 2.9: Electronic band structure of PbTe, calculated using (a) the LDA and HGH pseudopotentials excluding SOI, (b) the LDA and HGH pseudopotentials including SOI, and (c) the HSE03 hybrid functional and PAW pseudopotentials including SOI. The energies of the valence band minimum (blue dashed line) and conduction mand maximum (red dashed line) are also highlighted. Reprinted with permission from [26]

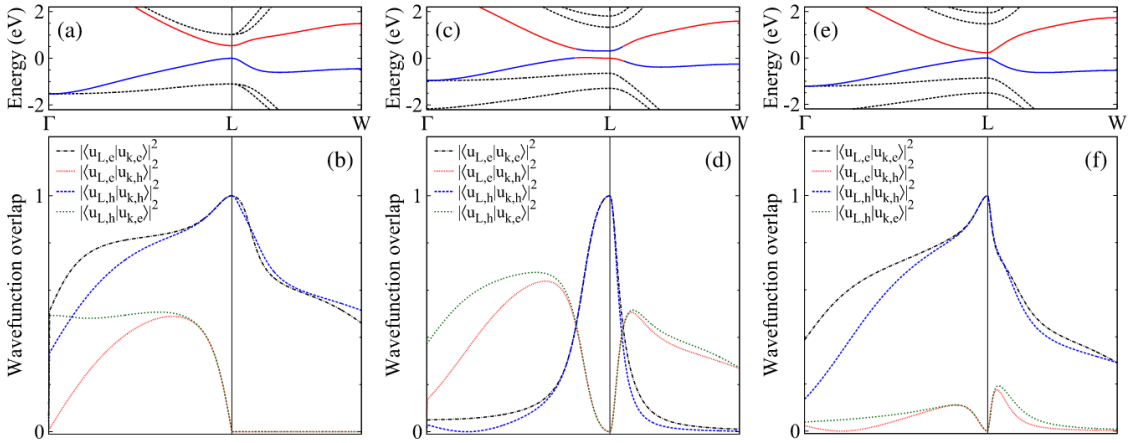

Figure 2.10: Electronic band structure of PbTe near the Fermi level at 0K along the $\Gamma - L - W$ line calculated using the functionals as outlined in figure 2.9. The bottom panels show the overlaps of the periodic part of the wave function for the lowest conduction band and highest valence band at the wave vector k with the wave function of one of these two bands at the L point. Reprinted with permission from [26]

In Murphy et. al.'s study in 2018 [26], the PAW method with LDA XC was used and results showed that band inversion only happens when spin-orbit coupling (SOC, discussed in section 2.2) is included in the calculations (figures 2.9 and 2.10). They calculate the wave function overlap of the CBM and VBM which shows the character inversion. Their results show that the character of the band states near the gap, despite the band-gap overestimation, can be correctly represented with the LDA XC but without including SOC.

2.1.5 Pseudopotentials

Beyond the mathematical formalism outlined so far, more theoretical tools go into a modern DFT calculation. To obtain a solution to Schrodinger's equation the wave function, Ψ, for each particle must be known in three dimensions. Even when using DFT, the three-dimensional wave function plays a part and puts a restriction on the ability to handle large systems because of the large number of terms required to describe all the particles involved. A way to reduce the exact information needed in the problem is to use pseudopotentials. The pseudopotential formalism separates the electrons in a system into valence electrons and core electrons. The idea is that

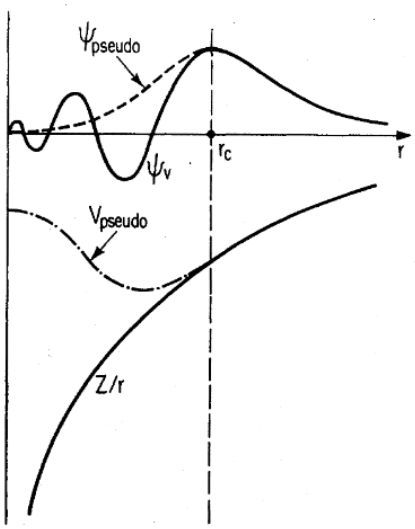

Figure 2.11: Schematic illustration of all-electron (solid lines) and pseudoelectron (dashed lines) potentials and their corresponding wave functions. The radius at which all-electron and pseudoelectron values match is designated r_c. Reproduced with permission from [27].

only the valence electrons are affected by chemical changes to the system while the core electrons remain in their atomic configuration. In the region of space close to the nucleus the exact information for the core electrons is disregarded in favor of a function that approximately reproduces the same effective potential. Figure 2.11 shows a sketch of the all-electron potential and wave function, denoted as Z/r and Ψ_V, respectively. V_{pseudo} and Ψ_{pseudo} denote the approximations of these two quantities used in the pseudopotential formalism. The region of space which is approximated is parameterized by the cutoff radius, labeled r_c in figure 2.11, and it is often required that the pseudo-expressions must match the all-electron expressions at r_c. Past the cutoff radius the valence electrons are explicitly treated. To emphasize this point, the pseudopotential must be zero past a defined radius.

There are various constraints placed on pseudopotentials: examples include separable, norm conserving, strictly local or non-local. Different constraints and methods of generating pseudopotentials effect their ability to accurately represent the physical system. There are software packages available to allow users to construct their own pseudopotentials, and online databases of pseudopotentials that are available for use. DFT packages usually include recommend sets of pseudopotentials that

have been generated and tested, or encourage the user to create their own set specific to the system under study. In this study, within the VASP software package sets of tested pseudopotentials of the ultrasoft projector augmented wave variety are provided, and so, these were the pseudopotentials used for Mg alloys. From the VASP wiki page: “Except for the 1st-row elements, all PAW potentials are designed to work reliably and accurately at an energy cutoff of roughly 250 eV." [28] While a healthy level of skepticism should be applied to any simulation result, VASP users can trust these pseudopotentials to give reasonable results without worrying too much.

The Octopus code is somewhat different in that multiple incomplete sets of pseudopotentials of different flavors are provided within the source-code package. While these potentials are provided, the Octopus developers give strong warnings against trusting them to provide accurate results. The user is informed that there are a variety of pseudopotentials available though open-source repositories and it is left to the user to decide which type and flavor is appropriate for their particular application. It is an advantage that the developers have designed the Octopus code to read many different pseudopotential file formats, however in practice not all code functionalities work with every type of ‘compatible’ pseudopotential. Following the study by Murphy in 2018 [26], the HGH LDA pseudopotentials [29] were used in the PbS study. In addition to Murphy’s study demonstrating the suitability of the HGH pseudopotentials to treat PbTe with successful representation of the band edge states, testing within the Octopus code has shown that the LDA type of pseudopotentials are the most compatible with code features.

2.2 Spin Orbit Coupling

Spin orbit coupling (SOC) or spin orbit interaction (SOI) is a change to the orbital energy levels of an electron due to the relativistic interaction of the electron’s spin magnetic moment (μ_s) with the orbital magnetic field (B) of the nucleus due to the particle’s motion [31]:

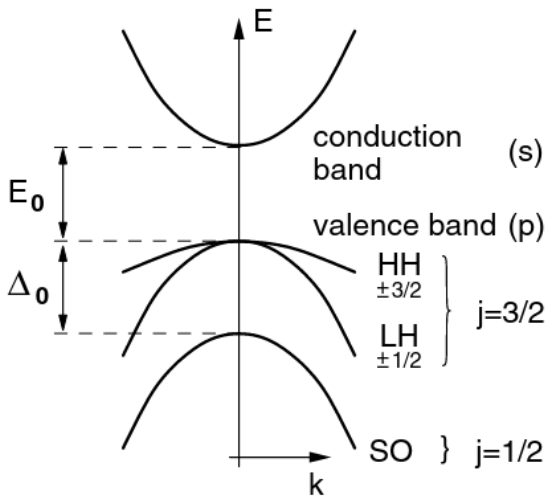

Figure 2.12: Sketch of the band structure of GaAs with SOC effects. Reproduced with permission from Springer Nature [30]

$$\hat{H}_{SO} = -\mu_s \cdot B \Rightarrow \frac{1}{2{m_e}^2 c^2} \frac{1}{r} \frac{d\hat{V}}{dr} \hat{S} \cdot \hat{L} \tag{2.13}$$

where m_e is the mass of the electron, c is the speed of light, $\hat{V}$ is the central Coulomb potential of the nucleus, $\hat{S}$ is the spin angular momentum, and $\hat{L}$ is the orbital angular momentum of the electron. It was first proposed by Thomas in 1926 [32] to explain small differences in atomic spectroscopy data. SOC effects are often referred to as the fine structure of a system. The strength of the effect is dependent on the size of the nucleus, in that the more charge the nucleus has the greater the electric field is which the electron experiences. Figure 2.12 shows the effect of SOC on the band structure of GaAs. In semiconductors like GaAs, the electron states at the valence band edge are p-like and when SOC effects are applied these states split into j=1/2 and j=3/2 states with different energies. Figure 2.2 tabulates the calculated atomic contribution to the SO band splitting in a binary semiconductor model from various atoms. Clearly Pb has a strong SOC effect and SOC terms are usually included in calculations involving this element. For example, figure 2.2 gives the SOC energy splittings at the Γ and X point found by Svane 2010 from DFT calculations in PbS, PbSe, and PbTe [25].

As was discussed in the previous section, including SOC in DFT calculations of

Be	B	C	N	O	F
0.002	0.004	0.006	0.009	0.010	0.010
Mg	Al	Si	P	S	Cl
0.01	0.024	0.044	0.08	0.09	0.09
Zn	Ga	Ge	As	Se	Br
0.10	0.18	0.29	0.43	0.48	0.49
Cd	In	Sn	Sb	Te	I
0.10	0.36	0.80	1.05	1.10	1.11
Hg	Tl	Pb			
0.5	0.9	2.0			

Table 1: Theoretical values of the atomic contribution to spin-orbit splittings in binary semiconductors from various atoms. Values are given in eV. Reproduced with permission from Springer Nature [30]

	PbS		PbSe		PbTe	
	Γ	X	Γ	X	Γ	X
QS*GW*	0.33	0.28	0.58	0.43	0.99	0.64
LDA	0.36	0.32	0.66	0.48	1.11	0.70
Expt.[a]	0.3	0.2	0.6	0.5	1.15	0.9
Expt.[b]			0.75	0.55	1.10	1.10

Table 2: Spin orbit splittings at Γ and X points for the lead chalcogenides as calculated with the QSGW approximation and with LDA. All values are in eV. Reproduced with permission from [25]

PbS leads to inverted band character at the band gap due to a compounding effect with the known overestimation of the band gap [35]. Therefore some authors have not been applying SOC. Additionally, in the reduced dimensionality systems studied here, Kane and Wise in 1997 [34] found that quantum confinement has an especially large role in the energy levels of the electrons. Figure 2.13 shows a schematic of the character of the QD levels surrounding E_f, the calculated optical transition energies superimposed on the experiment absorption spectra, and the calculated value of the HOMO-LUMO gap of PbS QDs as a function of size. Figure 2.14 shows results from a theoretical study on a spherical PbS QD picture and shows how the hole and electron levels within a PbS QD change with the diameter of the QD. The Bohr radius of PbS is approximately 18 nm, which is much larger than the typical size of QDs used in studies (1-10nm) [34][36][37]. Because of this, in small QDs, the energy level splittings in PbS and PbSe QDs are dominated by the confinement energy which is on the order of 1 eV as opposed to other effects such as exchange

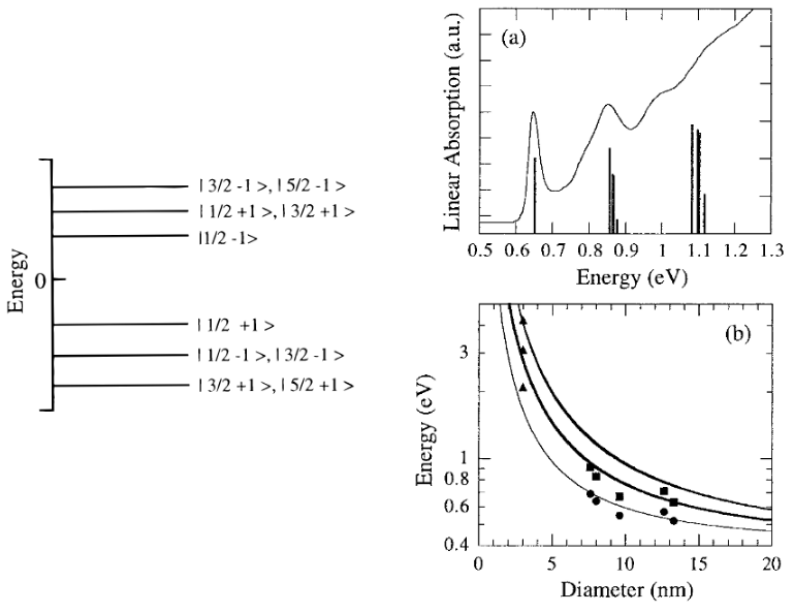

Figure 2.13: Left: general form of the first few electron and hole energy levels of PbS or PbSe QDs. The states are labeled by the quantum numbers j (total angular momentum) and π (parity): $\mid j\pi\rangle$. Right: (a) Absorption spectrum and calculated transition strengths of 8.5 nm diameter PbS QDs in oxide glass. (b) Measured and calculated exciton energies (plotted on a logarithmic scale) as a function of the size of PbS QDs. The dark lines indicate nearly degenerate transitions between the states indicated in figure at right. Reproduced with permission from [33]

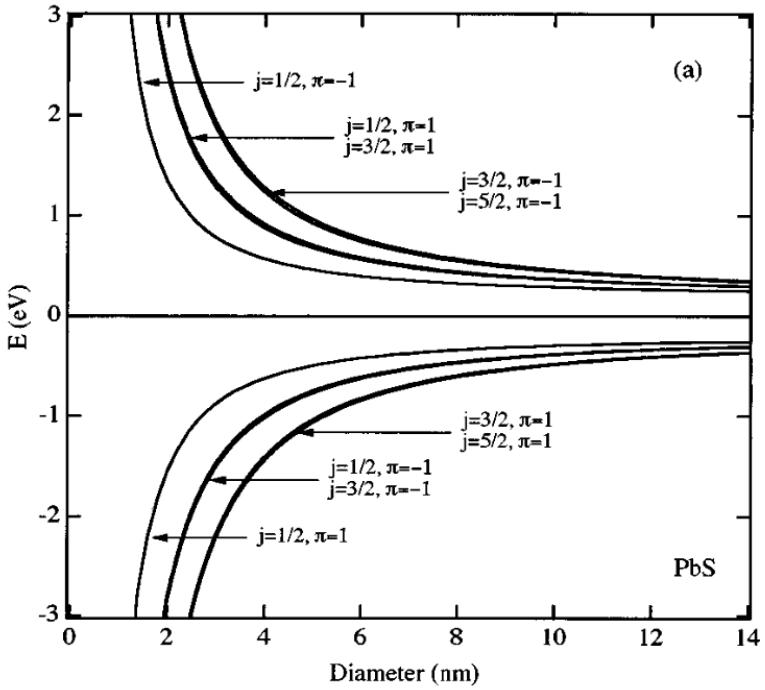

Figure 2.14: Unperturbed energy levels of conduction and valence electrons of PbS QDs. Reproduced with permission from [34]

interaction and inter-valley scattering which are less than half the magnitude of the confinement energy. Due to these considerations SOC has not be employed in the calculations in this study.

2.3 Minima Hopping Method

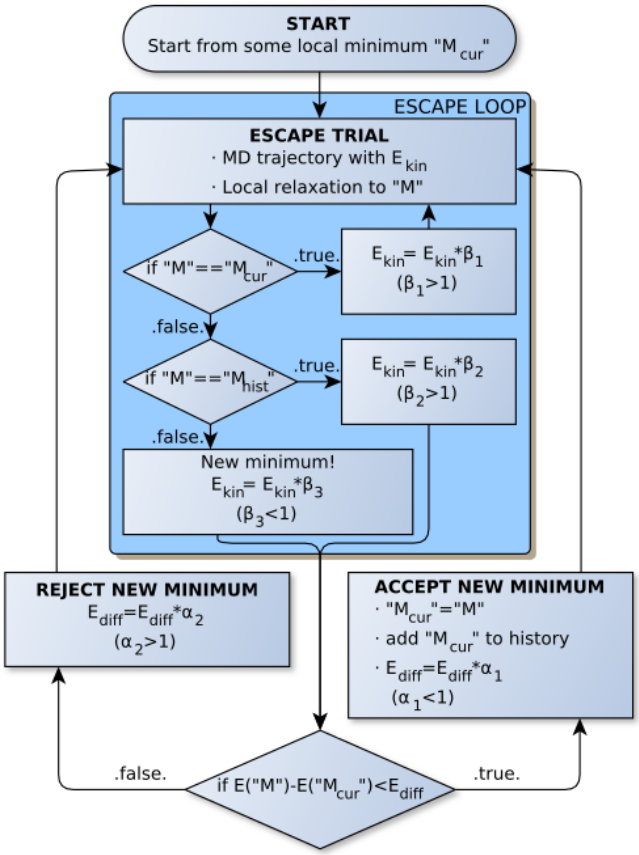

Figure 2.15: The Minima Hopping Method algorithm flowchart. The algorithm consists of two main parts, the inner part (encapsulated in blue) controls the jumps into neighboring minimum, while the outer part controls whether this minimum is accepted or rejected. [38]

For the prediction of novel alloy structures, the Minima Hopping Method (MHM) numerical technique was used [38] [39]. For a given atomic composition, this algorithm explores the potential energy surface (PES). The PES is a way to map the free energy of an atomic structure with respect to its internal degrees of freedom, or in other words the positions of the atoms. Local minima points on the PES correspond to a set of atomic coordinates which are energetically stable. The energetic order-

ing of these minima indicates the thermodynamic stability of the different phases. This dynamical algorithm effectively samples the entire potential energy surface to find the global energy minimum using temperature as the variable. The simulation starts with an arbitrary atomic configuration and quickly finds the local minima. To leave this minima, a series of consecutive short molecular dynamics simulations are used to overcome the surrounding energy barrier and 'hop' elsewhere. This allows the algorithm to visit many local minima and explore all locations on the potential energy surface. Local geometry relaxations follow each hop to identify the atomic configuration corresponding to the energy minima. The escape is made efficient by choosing the initial velocities of molecular dynamics trajectories approximately along soft mode directions, or in other words toward a direction with low curvature [39]. This method is used in conjunction with DFT to predict stable and metastable structures. The only information required is the chemical composition of the system.

2.4 Electron Localization Function and Bonding

The Electron Localization Function (ELF) is a differential scalar field in 3D space and provides a simple measure of electron localization in atomic and molecular systems. It is a powerful tool to analyze the spatial arrangement of electrons within a material, and gives information such as the type of bonds present. Utilizing the ELF alone has been proven sufficient to identify bonds and lone pairs in molecules and solids as well as be of use in characterizing material properties. [40] [41] [42] [43] The ELF is denoted $n(r)$ and defined in the following way:

$$n(r) = \frac{1}{1 + \chi(r)}$$

where $\chi(r)$ is the ratio of electron localization $D(r)$ with respect to the uniform electron gas $D_h(r)$:

$$\chi(r) = \frac{D(r)}{D_h(r)} \tag{2.14}$$

ELF value	What it means
> 0.7	Localized electrons, core regions, bonding, lone pairs
0.2 < n < 0.7	Characteristic of metallic bonding
0.5	Value of the free electron gas

Table 3: Possible ELF values divided into three regions.

$$D(r) = \frac{1}{2}\sum |\nabla\psi(r)|^2 - \frac{1}{8}\frac{|\nabla p(r)|}{p(r)} \tag{2.15}$$

$$D_h(r) = \frac{3}{10}(3\pi^2)^{2/3}p(r)^{5/3} \tag{2.16}$$

The ELF is calculated as a ratio between the electron localization – based on the electron density - and the uniform electron gas. In a practical sense it is the probability density of finding another electron near the reference electron with the same spin [43].

Table 3 lists how the value of the ELF is used to analyze the electron localization. The ELF takes a value between 0 and 1, with 0 indicating no localization and 1 indicating the presence of electrons in the form of a lone pair, a covalent bond, or electrons bound to a nucleus. A value between 0.2 and 0.7 is indicative of metallic bonding, and above 0.7 indicates a high level of localization. Values below 0.2 indicate a low probability of electrons being in that region of space with most dipole induced bonds having ELF values of less than 0.1 between atoms.

As outlined in Koumpouras 2020 [43] and summarized in table 4, there are defining features of the ELF for the regions between atoms which indicate what type of bonding exists in that region. Bond types are separated into two broad categories, chemical bonds defined by shared electron bonding and physical bonds defined by closed shell or bonds that do not share electrons (see table 4).

Within the chemical bonding category are covalent bonding and metallic bonding. Covalent bonds consist of usually 2 electrons shared between a pair of atoms and always have what is called a bond attractor, a maximum of the ELF that is not

Bond	Type of Bond	Electron sharing?	Common Characteristic	Localization Window
Covalent	chemical	yes	Always one bond attractor; non-nuclear maxima present in the interaction region	large
Metallic	chemical	yes	ELF basins are big and extended with uniform localization connecting the atoms; smoothness and almost constant ELF in interaction regions	narrow
Ionic	physical	unshared/close -shell	Very low values of ELF in the region between nuclei (below 0.01); distorted areas of high localization, contraction of ELF around ion	none
Van der Walls (strong and normal)	physical	unshared/close -shell	Strong: low but existing ELF at the interaction minimum Normal: n very close to 0 at the minimum (similar to ionic), contraction of electron density of each layer; no permanent dipole moments in constituent atoms/molecules	large
Permanent dipole moments/bond dipoles (hydrogen)	physical	unshared/close -shelled	Contractions of the individual ELF basins on each side of the interaction region; a sharp V shaped minimum in-between; a considerable value of n (above 0.1)	large

Table 4: Different bonding types and properties of those bonds.

Localization window: difference between maximum ELF value and the first order saddle point [quantifies smoothness of the ELF along the bond axis]

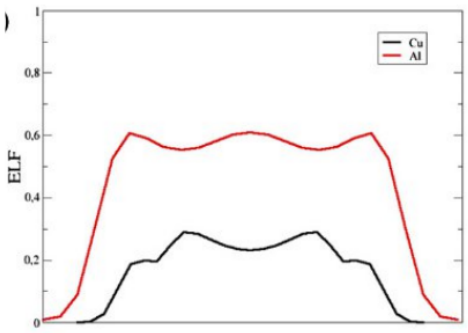

Figure 2.16: The ELF profile of the interaction regions between neighboring atoms of Cu (black) and Al (red) demonstrating the concept of localization window. [43]

an atomic nucleus. Metallic bonds consist of delocalized electrons shared between all atoms and exhibit little variation in the amplitude of the ELF value in the region between atoms. This almost constant value of the ELF between atoms is quantified by the concept of the localization window. Shown in the metallic example in figure 2.16, the localization window describes the difference between the maximum and minimum value of the ELF in the region between atoms.

In the physical bond category are ionic bonding, Van der Walls bonding, dipole induced bonds called permanent dipole bonds, and hydrogen bonds. These unshared electron bonds have very low values of ELF in the regions between atoms, usually much less than 0.2 but sometimes as high as 0.3 for hydrogen bonds. Van der Walls

bonding is a special case in that it is always present to some degree between atoms that are close to each other. However being the weakest type of atomic interaction it is typically negligible unless no other electronic interaction is taking place.

Due to the way the ELF is defined, it gives no information about how many electrons are in a particular region of space. It does provide a measure of how likely an electron is to spatially occupy that region and a measure of the kinetic energy of that electron. For that reason, when studying the ELF we will also study the charge density in the same regions to identify the presence of electrons.

Chapter 3

LiMg Study

3.1 Introduction

The search for cost-effective and lightweight structural materials for ground and air vehicles has led researchers to investigate the properties of Magnesium (Mg). Ongoing research since the 1950's has found Mg to be naturally abundant, recyclable, cast-able, weldable, and to possess high specific strength. [44] [45] [46] [47] [48] [49] [50] [51] The most attractive property however is the low density of 1.74g/cm^3 [52] which could minimize the environmental impacts of automobiles and airplanes.

Currently Mg is not widely used as a structural material because at room temperature it crystallizes into the hexagonal close packed (HCP) lattice structure which is inherently brittle. Features of the HCP structure are shown in figure 3.1. Most notably the HCP structure has two equivalent lattice constants which are short while the third is long ($a = b, c$) and two alternating stacked planes of atoms, A and B. The shorter distance between atoms within a plane compared to the distance between the A and B planes cause the structure to deform anisotropically when an external force is applied which leads to brittleness.

To investigate further what causes a material to be ductile instead of brittle, we turn to understanding the details of deformations. The way a solid responds to forces is generally broken into two regimes: small forces which cause non-permanent elastic deformations and large forces which cause permanent plastic deformations.

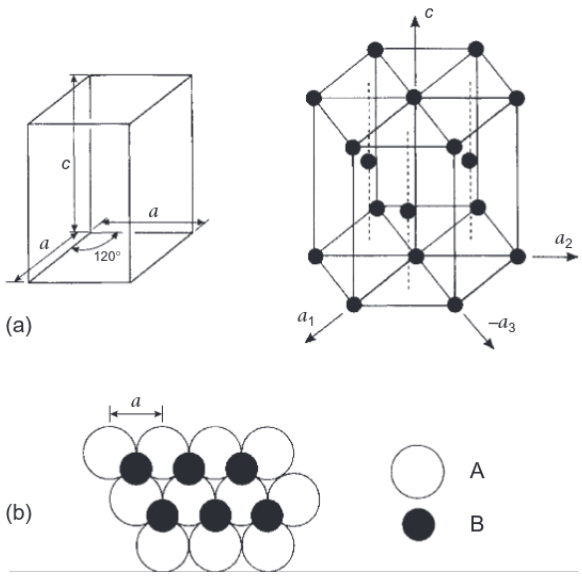

Figure 3.1: Close-packed hexagonal structure: (a) the unit cell of the lattice and the hexagonal cell showing the arrangement of atoms, (b) *ABAB*... stacking sequence of the atomic planes perpendicular to the *c* axis. Reproduced with permission from [53]

The value of force which makes it small or large is material dependent.

For Mg in particular, plastic deformations occur at low forces. At the atomic level, plastic deformations occur most often along slip planes. Slip planes are identified when one plane of atoms slides over another plane of atoms in a direction parallel to one another[53]. Figure 3.2 shows three common slip planes in HPC structures. In Mg, at low pressures there is slip along only the basal planes while the pyramidal and prism planes do not activate until higher stresses [54]. Because there is one preferred slip plane which deforms at low energies, the plastic deforma-

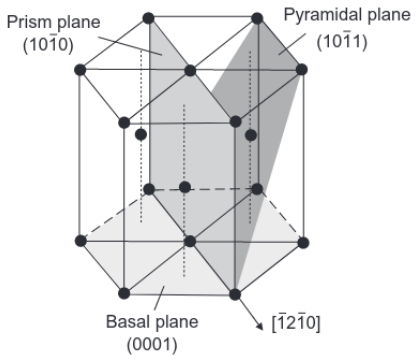

Figure 3.2: Planes in an hexagonal lattice with common $[\bar{1}2\bar{1}0]$ direction. Reproduced with permission from [53]

tion is anisotropic and Mg is brittle. Changing the crystal structure symmetry away from HCP, with two short and one long lattice constants, to a more cubic structure with more symmetry and more competition between deformation mechanisms would change the force required for plastic deformation and improve the ductility of the material.

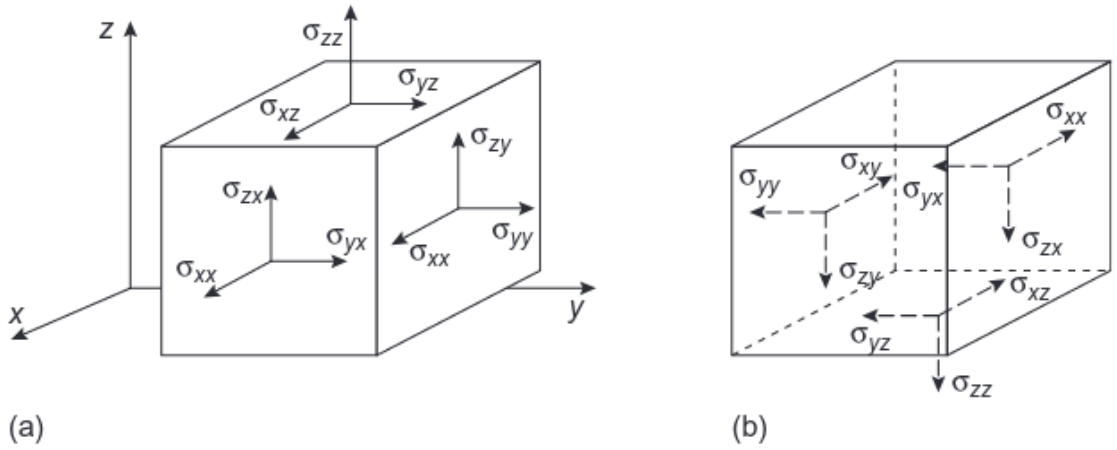

Figure 3.3: Components of stress acting on (a) the top and front faces and (b) the bottom and back faces of a cubic volume. Reproduced with permission from [53]

We can then turn our focus on the elastic regime, which will play a larger part in more symmetric materials. Elastic deformations occur at small amounts of applied force, before a plastic deformation. The force is applied via stresses on the surface of a volume of material. Here we will consider a cube with faces aligned in the x, y, and z directions (see figure 3.3). Stress, σ_{ij}, is the force per unit area of surface, usually measured in pascals (1 pascal = 1 N/m^2). The indices i, j represent one of the x, y, or z directions, with the first index giving the direction of the force and the second index giving the direction of the outward normal of the face being acted upon. This definition requires that the magnitude and direction of the force, as well as the orientation of the surface, be specified to completely describe the stress, and so tensors are required (more on tensor notation below). The response to stress in a material is strain, a measure of the change in length of the material ($\Delta L/L_0$) and is unitless, as described by Hooke's law [55]:

$$\sigma_{ij} = C_{ijkl}\epsilon_{kl} \tag{3.1}$$

Here σ_{ij} is the stress, ϵ_{kl} is the strain tensor, and the C_{ijkl} are called the elastic stiffness constants, where as above i, j, k, l indices are one of the x, y, or z directions so that equation 3.1 stands for nine equations, each with nine terms on the right-hand side.

From studying the stress-strain relationship and Hooke's law we can connect the macroscopic elastic deformation behavior to the microscopic properties. Consider the stress-strain plots in figure 3.4, which are produced from a test often used to study the deformation properties of solids by applying a stress at a constant rate while simultaneously measuring the strain. Young's modulus, which quantifies the stiffness of a material in the direction of the tension, is defined as the ratio of the longitudinal stress to the longitudinal strain, which is the slope of the stress-strain curve in the linear region. Young's modulus is also defined as $E = C_{1111}$ for the case of cubic symmetric crystal structures.

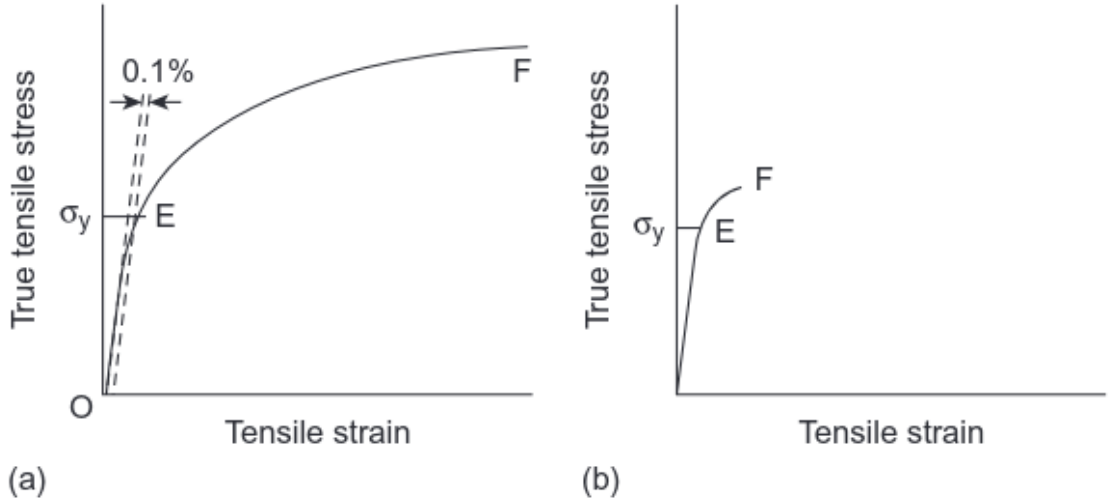

Figure 3.4: Typical stress-strain curves for (a) a ductile material an (b) a brittle material. Reproduced with permission from [53]

Shown in figure 3.4 are representative examples of typical curves obtained from (a) a ductile material undergoing plastic deformation before fracture at F, and (b) a brittle material. The curves show a linear region from O-E which is the elastic

deformation regime and obeys Hooke's law (the stress is proportional to the strain.) At E the material is said to yield which is then followed by plastic deformation until fracture at F. For most materials there is no abrupt change from the elastic regime to the plastic and the yield stress σ_y is not unique. Yielding is defined to occur when the plastic strain reaches some prescribed value, for example here 0.1% (figure 3.4(a)). The stress-strain curve is dependent on many factors including the temperature and applied strain rate during the test, as well as parameters like the crystal structure and alloy composition. Therefore, DFT provides a powerful tool for investigating the macroscopic elastic properties of a material through the ability to calculate the elastic stiffness constants, and since the only inputs required for a DFT calculation are atomic species and crystal structure, in theory any material can be characterized.

The Von Mises criterion specifies that five independent components of strain, or five independent slip systems, are needed for a general elastic shape change when volume remains constant [53]. In HCP metals in which basal slip is strongly preferred, there are only three slip systems and only two of those are independent. Therefore the elastic shape change does not occur and the material is brittle. This inhibition of elastic deformations in HCP Mg has been a topic of extensive study [56] [54] [57] [58].

Cubic systems on the other hand are known for very ductile behavior. This is because all three lattice constants are equal and the crystal structures are highly symmetric giving no strongly preferred direction for deformation. The close packing direction in the body centered cubic (BCC) crystal structure is along the (111) direction and there are 12 planes in which slip occurs. Five of these are independent, satisfying the Von Mises criterion allowing an elastic shape change.

One way to improve Mg's ductility is to alloy it with another metal which has more isotropic features in the hope that the HCP crystal structure will change to a more ductile one. Recently, alloying Mg by solid solution with rare earth elements has been investigated [59] [60] [61] [62] [63]. These studies focus on changing the

type of alloying element to improve the ductility of Mg.

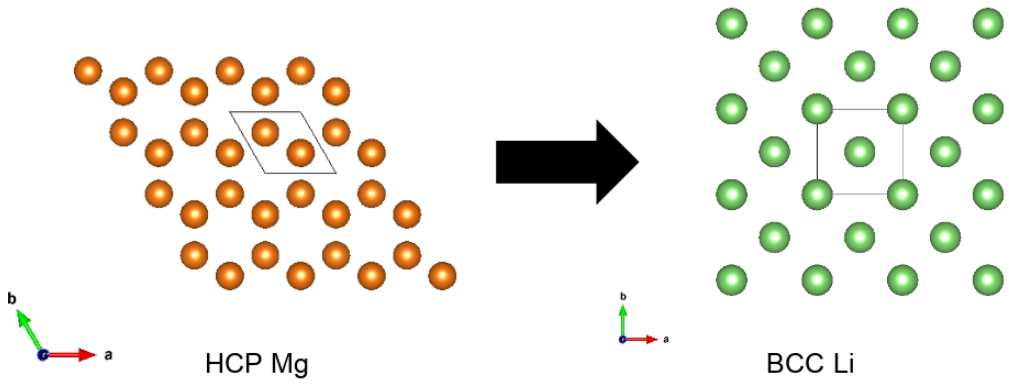

Figure 3.5: Structure of Pure HCP Mg and Pure BCC Li with primitive unit cell shown. (crystal structures from Materials Project [64])

The approach used here is to 'experiment' within computational quantum mechanical simulations via changing the lattice structure from the native HCP lattice of bulk Mg to a cubic one. In order to keep the lightweight advantage, an alloying metal with similar or lighter weight and density values is needed. Lithium (Li) is lighter and less dense ($0.58 g/cm^3$) than Mg and also is of body cubic centered (BCC) structure at room temperature, making it ideal for alloying with Mg for the application of a lightweight structural material. [47] [48] [65].

3.1.1 Crystal symmetry and elastic stiffness constants

The crystal symmetry of the Li-Mg alloy will be important in the analysis of the elastic properties. The impacts of crystal symmetry on elastic properties is readily seen by considering the elastic stiffness constants, C_{ijkl}. In the most general form there are 81 C_{ijkl} coefficients, however only 21 of these coefficients are independent since

$$C_{ijkl} = C_{jikl} C_{ijkl} = C_{ijlk} \tag{3.2}$$

which is a consequence of the fact that σ_{ij} may always be taken as symmetrical and ϵ_{kl} is defined as the symmetrical part of the strain. (see ref [55] for details).

The notation can be simplified by changing the scheme from tensor notation to Voigt notation:

tensor notation	11	22	33	23, 32	31,13	12,21
Voigt notation	1	2	3	4	5	6

With this notation we can write:

$$C_{ijkl} = C_{mn}(i, j, k, l = 1, 2, 3; m, n = 1, ..., 6) \tag{3.3}$$

and

$$\sigma_i = C_{ij}\epsilon_j(i, j = 1, 2, ..., 6) \tag{3.4}$$

The Hooke's law equation can then in general be written:

$$\begin{pmatrix} \sigma_{11} \mapsto \sigma_1 \\ \sigma_{22} \mapsto \sigma_2 \\ \sigma_{33} \mapsto \sigma_3 \\ \sigma_{23} \mapsto \sigma_4 \\ \sigma_{13} \mapsto \sigma_5 \\ \sigma_{12} \mapsto \sigma_6 \end{pmatrix} = \begin{pmatrix} C_{11} & C_{12} & C_{13} & C_{14} & C_{15} & C_{16} \\ C_{21} & C_{22} & C_{23} & C_{24} & C_{25} & C_{26} \\ C_{31} & C_{32} & C_{33} & C_{34} & C_{35} & C_{36} \\ C_{41} & C_{42} & C_{43} & C_{44} & C_{45} & C_{46} \\ C_{51} & C_{52} & C_{53} & C_{54} & C_{55} & C_{56} \\ C_{61} & C_{62} & C_{63} & C_{64} & C_{65} & C_{66} \end{pmatrix} \begin{pmatrix} \epsilon_{11} \mapsto \epsilon_1 \\ \epsilon_{22} \mapsto \epsilon_2 \\ \epsilon_{33} \mapsto \epsilon_3 \\ \epsilon_{23} \mapsto \epsilon_4 \\ \epsilon_{13} \mapsto \epsilon_5 \\ \epsilon_{12} \mapsto \epsilon_6 \end{pmatrix} \tag{3.5}$$

The elastic stiffness constants are further reduced when applied to high symmetry crystal structures. HCP crystal structures have 5 independent elastic constants $(C_{11}, C_{12}, C_{13}, C_{33}, C_{44})$, and cubic crystal structures have only 3 (C_{11}, C_{12}, C_{44}). Hooke's law for a cubic system then reads:

$$\begin{pmatrix} \sigma_1 \\ \sigma_2 \\ \sigma_3 \\ \sigma_4 \\ \sigma_5 \\ \sigma_6 \end{pmatrix} = \begin{pmatrix} C_{11} & C_{12} & C_{12} & 0 & 0 & 0 \\ C_{12} & C_{11} & C_{12} & 0 & 0 & 0 \\ C_{12} & C_{12} & C_{11} & 0 & 0 & 0 \\ 0 & 0 & 0 & C_{44} & 0 & 0 \\ 0 & 0 & 0 & 0 & C_{44} & 0 \\ 0 & 0 & 0 & 0 & 0 & C_{44} \end{pmatrix} \begin{pmatrix} \epsilon_1 \\ \epsilon_2 \\ \epsilon_3 \\ \epsilon_4 \\ \epsilon_5 \\ \epsilon_6 \end{pmatrix} \tag{3.6}$$

and for a hexagonal structure:

$$\begin{pmatrix} \sigma_1 \\ \sigma_2 \\ \sigma_3 \\ \sigma_4 \\ \sigma_5 \\ \sigma_6 \end{pmatrix} = \begin{pmatrix} C_{11} & C_{12} & C_{13} & 0 & 0 & 0 \\ C_{12} & C_{11} & C_{13} & 0 & 0 & 0 \\ C_{13} & C_{13} & C_{33} & 0 & 0 & 0 \\ 0 & 0 & 0 & C_{44} & 0 & 0 \\ 0 & 0 & 0 & 0 & C_{44} & 0 \\ 0 & 0 & 0 & 0 & 0 & (C_{11} - C_{12})/2 \end{pmatrix} \begin{pmatrix} \epsilon_1 \\ \epsilon_2 \\ \epsilon_3 \\ \epsilon_4 \\ \epsilon_5 \\ \epsilon_6 \end{pmatrix} \tag{3.7}$$

From these C_{ij} we can calculate the macroscopically measurable quantities for materials [55], [66]: Young's modulus(E), Poisson's ratio(ν), Shear modulus(G), the B/G ratio (a measure of ductility), and Bulk modulus(B). The expressions are given for isotropic materials, which is their simplest form. For a more general expression see ref [66]

- **Young's modulus** is the stiffness of the system, given by the slope of the stress-strain curve. In terms of elastic constants it is given by $\mathrm{E} = C_{11}$. Larger values of the Young's modulus indicate a stiffer material.

- **Poisson's ratio** is a measure of the expansion of a material when it is compressed in the transverse direction, or the ratio of the transverse strain to the axial strain, and in general is used as a measure of plasticity. It is given by $\nu = -\mathrm{E}\ C_{12}$.

- The **Shear modulus**, or the modulus of rigidity, is given by $\mathrm{G} = \mathrm{E}/2(1+\nu)$.

- The **B/G ratio** is a good indicator as to whether a material is brittle or ductile, with values above 1.7 indicating ductile behavior and values below this number being brittle. [67]

- The **bulk modulus** represents the volume compressiblity and is given by $\mathrm{B} = \mathrm{E}/3(1-2\nu)$.

Material	Young's Modulus E (GPa)	Poisson's ratio ν	Shear Modulus G (GPa)	Bulk Modulus B (GPa)
Aluminium	68.9	0.34	25.7	71.8
Concrete	27.6	0.20	11.5	15.3
Copper	89.6	0.34	33.4	93.3
Glass	68.9	0.25	27.6	45.9
Nylon	28.3	0.4	10.1	47.2
Rubber	0.0019	0.499	0.65×10^{-3}	0.326
Steel	207	0.29	80.2	164

Table 3.1: Typical values of the elastic moduli for common materials. Reproduced with permission from [66]

To get a better feel for these numbers, table 3.1 lists typical values for the elastic moduli for common materials.

In this study, the elastic constants have been calculated for each structure and the macroscopic elastic properties have been plotted: bulk modulus, shear modulus, Young's modulus, Poisson ratio and bulk/shear ratio [68]. From these results it can be determined what effect Li concentration has on the properties of the Mg system. The amount of Li included in the structure is varied from 0% to 100% and the Minima Hopping Method is used to determine the ground state configurations (see section 2.3). This study relies on VASP, a commercially maintained DFT code which has been used by hundreds of researchers to successfully study a wide range of materials. VASP is built upon plane wave basis sets, which requires a sample-representative unit cell which is periodically repeated in three directions. This is a suitable method for studying Mg alloys as this is a bulk system with a periodic crystal structure which is readily described by a repeated unit cell.

The process of alloying is not straightforward. On the theoretical side, simply replacing atoms within the Mg structure will not always result in an end product that is energetically stable or possible to make experimentally. On the experimental side producing alloys of various compositions in a laboratory is time and cost intensive. Here an investigative and experimental approach is used within a simulation framework to minimize the time spent searching for stable candidates. Once found, the candidate structures are further analyzed with another series of DFT calculations to determine their elastic properties.

3.2 Background

Many groups have approached the Mg-Li system by investigating the properties of a few ordered structures. The most common method is to fix the lattice and change the atoms, where only hexagonal and cubic lattice structures are considered. In 2001, Uesugi et. al. [69] used the local density approximation within DFT to investigate three different configurations for 87% Mg. Counts et al. [63] studied the mechanical properties of cubic supercells of Mg-Li of various Mg concentrations using a generalized gradient approximation within DFT. Taylor, Curtarolo, and Hart [70] made predictions of Mg-Li ordered phases using the first-principles-based cluster expansion (CE) method and found ground states at 12%, 50%, 66%, and 75% Mg concentrations. Liang and Gong [71] selected three Mg-Li compositions and studied the structural stability and elastic properties. They used a generalized gradient first principles approximation to find the crystal structure of the ground-state of each composition. Phasha et al. [46] also used DFT within the generalized gradient approximation to investigate the existence of FCC and BCC structures at 50%, 75%, 83% and 87% Mg concentrations. That group later also studied random Mg-Li alloys in HCP, FCC, and BCC lattices [72]. Shin and Carter [47] applied orbital-free density functional theory (OFDFT) to ordered and disordered BCC Mg-Li supercells to study their elastic properties.

This study approaches the problem from a new perspective, by beginning with an ab-initio energy search over all possible compositions and structures [68]. This allows for finding naturally occurring structures over the complete composition range of the two metals. From the results the most promising structures are selected. The selection criteria is based on the space group and formation energy of the structure. Foremost, the task is to look for high symmetry structures as it is likely that these will be the structures with the highest ductility. Structures are also chosen with the lowest formation energy as these are the most stable and therefore the most likely to be able to be synthesized. These favorable structures are then further analyzed to investigate and characterize the elastic properties and stability.

3.3 MHM Results

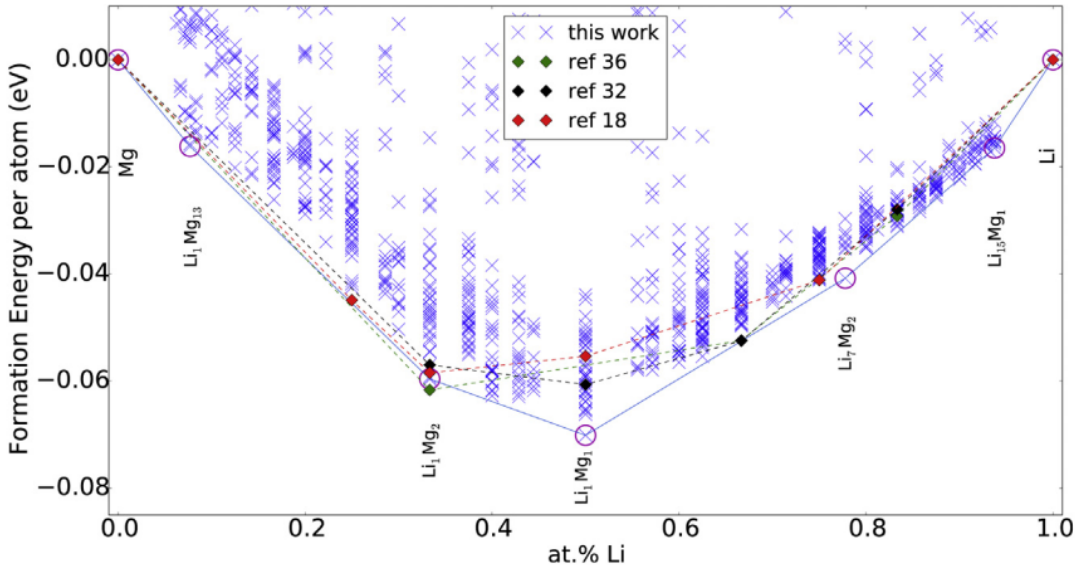

Figure 3.6: Convex Hull of the Li-Mg Binary system. Blue x's indicate structures from this work, where magenta circles indicate structures belonging to the convex hull. Green diamonds are structures from the Materials Project, black diamonds are structures from the Open Quantum Materials Database, and red diamonds are structures obtained from the AFLOW online database. [68]

To ensure stability of the predicted structures, three analyses are done: energetic stability, thermodynamic stability, and elastic stability. First, the energetic stability of the structures found are analyzed. To do so, the results of the MHM calculations are re-optimized with tighter energy convergence criteria and the formation energy is calculated. These formation energy results are then plotted with respect to Li composition. This plot has a line, called the convex hull, which connects the lowest energy structures. In figure 3.6 the re-optimized formation energies of the structures found in the MHM search of the Li-Mg binary system are presented. Each blue x represents the formation energy of each structure found at the bottom of an energy valley for each particular composition. The solid line at the bottom connects the lowest energy structures and depicts the convex hull. Structures on the line, marked by a magenta circle, are energetically stable and can be chemically synthesized.

There are three online databases which have reported theoretical reslts for the Li-Mg system: The Materials Project [73] [74] [64] is an online database dedicated

% Li	Phase	Space Group	Atoms in Unit Cell	Formation Energy(meV)
7	Li_1Mg_{13}	P1(1)	14	-9.7 (ground)
25	Li_1Mg_3	Fm-3m(225)	4	-27.6 (metastable)
33	Li_1Mg_2	P-6m2(187)	3	-35.5(metastable)
33	Li_1Mg_2	I4/mmm(139)	6	-59.6 (ground)
40	Li_2Mg_3	R-3m(166)	5	-62.7 (ground)
43	Li_3Mg_4	P6/mmm(191)	7	-15.6 (metastable)
50	Li_1Mg_1	Pm-3m(221)	6	-70.1 (ground)
50	Li_1Mg_1	P4/mmm(123)	4	-65.2(metastable)
78	Li_7Mg_2	Immm(71)	9	-40.7 (ground)
84	Li_5Mg_1	P-62m(189)	6	-28.0 (metastable)
85	Li_6Mg_1	P1(1)	7	-28.3 (ground)
88	Li_7Mg_1	P-6m2(187)	8	-24.2 (metastable)
90	Li_9Mg_1	C12/m1(12)	10	-22.3 (ground)
93	$Li_{15}Mg_1$	Cmmm(65)	16	-16.4 (ground)

Table 3.2: Space group, number of atoms in the unit cell and formation energy for the lowest-energy structures found in our structure search. [68]

to predicting properties of materials, AFLOW [75] is an online library of structural ab initio calculations, and the Open Quantum Materials Database (OQMD) [76] is a database of DFT calculated thermodynamic and structural properties. Structures from these databases are included in the results of this study for comparison. Each of these structures from other studies has been re-optimized with our pseudopotentials and convergence criteria. In figure 3.6 it can be seen that our search method has found structures at all the compositions reported by these sources. While many of the structures are found to be of lower energy than the reported ground states, there are three places where our results are of higher formation energy: at the compositions Li_1Mg_2, Li_2Mg_1, and Li_3Mg_1. However, these results are within the numerical accuracy of our calculations. Five structures are on the convex hull, three of which are previously unreported. Each will be discussed in more detail below.

Second, to check thermodynamic stability the phonon dispersion is calculated. It is well known that a positive phonon dispersion indicates thermal stability. Interestingly, a phonon gap appears in a large portion of our structures. Only one of the structures on the convex hull, Li_1Mg_2 exhibits negative phonon modes. The phonon spectra for each of the structures found on the convex hull can be found in appendix B.

Third, the elastic stability as outlined in Mouhat and Coudert has been calculated. [77] Due to the range of crystal structures found, we refer the reader to the original work for a detailed description of the calculations. All of the structures presented in figure 3.2 meet this mechanical stability criteria.

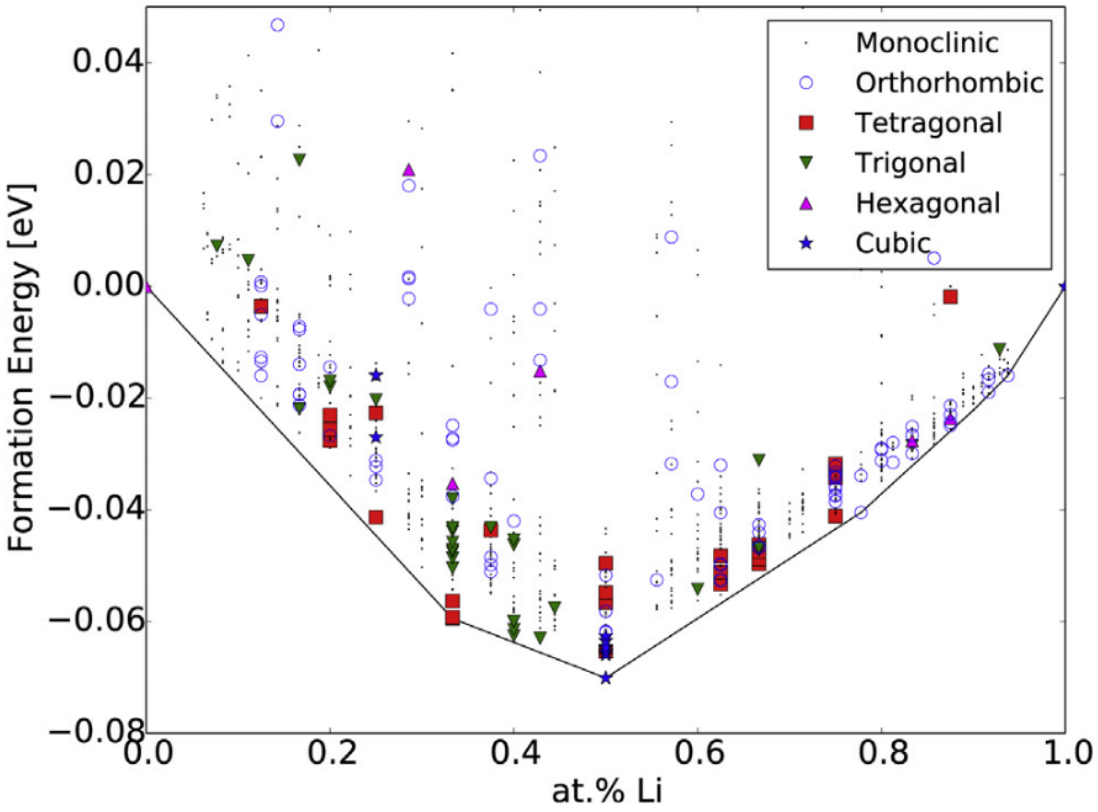

Figure 3.7: Convex hull of the Mg-Li binary system with crystal structure indicated by symbols. The left of the plot is pure Li and the right of the plot is pure Mg. [68]

To see how Li concentration affects the crystal lattice, the results of the structure search are plotted in three ways: first, in figure 3.7 the convex hull is plotted again replacing the blue x's with symbols indicative of the space group of each structure; second, in figure 3.8 for each composition of atomic percent Li the highest space group found is plotted as well as the space group of the energetic ground-state; third, in figure 3.9 the number of structures found within each space group are plotted via a histogram. These plots indicate that our structural search is able to locate a large diversity of crystal symmetries, which indicates the richness of the Li-Mg compounds.

It is important to note at this point that because of the richness of lattice sym-

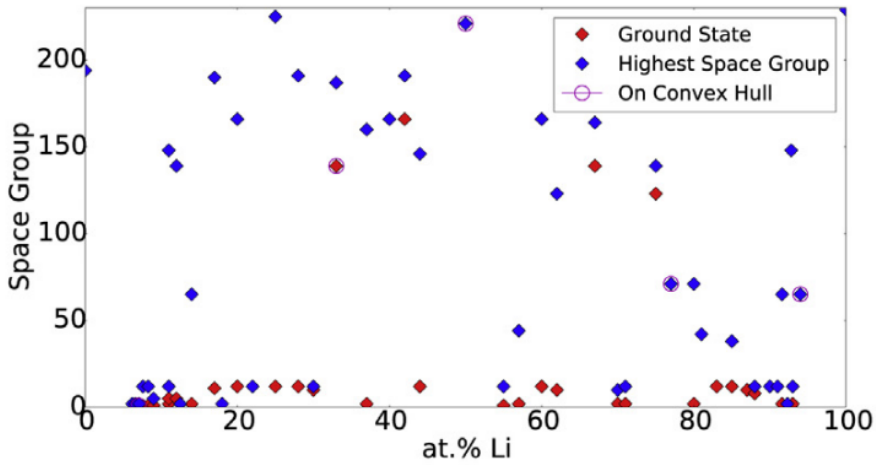

Figure 3.8: The Space Group (by number) of the highest symmetry structure and the ground state structure vs at% Li. [68]

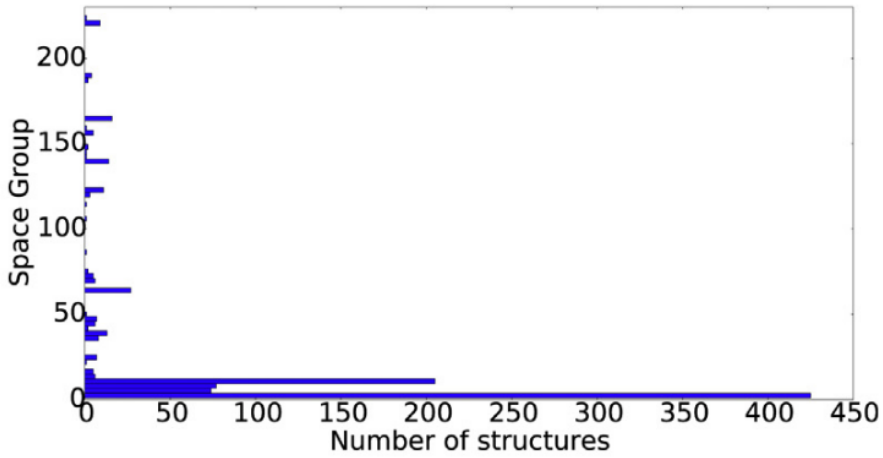

Figure 3.9: Histogram of the number of structures found in each Space Group with respect to every structure found. [68]

metry in our results, comparison of our results with previous works present in the literature proves challenging. All studies found in the literature concern only hexagonal and cubic structures, with the exception of the results of ref [46]. The databases do not show this exclusion of lower symmetry structures. The results of Taylor et. al. can be found in ref [70] as well as on the online database, AFLOW [75]. AFLOW includes structures of lower symmetry than cubic or hexagonal, while the only results that are analyzed in ref [70] are those which are cubic and hexagonal. From figure 3.9, a majority of the structures found are low in symmetry with international space group numbers lower than 50. However figure 3.8 shows that many of the ground state structures are of these low symmetries. Experimentally, it is known that pure

Composition	Space Group	a	b	c	α	β	γ	DOS(Ef)(eV)
Li_1Mg_{13}	P1(1)	6.07	8.09	7.46	114.4	75.9	109.6	2.60
Li_1Mg_2	I4/mmm(139)	3.43	3.43	10.53	90	90	90	0.53
Li_1Mg_1	Pm-3m(221)	3.42	3.42	3.42	90	90	90	1.06
Li_7Mg_2	Immm(71)	9.67	9.72	3.83	90	90	90	2.23
$Li_{15}Mg_1$	Cmmm(65)	7.45	6.14	7.45	90	110.5	89.9	4.29

Table 3.3: Space group, lattice parameters, angles, and DOS at Fermi for ground state structures. [68]

Mg and Li metals crystallize into HCP and BCC structures, respectively [65] [78] [79] [80]. Consequentially these are the lattice types which theoretical calculations are based upon. However our results indicate that limiting attention to only structures with hexagonal and cubic symmetry may miss a large number of candidates with the potential for good elastic qualities.

Additionally, in figure 3.7 there are only a small number of cubic and hexagonal structures, but many of tetragonal symmetry. Note that ref [46] includes tetragonal structures. Since our calculations are performed at zero temperature and pressure, we assume structures with tetragonal symmetries and c/a ratios close to one are not stationary and may change to cubic symmetry. Of the structures included in figure 3.7 all of the tetragonal structures either have a c/a ratio of one or are within 20% of that value.

As part of the analysis the electron localization function (ELF) was calculated. We present the real space contour plots of the ELF along a selected plane of the Li_1Mg_1 cubic structure as a representative sample (figure 3.10). The ELF plots contain information regarding the distribution of electrons and bonding of atoms in bulk systems. The bottom of the scale, represented by the blue color, corresponds to a depletion of charges where electrons are delocalized. The top of the scale, represented by red, corresponds to an excess of charges where electrons are highly localized. All of our systems are metallic, and this is reflected in the ELF plots. Metallic bonding can be recognized by the homogeneous green delocalized sea of electrons between all of the atoms. This was a common feature for all of the structures studied here. Because every ELF plot presented extremely similar

characteristics to figure 3.10, we will not discuss the ELF plots for each individual structure.

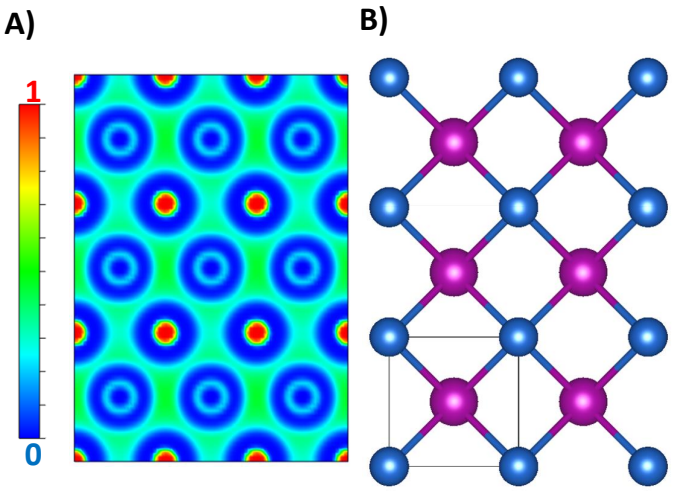

Figure 3.10: 2D slice of the real space contour plot of the cubic Li_1Mg_1 Electron Localization Function.

From our search at zero temperature and pressure we have found five ground state structures which form the convex hull at compositions Li_1Mg_{13} Li_1Mg_2, Li_1Mg_1, Li_7Mg_2, $Li_{15}Mg_1$ and nine meta-stable structures at compositions Li_1Mg_3, Li_1Mg_2, Li_2Mg_3, Li_3Mg_4, Li_1Mg_1, Li_5Mg_1, Li_6Mg_1, Li_7Mg_1, and Li_9Mg_1. In table 3.2 we report the atomic percent Li, the space group by Pearson symbol and international number, the number of atoms in the primitive unit cell, and the formation energy for each structure.

When compared to the online databases, our methods have recovered all previously reported structures. Li_1Mg_3, Li_1Mg_2, Li_1Mg_1, Li_1Mg_5, Li_2Mg_1, Li_3Mg_1, Li_5Mg_1 have been found in the Materials Project database, the Open Quantum Materials Database, and AFLOW. Remarkably, we have also discovered many previously unreported structures. The most interesting of these are those which lie on the convex hull (Li_1Mg_{13}, Li_7Mg_2, $Li_{15}Mg_1$). Their composition, space group, lattice parameters, and DOS at Fermi Energy are given in table 3.3. We discuss the elastic properties of the Li-Mg system followed by the ground state structures further individually.

3.3.1 Elastic Properties Results

Table 3.4: Computed elastic constants for lowest-energy structures. All values are given in GPa. [1] & [2]ref [71], [3] ref [46]. [68]

Structure	C11	C12	C44	C33	C13	C66
Mg	56.5	25.1	15.7	56.2	26.6	
Mg [2]	59.5	26.12	16.35	61.55	21.80	
Li_1Mg_{13}(1)	57.2	22.2	17.0	58.1	19.6	20.0
Li_1Mg_3(FCC)(225)	37.3	26.5	0.34			
Li_1Mg_3(BCC)[2]	41.0	24.0	37			
Li_1Mg_3(BCC)[1]	41.7	24.8	36.4			
Li_1Mg_2(187)	62.5	13.3	17.9	83.5	0.60	24.5
Li_1Mg_2(139)	42.7	21.7	39.7	43.2	21.9	34.0
Li_3Mg_4(191)	42.9	22.4	16.6	74.9	0.82	10.2
Li_1Mg_1(CCP)(221)	33.0	20.9	18.3			
Li_1Mg_1(123)	35.7	17.9	26.4	25.7	21.9	22.0
Li_1Mg_1(BCC)[2]	30.5	19.5	23.4			
Li_1Mg_1(BCC)[1]	34.1	20.0	26.5			
Li_1Mg_1(CCP)[3]	37.5	19.7	25.9			
Li_7Mg_2(71)	20.7	16.7	0.49	31.1	15.8	16.7
Li_5Mg_1(189)	28.2	16.7	0.42	40.3	0.51	0.57
Li_7Mg_1(187)	27.1	15.3	0.47	36.4	0.52	0.58
Li_7Mg_1(FCC)[3]	15.8	16.9	11.7			
Li_9Mg_1(12)	28.2	10.4	12.7	26.3	0.68	11.9
$Li_{15}Mg_1$(65)	27.1	8.9	3.8	22.5	8.4	6.6
Li	15.1	13.3	11.9			
Li [2]	15.1	12.7	11.4			

Table 3.4 lists the elastic stiffness constants and table 3.5 lists the values of the elastic properties. In figure 3.11 and figure 3.12 we plot these elastic properties versus Li concentration.

With respect to the entire Li-Mg system, we see a linear decrease in Bulk modulus as Li concentration increases. This is in agreement with what has been reported.[81] The Poisson's ratio is generally increasing, indicating an increase of plasticity and metallicity in the alloy as Li concentration increases. We see a general decreasing in Young's modulus with increasing Li content, indicating a more elastic alloy.

For alloys with low Li concentrations, the bulk modulus to Shear modulus ratio shows brittle behavior. In all these plots, excluding the bulk modulus, we see a jump in the values for Li_1Mg_2 composition. Both structures at this composition show this deviation from the trend. We also see a smaller jump for Li_9Mg_1. These

Table 3.5: Calculated Bulk modulus, Shear modulus, Young's modulus, Poisson's ratio, and Bulk modulus/Shear modulus(B/G) ratio. [1] & [2]ref [71], [3] ref [46]. [68]

Structure	Bulk	Shear	Young	Poisson	B/G
Mg	36.25	17.51	45.24	0.29	2.07
Mg [2]	34.3				
Li_1Mg_{13}(1)	33.16	18.31	46.39	0.26	1.81
Li_1Mg_3(FCC)(225)	30.18	18.49	45.04	0.25	1.63
Li_1Mg_3(BCC)[2]	30.5	20.4	50.1	0.23	
Li_1Mg_3(BCC)[1]	29.7				
Li_1Mg_2(187)	28.75	23.51	55.42	0.17	1.22
Li_1Mg_2(139)	28.864	22.715	53.680	0.190	1.27
Li_3Mg_4(191)	26.31	15.57	38.98	0.25	1.69
Li_1Mg_1(CCP)(221)	24.98	11.79	38.50	0.24	2.11
Li_1Mg_1(123)	24.31	12.94	32.52	0.27	1.87
Li_1Mg_1(BCC)[2]	24.7	15.7	38.8	0.24	
Li_1Mg_1(BCC)[1]	23.2				
Li_1Mg_1(CCP)[3]	25.6	16.9	41.6		1.51
Li_7Mg_2(71)	17.85	8.14	21.01	0.30	2.19
Li_5Mg_1(189)	16.77	6.62	17.52	0.32	2.53
Li_7Mg_1(187)	16.05	6.71	17.66	0.31	2.39
Li_7Mg_1(FCC)[3]	16.6	2.7	8.2		6.15
Li_9Mg_1(12)	15.40	7.42	19.11	0.29	2.07
$Li_{15}Mg_1$(65)	14.78	5.26	14.02	0.34	2.80
Li	13.96	4.77	12.46	0.35	2.92
Li [2]	12.95				
Li [3]	13.3				

jumps cannot be accounted for from crystal symmetry, since there are structures with similar, and higher, symmetry such as Li_1Mg_1. However it was found that the Li_1Mg_2 structures exhibit peculiar phonon band dispersion. In comparison to the reported values, our results match reasonably well with what has been reported.

3.3.2 Ground-state structures

Li_1Mg_{13}

For the Li_1Mg_{13} composition, no structures have been previously reported. We find a ground state structure of space group P 1(1) which indicates only one symmetry operation, the identity. Figure 3.13 shows the crystal structure and the density of states. There is a large density of states around the Fermi level, likely due to the large

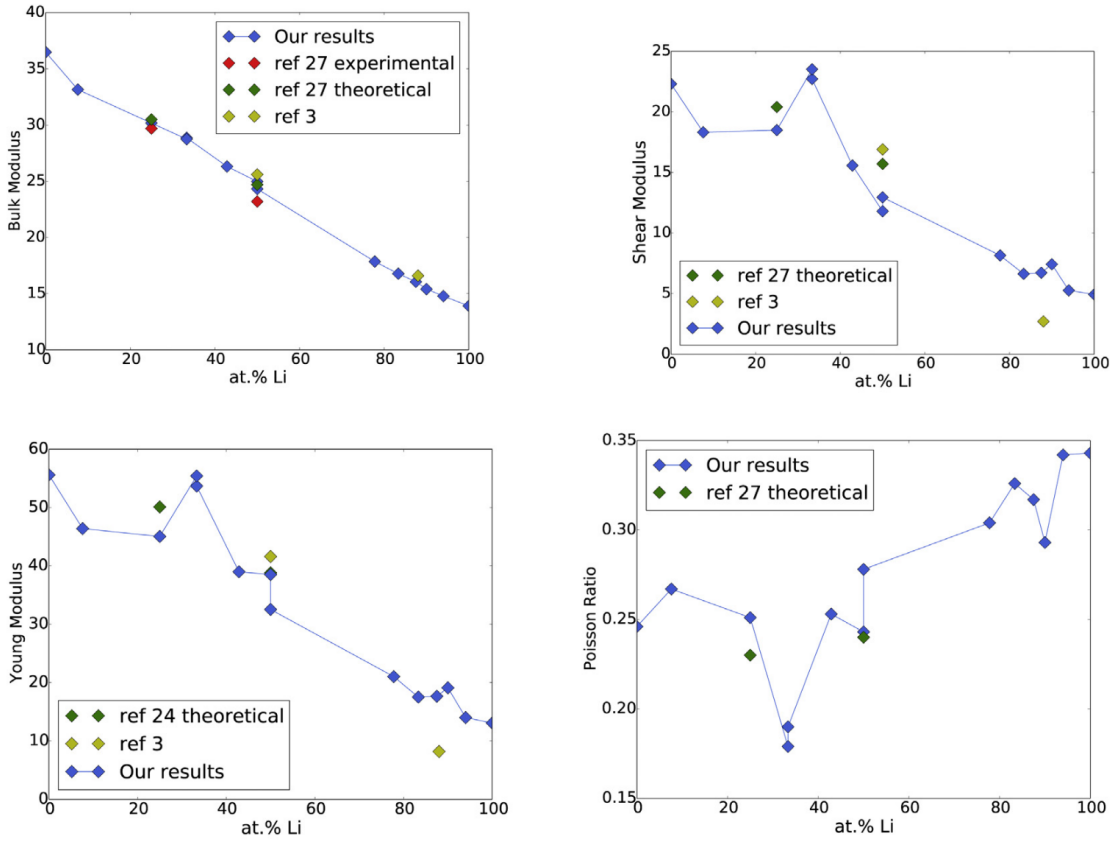

Figure 3.11: Elastic Constants. Ref [71] reports the theoretical and experimental results, these are plotted separately. Green diamonds represent theoretical results reported in Ref [71], red diamonds represent experimental results reported in Ref [71], yellow diamonds represent results reported in Ref [46], blue diamonds represent results from this work. [68]

number of atoms in the unit cell. Despite the large and unequal lattice parameters (a=6.07 Å, b=8.09 Å, c=7.46 Å, $\alpha = 114.4°, \beta = 75.9°, \gamma = 109.6°$), the elastic properties are not very different from the values for the cubic Li_1Mg_3 (225) (table 3.4). As can be seen in figure 3.12, the B/G ratio actually shows ductile behavior and this is the only one of the Mg-rich structures to do so. The nearest neighbor distance between Mg-Mg atoms, and Mg-Li atoms in this structure is 3.11 Å and 3.10 Å, respectively. There are no Li atoms which are neighbors with other Li atoms.

Li_1Mg_2

At composition Li_1Mg_2 we find the ground state structure to be tetragonal and of space group $I4/mmm$ (139). Figure 3.14 shows the crystal structure and the density of states. There are 16 symmetry operations for this space group; however,

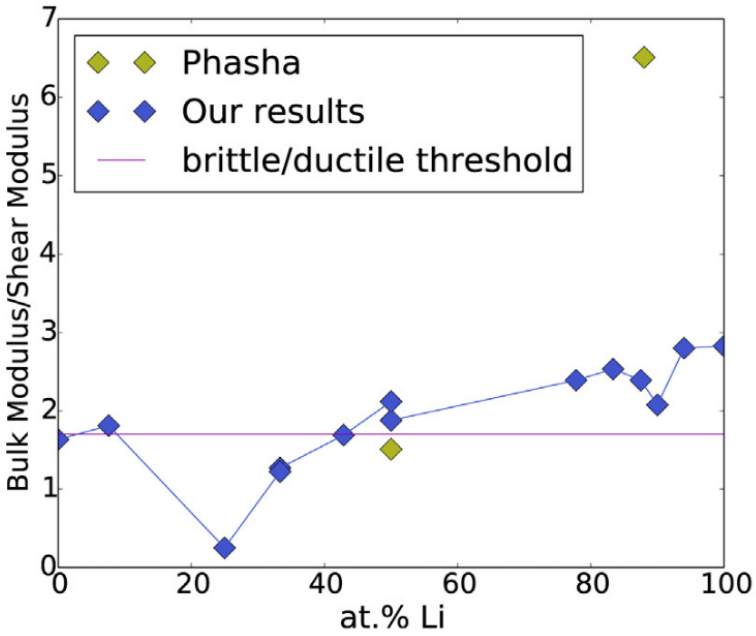

Figure 3.12: B/G ratio, a measure of brittle or ductile behavior. The critical value separating the two lies at 1.7 and is drawn with a magenta horizontal line. Yellow diamonds from ref [46]. [68]

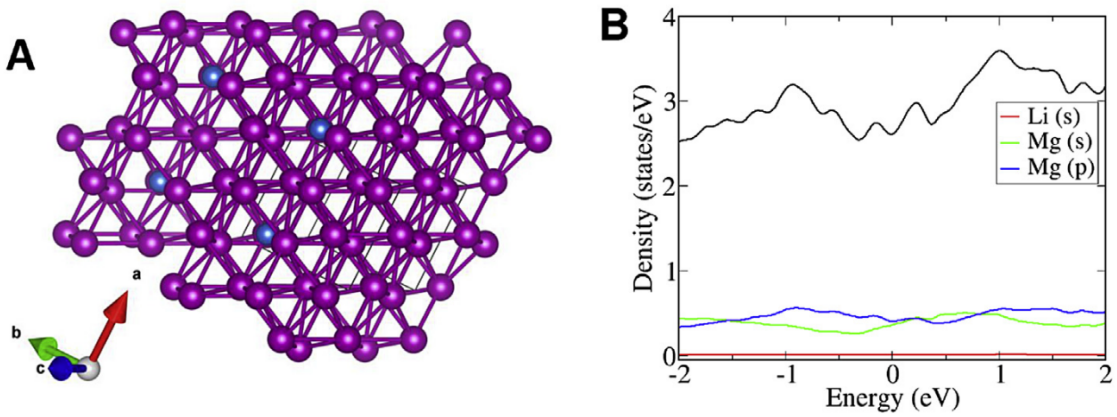

Figure 3.13: Li_1Mg_{13} Space Group $P1(1)$ A) crystal structure, B) density of states (black line indicates total DOS). [68]

the significant difference in the lattice constants (a=b=3.43 Å, c=10.53 Å) and the value of B/G indicate that it is likely brittle. The nearest neighbor distance between Mg-Mg atoms, Li-Li atoms, and Mg-Li atoms in this structure is 3.43 Å, 3.43 Å, and 2.94 Å, respectively.

For this composition a low energy hexagonal structure is found for space group $P-6m2$ (187), 24.1meV per atom above the ground state. Figure 3.15 shows the

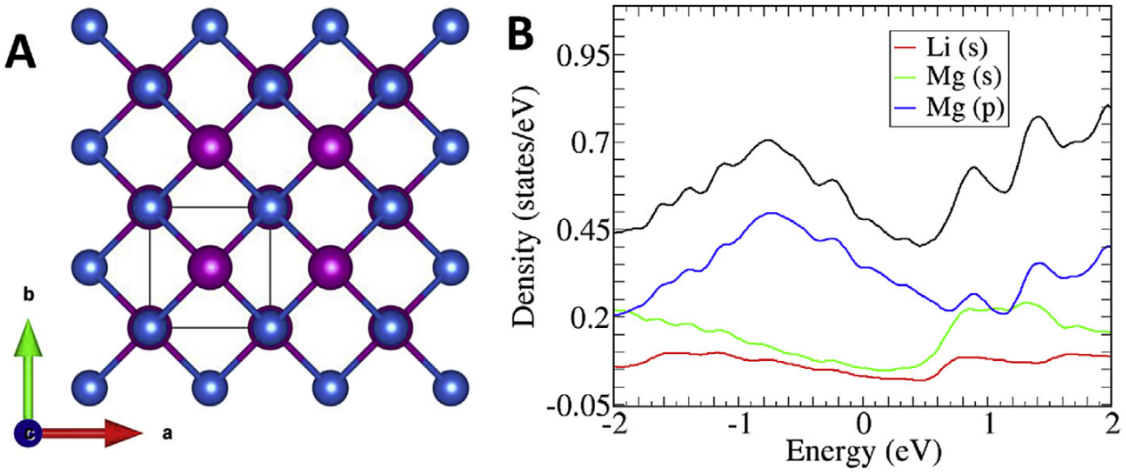

Figure 3.14: Li1Mg2 Space Group $I4/mmm$ (139) A) crystal structure B) Density of states (black line indicates total DOS). [68]

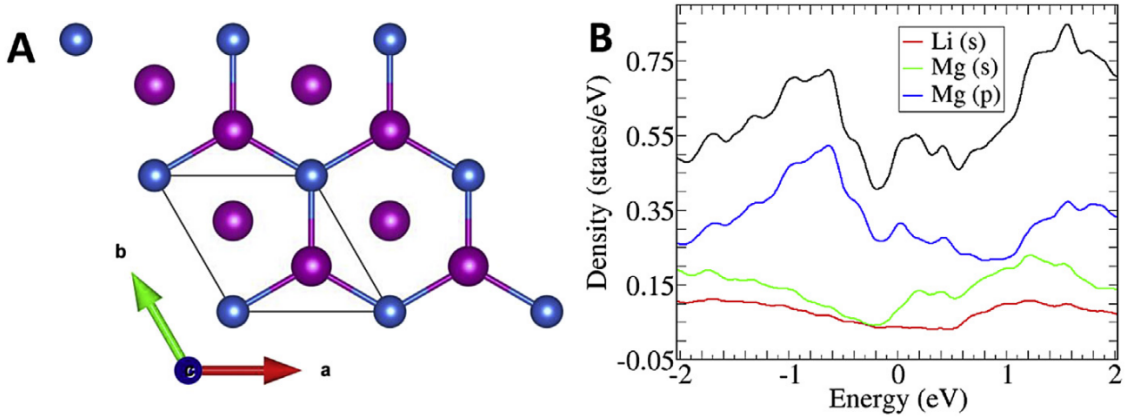

Figure 3.15: Li1Mg2 Space Group $P-6m2$ (187) A) crystal structure B) Density of states (black line indicates total DOS). [68]

crystal structure and density of states. In the crystal structure the hexagonal pattern can clearly be seen with Mg atoms surrounding Li atoms. The elastic properties are similar to the ground-state tetragonal structure (see table 3.5). The nearest neighbor distance between Mg-Mg atoms, Li-Li atoms, and Mg-Li atoms in this structure is 3.22 Å, 4.94 Å, and 2.85 Å, respectively. When examining the phonon structure however, negative phonons were observed around -100 cm^{-1} indicating an unstable structure. We note that this structure may become stable at higher pressure or temperature conditions.

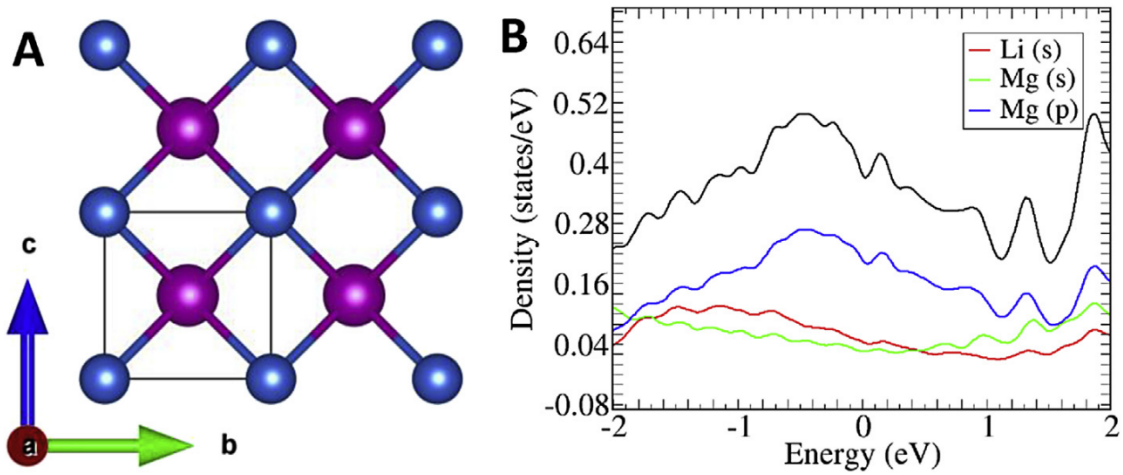

Figure 3.16: Li_1Mg_1 spacegroup $Pm-3m(221)$ A) crystal structure, B) density of states (black line indicates total DOS). [68]

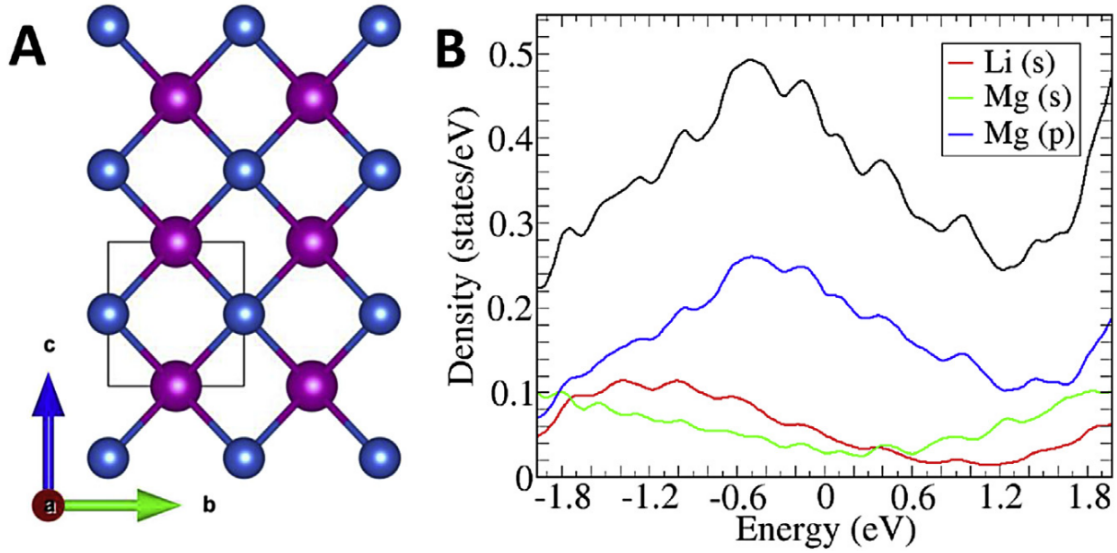

Figure 3.17: Li_1Mg_1 spacegroup $P4/mmm(123)$ A) crystal structure, and B) density of states (black line indicates total DOS). [68]

Li_1Mg_1

Li_1Mg_1 is the lowest lying energy structure for the entire LiMg binary system and has been studied extensively. [75] [64] [74] [73] The ground state structure was found to be cubic of space group $Pm-3m$ (221). This agrees well with what has been previously reported [46] [70] [71]. Figure 3.16 shows the crystal structure, and the density of states. The cubic structure is easily recognized. The nearest neighbor distance between Mg-Mg atoms, Li-Li atoms, and Mg-Li atoms in this structure is 3.41 Å, 3.41 Å, and 2.95 Å, respectively.

The lowest energy tetragonal structure found at this composition is of space group $P4/mmm$ (123) and is 4.9meV per atom above the ground state. Figure 3.17 shows the crystal structure and the density of states. The nearest neighbor distance between Mg-Mg atoms, Li-Li atoms, and Mg-Li atoms in this structure is 3.36 Å, 3.36 Å, and 2.96 Å, respectively. As stated above, we find many tetragonal structures in our MHM results and there is good reason to anticipate that these may change to cubic symmetry. It is interesting to note that values for elastic properties in table 3.5 are similar, further strengthening this assumption.

Li_7Mg_2

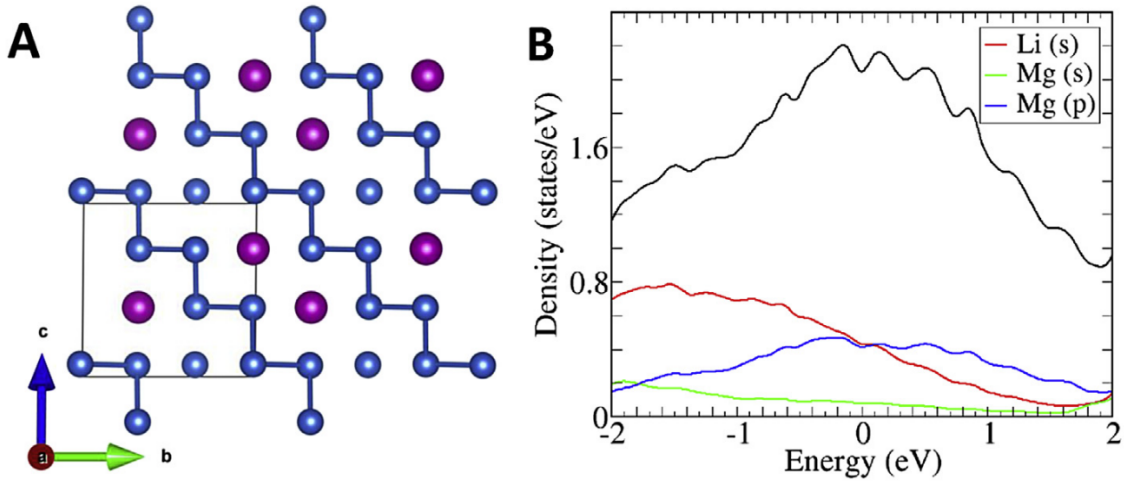

Figure 3.18: Li_7Mg_2 spacegroup $Immm$(71) A) crystal structure B) density of states (black line indicates total DOS). [68]

There are no previously reported structures at the Li_7Mg_2 composition. We find a ground state structure of orthorhombic space group $Immm$ (71). Figure 3.18 shows the crystal structure and the density of states. This space group only has 8 symmetry operations and the structure has two large lattice constants close in value with the third much shorter (a=9.67 Å, b=9.72 Å, c=3.83 Å). The nine atoms in the primitive unit cell give a large density of states at the Fermi level. The nearest neighbor distance between Mg-Mg atoms, Li-Li atoms, and Mg-Li atoms in this structure is 3.20 Å, 2.95 Å, and 2.99 Å, respectively.

$Li_{15}Mg_1$

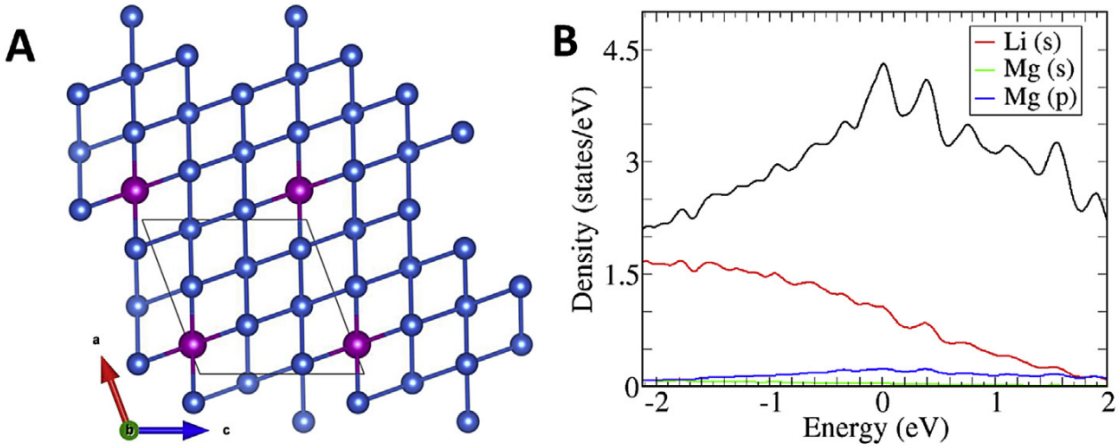

Figure 3.19: $Li_{15}Mg_1$ spacegroup $Cmmm(65)$ A) crystal structure B) density of states (black line indicates total DOS). [68]

Structures with composition Li_15Mg_1 are previously unreported. As the ground state we find an orthorhombic structure of space group $Cmmm$ (65), which is similar to the space group of Li_7Mg_2 but with a face-centered lattice as opposed to a body-centered lattice. Figure 3.19 shows the crystal structure and density of states. There are 16 atoms in the unit cell, the most of the ground state structures and consequently this structure has the highest density of states value at the Fermi level. Interestingly, the lattice constants are all similar in value with (a=c=7.445 Å, b=6.14 Å). The nearest neighbor distance between Li-Li atoms and Mg-Li atoms in this structure is 3.02 Å and 3.04 Å, respectively.

3.4 Conclusions

Beyond the cubic structure at Li_1Mg_1, it is not immediately obvious if the addition of Li to Mg produces the desired effect of a more symmetric crystal structure. Overall the majority of the structures found are low in symmetry (see figure 3.9). It does seem that the structures on the Li rich side of figure 3.7 are lower in energy, however from figure 3.8 and table 3.2 there are also less high-symmetry Li-rich structures. Further analysis of the elastic constants shows a trend of improving values across all

five calculated elastic moduli with an increase of atomic percent Li. It seems that even though few cubic structures were found, the addition of Li to Mg influences the lattice parameters enough to change the strong preference for one slip plane observed for HCP Mg. The robustness of the results produced from the Minima Hopping Method provides a compelling path towards achieving an ultralight Mg alloy suitable to be used in structural applications.

In conclusion, we have performed a systematic study of the Li-Mg binary system considering all compositions from 0 to 100% Li with up to 16 atoms per unit cell using *ab-initio* density functional theory. We have found five structures belonging to the convex hull, three of which were previously unreported. We have studied their stability in three ways: energetically, thermodynamically, and elastically. We have also calculated the elastic constants and the elastic moduli giving the macroscopic elastic properties and studying how Li content effects these characteristics. It was found that adding low concentrations of Li does not help Mg's inherently low ductility, but does have a positive effect on the other elastic properties. In higher concentrations, the addition of Li seems to lower the overall symmetry of the structures found. Counter intuitively, increasing Li has a positive effect on the ductility. The results of this study imply that a more complex mechanism beyond the crystal structure is responsible for the elastic properties in Li-Mg alloys.

Chapter 4

PbS Study

4.1 Motivation

The motivating challenge behind this chapter is the realization of an infrared (IR) light camera which exhibits a small form factor so as to minimize the Size Weight and Power - Cost (SWaP-C) of the device. The electromagnetic spectrum is illustrated in figure 4.1 with special emphasis on the visible and IR sections.

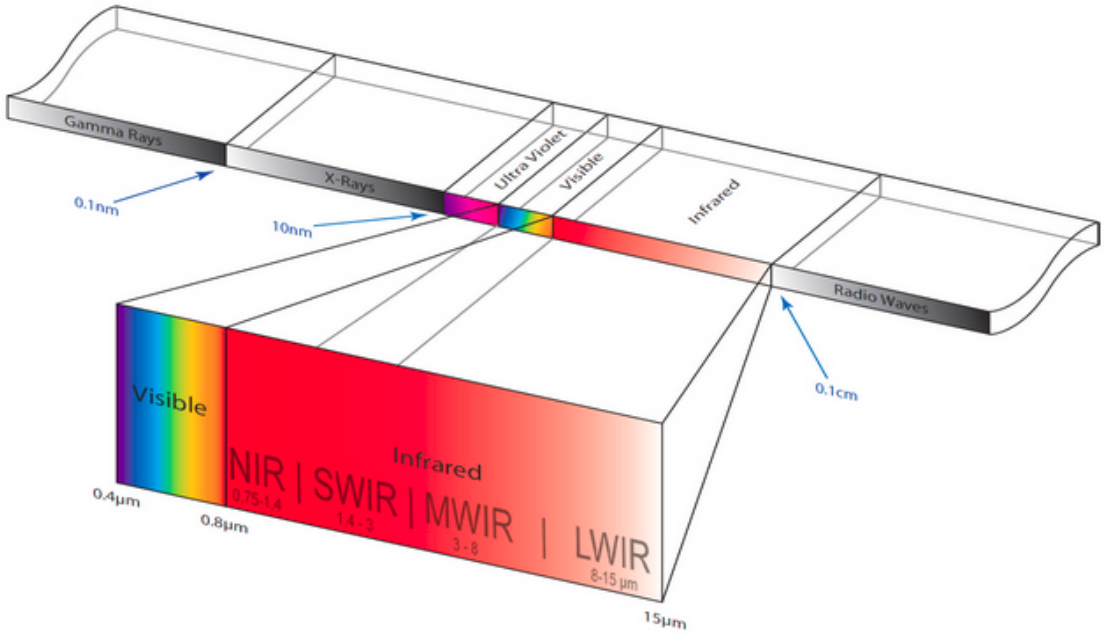

Figure 4.1: Cartoon of the electromagnetic spectrum, separated by bands. The visible and infrared portions are expanded and labeled. [82]

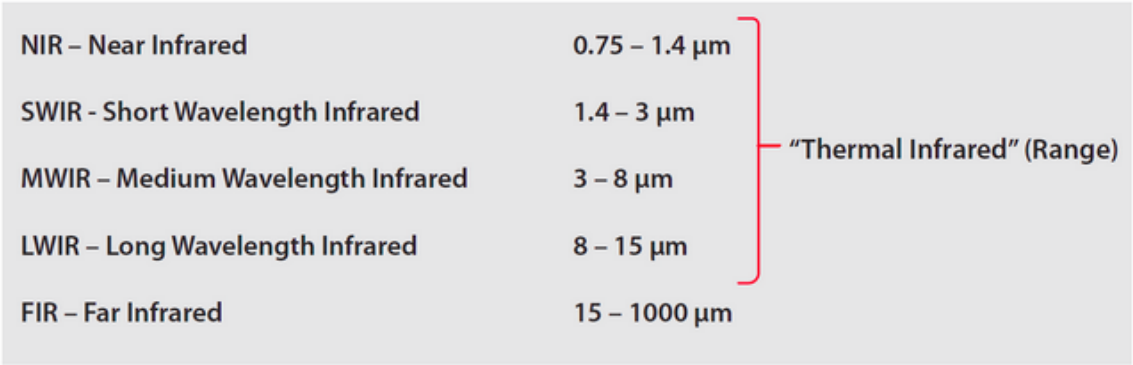

Figure 4.2: Named sections of the infrared portion of the electromagnetic spectrum and their associated wavelengths. [82]

Utilizing the IR portion of the electromagnetic spectrum for imaging endows multiple unique advantages over other spectral bands for applications across industry and defense. While the visible light spectrum is natively accessed by human vision, objects often become obscured in environments which are cluttered, contain haze or fog, or are missing an illumination source such as night-time conditions with heavy cloud cover. IR radiation can penetrate through fog and haze, and has the ability to passively image an object - meaning that no illumination source is required. This is because IR imagers give the ability to detect heat signatures which naturally radiate from warm objects. Figure 4.2 lists the names and acronyms for the various IR bands as well as the wavelengths which they span. Figure 4.3 shows the typical temperature ranges that can be detected with sensors which operate in each band.

Additionally, more information can be extracted from an IR image than just the picture, specifically because these images display heat signatures, and heat is a time dependent quantity. For example, it may be possible to determine if a parked car has been recently operated due to the front end or tailpipe showing a strong IR signature.

However, detection of the IR portion of the electromagnetic (EM) spectrum is a challenge. IR photons are of very small energy ($< 0.5eV$). These optical energies overlap with room-temperature vibrational energies of crystal lattices, so that the signal from the addition of an IR photon is lost among the vibrational energies. Because of this, it is currently necessary to cool IR detectors to very cold

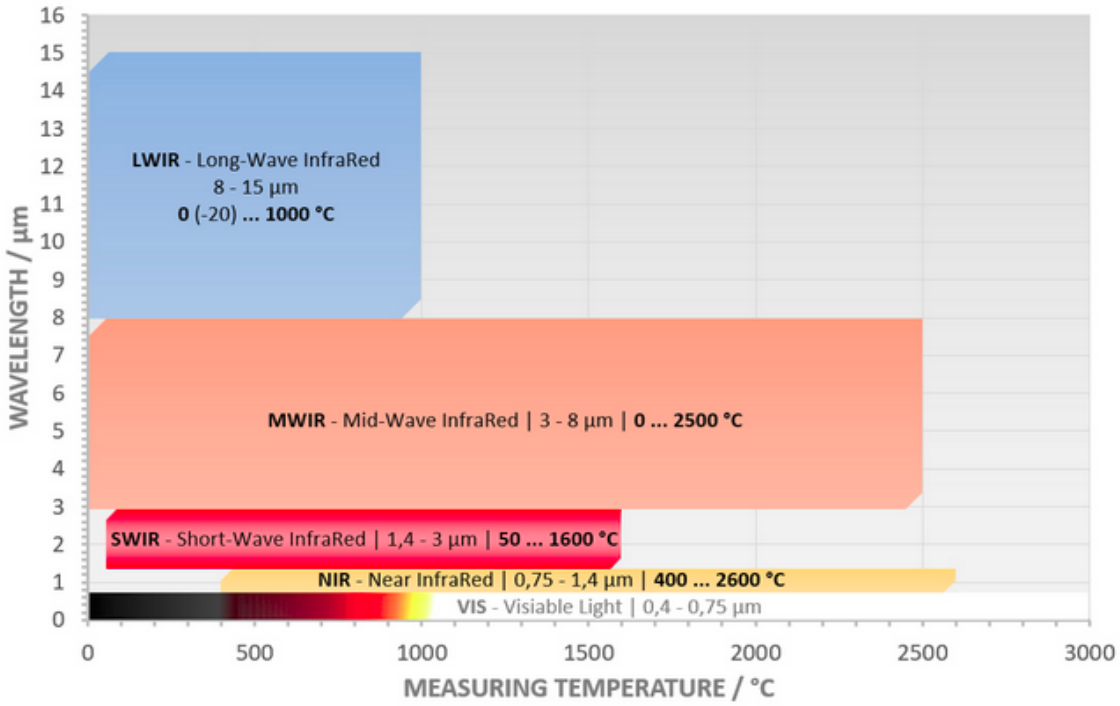

Figure 4.3: Diagram showing typical temperature ranges covered by different spectral responses of infrared radiation temperature measurement devices. [82]

temperatures to reduce the vibrations of the atoms in the detectors that occur at ambient temperatures.

Utilizing nanostructured materials can eliminate the need for cooling in IR photodetectors by changing the allowed vibrational modes of the atoms and shifting the energies of phonons away from the IR photons of interest. Introducing restrictions in the spatial dimension eliminates one major problem but introduces new challenges: everything EM related becomes localized. Charge carrier excitations are long lived but confined, reducing the amount of signal that can be read out. Surfaces, low coordination corners and edges, and dangling bonds affect chemical stability and destroy the ability to absorb photons.

The lead salts, PbS, PbSe, and PbTe have band gaps ranging from 0.44 eV to 0.34 eV and absorb in the SWIR [83]. All three PbX, in bulk and nanostructure form, have been utilized in IR sensing and emitting devices [84] [85] [86] [87]. PbTe is also known for its excellent thermoelectric properties [88], and PbSe has been extensively studied for its deviant electronic properties [89] [90]. All three PbX compounds

crystallize in the rock salt structure, a face centered cubic (FCC) lattice. Unlike other semiconductors, the band gap occurs at the L point in the Brillouin zone instead of the usual Γ point. There is an 8-fold degeneracy at the L point, due to four symmetric L points plus their spin. Recent studies have shown the importance of symmetry effects as well as orbital overlap, as they cause the gap to occur at the L point [88]. The effect of the L point transition alters the electronic transport through PbX nanostructures as compared to other commonly used photosensitive semiconducting materials.

Recently, the Wuttig group have discovered that the nature of the bonding in bulk PbX materials does not fall into known classifications such as ionic, covalent, or metallic bonding, but a novel type of bonding they call metavalent bonding [91] [92]. All three PbX bulk materials have been shown to demonstrate this type of bond [93]. These studies have not yet investigated the effects of metavalent bonding in the nanoscale, begging the question about its survival in low dimensional structures. As the unique characteristics of metavalent bonding have been shown to have a large impact on the optical properties of a material [94], special attention is given to the bonds within the nanoscale models studied here.

Working towards the use of PbX nanostructured materials in IR detectors, devices have been fabricated and characterized which show good response and high gain, but poor on/off times [95] [96] [97]. The poor on/off times are related to the charge transport, so that understanding and improving charge transport from and through nanostructures is crucial to overcome this poor device quality. The conditions impacting charge transport across the QD interface specifically in materials which exhibit room temperature IR detection has become a major field of study [98] [99] [37]. Inherent to the interface are the consequences of low-coordination atoms which form the surface of each nanostructure. To better understand the electronic environment of the surface we study 2D slabs and a 64 atom cube where the contributions from individual atoms of various coordinations can be separated and studied. PbS has been chosen as the test subject with the knowledge that PbSe and

PbTe structures will be similar. A study of the differences between the three PbX in nanostructures is a topic of future work.

In the following, an investigation of PbS quantum dots is undertaken with focus on the effects of atomic coordination, stoichiometry, and orbital interaction on the electromagnetic properties as well as the carrier wave functions. DFT has been used to calculate the ELF, wave functions, electron charge density, and density of states of PbS toy models which are representative of QD surfaces.

4.2 Applications

Optical technologies in the IR portion of the electromagnetic spectrum are a valuable tool becoming increasingly utilized across the modern technology space. Due to the wavelength of the signal, it propagates well through the atmosphere, better than visible light, while still allowing for significant data transfer, more than can be achieved in radio frequency waves. These properties make IR wavelengths a prime candidate for telecommunications technologies. Solar-energy harvesting benefits from the high transmission of IR through the atmosphere. Manufacturing processes utilize the IR for quality control to identify defects and faults at various stages in production. There are numerous biomedical imaging applications in the IR as well, as these wavelengths can transmit though living tissue. A particular advantage is for object recognition in low visibility environments such as clutter, dust, smoke, fog, haze, and low light conditions. Because of this IR imagers have been used in self-driving vehicle applications and forest fire operations.

The IR spectrum spans the wavelengths from 800 nm to 10000 nm (0.8μm to 10μm) and is broken into bands dictated by atmospheric transmission. Due to the chemical makeup of the atmosphere there are spectral regions which absorb rather than transmit IR radiation and are not accessible for IR detectors. Absorption due to carbon dioxide is the major cause of attenuation, and significantly blocks IR transmission from 1.7-3μm. In figures 4.1 and 4.2 the major bands of EM radiation transmission are shown within the electromagnetic spectrum as a whole and given

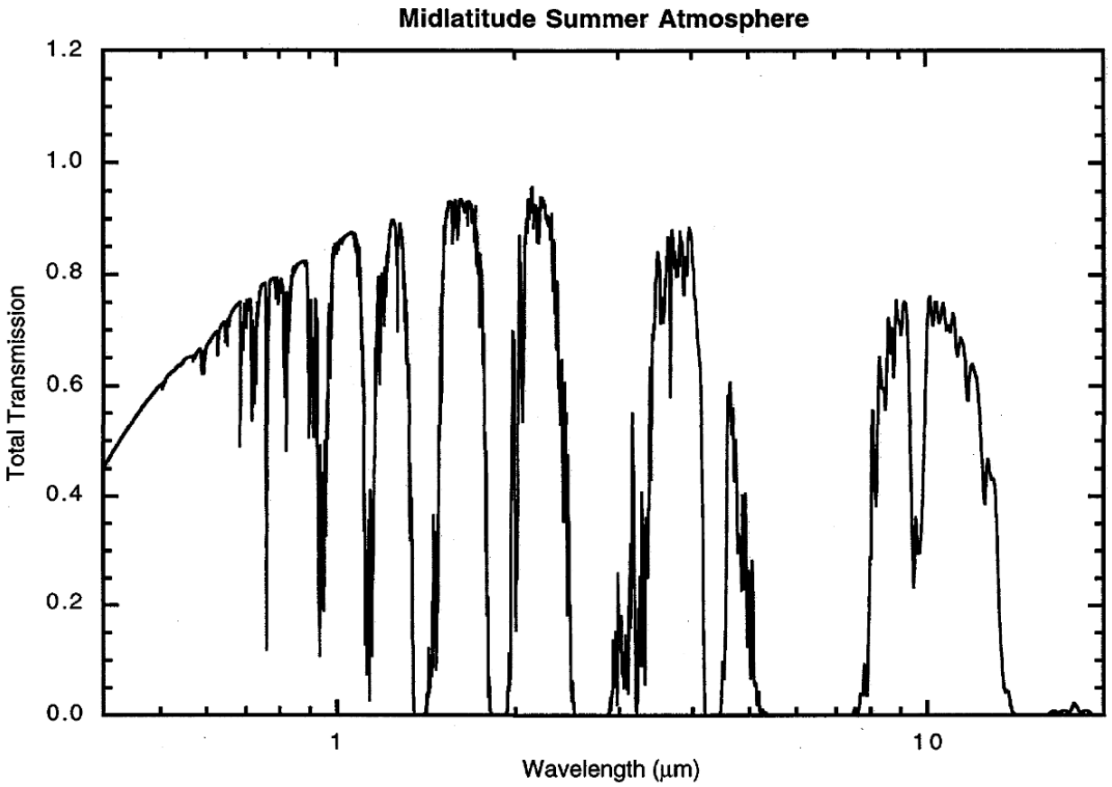

Figure 4.4: Typical atmospheric transmission of visible and IR electromagnetic waves in the midlatitude summer model. Reproduced with permission from [100]

in a list. In practice these ranges are not absolute and for any given climate/weather condition may be less than or extend past these ranges. Figure 4.4 shows the typical atmospheric transmission of visible and IR electromagnetic waves in wavelength.

The energy ranges that correspond to the IR wavelengths cover the energies we as humans most commonly associate with heat. For example the average human body is around 98 ° F or 310 K which translates to 9.34μm or 0.13eV. This falls in the LWIR portion of the spectrum.

Since hot objects naturally emit EM radiation in this range, IR imaging can be active or passive. Active imaging is what traditional visible cameras utilize; it requires an illumination source. For example a visible spectrum picture can only be taken when there is a light shining on the scene. In the IR range active imaging often involves illuminating an object with an IR laser. Passive imaging does not require an illumination source. No matter the illumination conditions (too little or too much background visible light) an image can be captured.

Since the IR spectrum allows the discernment of changes in temperature it can

also give more information about an object than what is seen in a visible spectrum image. However, any user of electronic devices is familiar with the problem of the device heating up as the operating time increases. Since IR cameras detect heat this internal heat shows up as noise and can completely ruin the functionality of the device. Noise in any type of information can have negative effects from distorting and hiding the signal up to destroying the ability to get any information at all. Examples of the types of noise specific to light detectors are given in the next section. In current IR camera architectures which operate based on absorbing EM radiation, the detector must be cooled to at least a lower temperature than the "heat" it is trying to detect, and often to a significantly lower temperature.

The equipment required for detector cooling is expensive and very delicate. This limits the availability and proliferation of good IR imagers. We will outline what requirements an imager must satisfy to be categorized as 'good' in the next section. For some applications it takes more than just good light absorption for a detector architecture to be useful. There are many places current state of the art devices just cannot be used due to complexity or cooling requirements.

4.3 Figures of Merit and Requirements

4.3.1 Figures of Merit

As there are multiple materials and architectures which result in successful IR detectors, particular properties have been identified and established in the field as identifying characteristics for IR detectors. The following figures of merit are outlined in ref [101]. These figures of merit are used to compare IR detectors to one another, determine how well they can capture IR light, and describe how well they produce usable signal.

- **Responsivity** is a measure of how much electrical signal output is generated per optical signal input. In technical terms, responsivity is equal to the ratio of photocurrent to the optical power impinging on the detector and is measured

in units of A/W.

- **Noise** is the amount of output signal that is not generated from input illumination. Intrinsic to the detector body itself there are various distinguished sources of noise:
  - Johnson/Nyquist noise is the fluctuation caused by thermal motion of the charge carriers in a resistive element. Local random thermal motion of carriers sets up fluctuating charge gradients, even though charge neutrality exists generally across a resistor. The current-noise expression is $i_j = \sqrt{\frac{4kT\Delta f}{R}}$
  - shot noise is associated with the DC current flowing across a potential barrier and is a series of independent events. The current through the diode possesses this noise because the charge carriers cross a potential barrier. The current-noise expression is $i_s = \sqrt{2q\bar{i}\Delta f}$
  - generation-recombination noise results from statistical fluctuation in the rate of generation and rate of recombination of charged particles into an upper state within the detector material. These variations may be caused by variations in carrier lifetimes or the random-generation process of the carriers. $i_{gr} = 2qG[\eta E_q A_d \Delta f + g_{th} A_d \Delta f \ell_x]^{1/2}$
  - 1/f noise is a strong function of frequency, most important at low audio frequencies. The noise power is approximately inversely proportional to the frequency. $i_f \alpha \sqrt{\frac{\bar{i}^{\,2} df}{f^{\,1}}}$

  The minimum optical power level a detector can discern depends on the responsivity and the noise level.

- **Signal to Noise Ratio (SNR)** - $SNR = RP/i_n$ the optical power at which the SNR is equal to unity is the minimum optical power that the detector can discern

- **Noise equivalent power (NEP)** is a specific measure of the SNR, at which

conditions where the SNR equals one. This is special because the minimum optical power level a detector can discern depends on the responsivity and the noise level; the signal produced must be above the noise level to be reliably detected. $NEP = i_n/R$

- **Specific Detectivity**, or normalized detectivity D* is a measure crafted by Jones [102] as a universal way to compare any photoconductive material. D* = equation. In technical terms D* is the SNR produced by a detector of $1cm^2$ surface when 1W of optical power impinges, measured with electrical band width of 1 Hz

- **Quantum Efficiency** is the efficiency with which an incident photon results in the excitation of an electron. It is a normalized value and is equal to the number of electrons excited divided by the number of photons incident of the detector's active area. This quantity typically includes reflectance, absorbance, and scattering.

4.3.2 Requirements

What are the fundamental specifications a light detector should satisfy to be considered a candidate for imaging applications? This question was explored for the case of image sensor technology by the authors of [96]. They have identified three prominent requirements:

- **Sensitivity** – the detector needs to have low noise values compared to its responsivity. Sensitivity is the capacity to distinguish an incident signal from noise. The higher the sensitivity of a device means that less signal is required in order to create an image. Higher sensitivity is also related to a higher signal to noise ratio at brighter illuminations. Within in this requirement is the need for large photoconductive gain, which is a greater than unity ratio of the number of circulated charge carriers per absorbed photon G = carrier lifetime/transit time.

- **Frame Rate** - ideally this needs to match the eye's refresh rate. The temporal response of the photodetector must be sufficiently rapid that within a period of a small number of frames (typically 5) no photocurrent remains that is visible to the eye. The photocurrent time constant should be no longer than a few tens of milliseconds.

- **Integration** - readily monolithically integrated with a simple, low-cost CMOS readout integrated circuit. Low fabrication cost, low complexity, and high pixel count

4.4 Types of Detectors

There are two primary operating mechanisms for light detectors [101]. PbS QD's have been built into both.

- **Photoconductor** - Semiconducting material and two ohmic contacts. Upon illumination the conductivity of the material changes due to a change in mobility or carrier density or both. Conductivity increase upon illumination is most typically attributed to generation of electron hole pairs resulting in carrier density increase.

- **Photovoltaic or Photodiode** - junction between two different semiconductors (heterojunction), or a semiconductor with opposite doping levels (homojunction), or a semiconductor and a rectifying metal contact (Schottky junction). In each case the principle is separation of the photo-generated electron hole pairs by the action of the built-in electric field in the junction and transport of the carriers to the respective contacts for extraction.

4.5 Current State-of-the-Art IR Detectors

The current best performing material for IR detectors is HgCdTe. Despite the difficult process required to produce a HgCdTe detector array and the required

low operating temperature (<100 K), the performance of HgCdTe exceeds other available IR absorbing materials (see table 4.5) [106]). The most advantageous characteristic is the long charge carrier lifetime over all spectral bands that give HgCdTe such high performance. However alternative candidates are emerging from the ongoing research. The development of superlattices composed of III-V alloys (type 2 superlattices) are generally regarded as the second best IR absorbing material class [105]. Superlattices are plagued by short charge carrier lifetimes, but this disadvantage can be mitigated somewhat by engineering of the layer thicknesses. The primary advantage of superlattices is the cost reduction of focal plane array fabrication as compared to HgCdTe devices.

To be truly disruptive to the HgCdTe IR detector market, an emerging technology would need to operate at room temperature, be easily fabricated on a large scale, and be compatible with silicon-based read out circuitry. Solution processed QDs meet all of these criteria. Their major drawback lies in the second requirement of 4.3.2: frame rate. The temporal response of QDs, specifically the fall time, is currently too long to allow for real time video imagery. This is related to the strong

Photoactive Material	Responsivity (A/W)	Specific Detectivity D* ($cmHz^{1/2}W^{-1}$)	Quantum Efficiency (%)	Temporal Response (fall time)
HgCdTe	-	3×10^{12}	80	10 μs
InAs/GaSb SL	-	1×10^{12}	50-60	1 μs
InAs/InAsSb SL	-	4×10^{11}	40	1 μs
PbS-QD/graphene [95]	5×10^{7}	7×10^{13}	25	100ms - 1s
PbS-QD [103]	1	8×10^{11}	80	10ns
PbS-QD/graphene [104]	6.81	-	940	3.2s

Table 4.1: Properties of various IR photodetectors. HgCdTe and InAs SLs were measured at 77 K and at longer wavelengths (10μ) ref [105]. The rest are solution processed devices measured at room temperature in the SWIR range (1.4-1.7μm).

quantum confinement within the QD which leads to advantageous long charge carrier lifetimes. One approach is to deposit the QDs in solution on top of a layer of graphene and allow them to dry into a thin film. As can be seen in table 4.5 the results are promising. However these architectures are far from optimized.

As outlined in ref [107] there are many challenges remaining to be addressed in QD photodetector materials and architectures, including: a deep theoretical understanding and experimental investigation on the response time; simultaneous high R, high D*, and fast response time; a proper and universal surface passivation strategy; and appropriate deposition thickness of QD films for best performance. To understand how to facilitate better photodetector properties, we must first understand the local electronic environment within the QD. This study of PbS toy models aims to investigate at the most basic levels the local electronic environment unique to nanostructured PbS QDs.

4.6 Literature review and background

In 1974 Richard Dalven at the University of California wrote "The IV-VI compounds lead sulfide, lead selenide, and lead telluride, often referred to collectively as the lead sulfide group or the lead salts, are extremely interesting semiconductors." [83] At that time there had been over 20 years of intense work on the lead salts which has since continued into an ongoing field of study. Dalven's review in 1974 along with Ravich's two part review in 1971 [108] [109] demonstrate the unique physical characteristics of the lead salt materials. In the 20th century they were intensely studied in bulk form and thin films due to their small band gap which has applications in infrared detection and solar energy harvesting technology. Many of the properties of the lead salts were known and reported on in Dalven's review, including the unusual electron configuration, non-parabolic conduction and valence bands, the dependence of effective mass on carrier concentration, low values of the TO phonon frequency at Γ, and high static dielectric constants.

In paying particular attention to scattering and transport phenomena Ravich

found that the non-parabolicity of the energy bands manifests in the k-dependence of the Bloch wave amplitudes which changes the wave-vector dependencies of the matrix elements describing phonon-carrier interactions. In other words the root cause of the anisotropic effective mass and anharmonic bonding lies in the non-parabolic energy bands. They find a significant amount of free carriers present in all the samples they studied which makes screening effects essential. These screening effects have a direct influence on the transition probability and the dispersion of optical modes in the long-wavelength region and are tied to the difference in static dielectric constant and optical dielectric constant. It is shown that the deformation potential constant can be used as a fitting parameter to match the theory to the experimental data.

However despite all of the experimental and theoretical analysis there were still contradicting views on some of the basic properties. One debate was, and could be argued still is, the nature of the bonding. Dalven labels all three PbX as polar semiconductors explaining that the inter-atomic bonds in these crystals are predominantly ionic in character. He cites multiple pieces of evidence for the ionic nature including: the sixfold coordination, a heavy concentration of charge around the Te atoms in PbTe, large values for the electron-optical-polaron coupling constant, the large difference in static dielectric constant and optical dielectric constant $\Delta\epsilon$ which is a measure of ionic polarizability, and strong absorption of far infrared photons by transverse optical phonons. Ravich however believed that the bonding was predominantly covalent in nature based on the analysis of carrier scattering which emphasizes the role of acoustic phonon scattering.

A more modern analysis of the characteristics of the bulk form of these materials was reported on by Wei and Zunger in 1997 [89], where they explained the anomalous structural and electrical properties via an analysis of the symmetries in the electron energy bands. Their calculated relativistic band structure for the three materials are shown in figure 4.5. The Pb-s band is fully occupied in all three PbX and lies below the valence band maximum (VBM). This has a profound effect on the band

edge states, which are predominantly made up of p states, causing the direct gap to lie at the L point within the Brillouin zone (BZ)

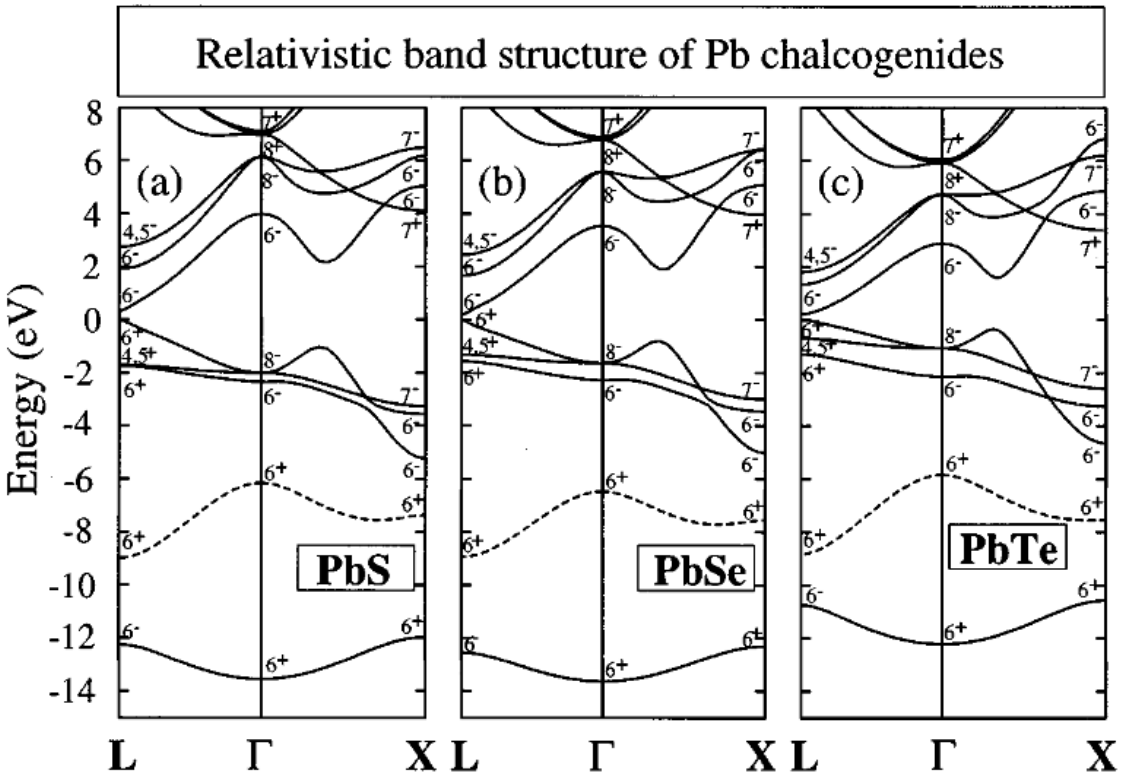

Figure 4.5: Calculated relativistic electronic band structure of (a) PbS, (b) PbSe, and (c) PbTe. Origin of the coordination is at the cation site. The occupied Pb 6s bands are denoted by the dashed lines. The valence band maximum is at zero. Reproduced with permission from [89]

In 2020 Brod et. al. [88] have reexamined the band edge states in bulk PbTe and found that p orbital mixing in a σ bonding configuration between Pb-p and Te-p states is the driving cause for the gap to lie at the L point, more than the s state interactions. The Pb-s states are shown to be in an antibonding configuration with the Te-p orbital however, in agreement with Wei and Zunger. Figure 4.6 shows the interactions of the Pb and Te s and p orbitals when considered separately, allowing the authors to distinguish which interactions cause the behavior of the band edge states.

In Cagnoni 2018 [110], a series of studies began by the Wuttig group on the chemical bonding mechanisms in bulk phase-change materials which discovered a new type of bonding in this class of materials they call incipient metals. PbS,

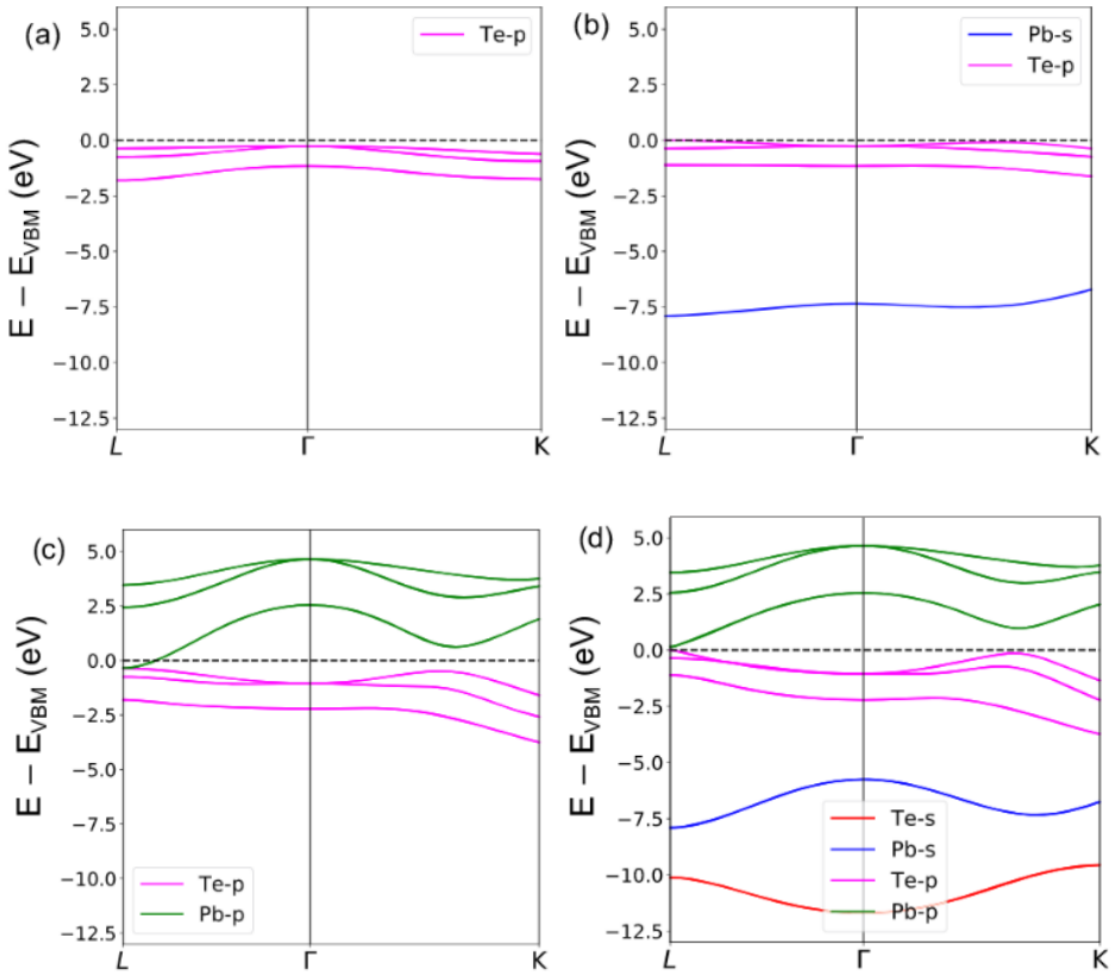

Figure 4.6: PbTe electronic dispersions calculated through the TB approximation (with SOC) with various atomic orbital states omitted. The line at $E - E_{VBM} = 0$ represents the Fermi level for the full electronic dispersion. (a) Band structure including only the Te-p states. The top of the valence band runs down from Γ to L. (b) Only the Te-p and Pb-s states are included. The top of the valence band runs up from Γ to L. (c) Te-p and Pb-p states are included. The VBM is at L. (d) All states are included. Reproduced with permission from [88]

PbSe, and PbTe were found to fall into this new class of materials which exhibit 'metavalent' bonding. The most intensive studies were performed on GeSe and GeTe, which share many of the same properties as the Pb compounds. The primary physical property being investigated in the study was thermoelectric performance, but the overall findings from the study, and the follow on work, have relevance to the lead salts. They found no significant charge transfer between atoms, as is the case in ionic bonding, with each atom possessing an average of three valence p electrons. The bonds to the six nearest neighbors are made up of p orbitals in the σ

	Ionic (e.g., NaCl, MgO)	Covalent (e.g., Si, GaAs)	Metavalent (e.g., GeTe, PbTe)	Metallic (e.g., Cu, NiAl)
Electronic conductivity (**electrical identifier**)	Very low ($<10^{-8}$ S cm^{-1})	Low to moderate (10^{-8}–10^{2} S cm^{-1})	Moderate (10^{2}–10^{4} S cm^{-1})	High ($>10^{5}$ S cm^{-1})
Effective coordination number[a] (**structural identifier**)	4 (ZnS), 6 (NaCl), 8 (CsCl)	8–*N* rule typically satisfied	8–*N* rule not satisfied	8 (bcc), 12 (hcp/fcc)
Optical dielectric constant ε_∞ (**optical identifier**)	Low (≈2–3)	Moderate (≈5–15)	High (>15)	—[b]
Born effective charges Z^* (**chemical bond polarizability**)	Low (1–2)	Moderate (2–3)	High (4–6)	—[b]
Mode-specific Grüneisen parameters (**anharmonicity**)	Moderate (2–3)	Low (0–2)	High (> 3)	Low (0–2)

[a]For ionic and metallic systems, representative structure types are given, but there are many others especially for multinary systems (e.g., in Zintl phases); [b]This indicator is not normally applicable to the metallic state.

Table 1: Property-based “fingerprints" to define bonding in inorganic metals. The fingerprint for metavalent solids is a combination of five different identifiers, all of which need to be present in a given material (e.g. NaCl and PbTe have the same structural identifier, but the electronic conductivity of NaCl is extremely low). [92]

bonding configuration with an average of one electron per bond; which is different that covalent bonding which has an average of two electrons per bond. The soft bonding leads to a slow phonon group velocity, which leads to small lattice thermal conductivity and a highly anisotropic effective mass tensor.

In Wuttig 2018 [92], five distinct characteristics of metavalent bonding are proposed (table 1): the electric conductivity, the effective coordination number, the optical dielectric constant, the Born effective charge (a measure of chemical bond polarizability), and the Gruneisen parameter (which is a measure of anharmonicity). An emphasis is made on the distinction between metavalent bonding and resonant bonding, as the characteristics between these two types of bonding appear similar. However as illustrated in figure 4.7, resonant bonding is specific to systems with large electron sharing in the form of π bonds or hybridized sp^2 bonds, whereas metavalent bonding originates from neither of these bonding mechanisms.

In Raty 2019 [111] this same group of authors goes on to quantify chemical bonding, including metavalent bonding, through the parameters electrons shared (ES) and electrons transferred (ET). Plotting materials as functions of these two values creates the map in figure 4.8. This figure is plotted again in figure 4.45, however with lines to guide the eye along two separate approximate slopes: one slope runs from 2.0 on the y-axis to 1.0 on the x-axis and connects the covalent bonding and ionic bonding materials; The second slope runs from 1.0 on the y-axis

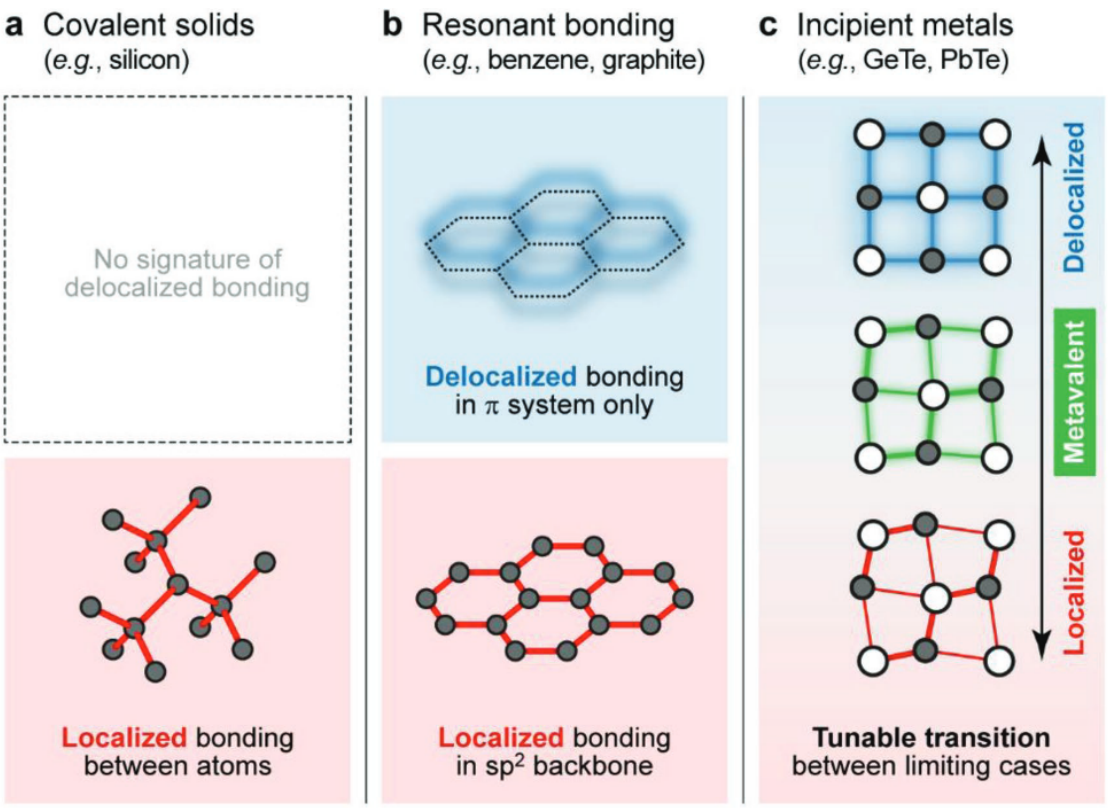

Figure 4.7: Schematic of bonding in covalent and resonantly bonded systems versus incipient metals. a) Covalent solids, e.g., diamond-type silicon, form strong and localized bonds only. b) In benzene and graphite, both localized sp^2 bonding (red) and delocalized π bonding (blue) exist, but the corresponding orbitals are orthogonal. c) By stark contrast, incipient metals are located between both limiting cases, but with unique properties that are observed only in the intermediate region of metavalent bonding (green). This transition can be tuned, for example, through pressure-induced structural transformations, but the mere presence of a phase transition is not a necessary criterion. For example, PbTe is undistorted but still shows fingerprints of metavalent bonding. [92]

almost horizontally across and connects the metavalently bonded materials. These slopes highlight the fundamental difference between the metavalent bonding and covalent/ionic bonds. In covalent/ionic bonding, it is primarily the electronegativity of the constituent atoms which determines the degree of ES and ET; with a tendency for either predominantly ES character (covalent) or predominantly ET character (ionic). In metavalent bonding, it is the alignment of atomic p orbitals and the balance between ES and ET which creates the bond, causing a different slope on the ES vs ET plot (figure 4.45). This difference can quantitatively be seen by the number of electrons involved in the ES and ET. For covalent bonds, ES involves

close to 2 electrons. For ionic bonds, ET involves close to 2 electrons. For the metavalent bonds, ES is close to one electron and ET is less than one electron.

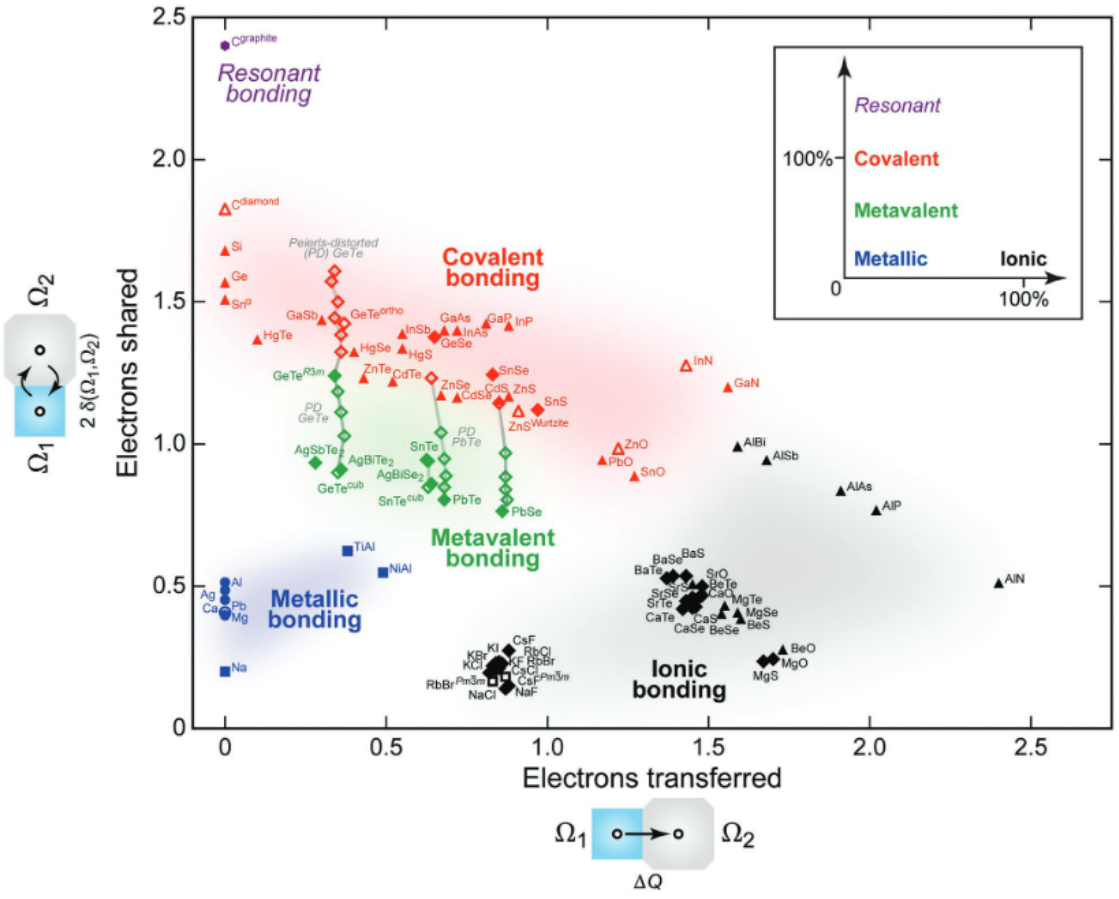

Figure 4.8: A 2D map of electronic interactions and bonding in materials. The amount of electrons transferred (x-axis) and shared between neighboring basins (y-axis) is computed using quantum-topological methods; they serve as quantitative measures for the ionic and covalent characters, respectively. Symbols indicate structure types: "sp3"- (tetrahedrally) bonded solids are shown as triangles, distorted and ideal rocksalt-type (octahedrally coordinated) structures as diamonds, body-centered ones as squares, and close-packed metal structures as circles. Filled symbols denote thermodynamically stable phases (at zero temperature); open symbols denote metastable phases. For GeTe, SnTe, PbTe, and PbSe, additional structural intermediates have been generated along the Peierls distortion coordinate (gray lines as guides to the eye). The sketch in the inset summarizes the qualitative conclusions drawn from this map: we consider $2\delta(\Omega_1, \Omega_2) = 2$ to correspond to the sharing of a full electron pair, and therefore label this as "100 %." Resonantly bonded graphite sheets exhibit more than this one electron pair shared between the atoms; metavalent materials have distinctly less. [111]

The work on metavalent bonding has been done in the bulk materials, but at this time no study of nano-sized geometries has been published. The structural, optical, and energetic properties of small systems can be drastically different that

what is seen in the bulk. For PbX, with their intrinsically large Bohr radius of the exciton, the development of synthesis into quantum dots in the late 1980s allowed for spatial dimensions smaller than the Bohr radius and caused the lead salts to be at the forefront of the effort to understand quantum confinement in semiconductors [112]. The earlier treatments used to model these quantum-confined structures defined different regimes of confinement and used simplifications in their modeling approaches. In 1982 Efros and Efros published a general study [113] of interband light absorption in a semiconductor sphere. Three regimes were obtained for the absorption coefficients of light: when the radius of a semiconducting sphere $\boldsymbol{a}$ is less than the Bohr radii of electrons and holes; when $\boldsymbol{a}$ is larger than the hole and smaller than the electron, and finally when both the hole and electron are smaller than $\boldsymbol{a}$. The lead salts are in the first case known as the strong confinement regime were the radius $\boldsymbol{a}$ of the QD is smaller than the Bohr radius of the total exciton mass.

Schmitt-Rink et. al. in 1987 [114] did a general theoretical analysis on QD optical properties which predicted fairly accurate behaviors. They found a range of sizes of QDs for which the electronic states are still like those of a crystalline semiconductor while the size of the QD is smaller than the Bohr radius of the exciton. In these sizes the effects of confinement dominate over the Coulomb interaction of the electron and hole so that the allowed optical transitions are between single-particle eigenstates. In their treatment they also find that the electron phonon coupling should not be so large that it deviates much from what is seen in the bulk, however the broadening due to phonons is inevitable. They predicted that the lowest interband transition will take on a very simple two-level system like behavior.

In 1997 Kang and Wise [34] published their intensive calculations of spherical PbS and PbSe QDs with a four-band envelope function formalism. They show that effects of band structure anisotropy are negligible for the CBM and VBM j=1/2 states. There is mixing however for the j=3/2 states which is quite small for PbS states but becomes significant in PbSe having the largest effect in the valence states.

In this model, the transition element of the dipole transitions becomes isotropic after summing over the transitions in all four equivalent L valleys. There are two contributions to the dipole moment in lead-salt QDs: one from the dipole moment of the envelope functions which is isotropic in its polarization as a consequence of the total wave functions of both conduction and valence electrons having been expanded in the same set of band edge Bloch functions. The second is from the dipole moment of the longitudinal momentum-matrix elements (taken between the extremal valence and conduction band states) Bloch functions and is polarized along one of the four [111] directions before being summed over the four equivalent valleys and is proportional to the overlap between electron and hole envelope functions. Overall they find the many-body perturbations due to Coulomb attraction (10-100meV), exchange interaction (1-10 meV), and intervalley scattering (1-10 meV) are insignificant compared to the confinement energy (1 eV).

In 2000 Wise [33] did a thorough review of the strong confinement regime in lead salt QDs. This study also states that the electronic energies are determined primarily by confinement (figure 4.9 (b)). The confinement causes the available energy states to become discreet and separate, as shown in figure 4.9 (left). The decreasing available energy states for transitions concentrates the optical transitions into a few narrow energy intervals causing strong absorption of specific wavelengths of light (4.9 (a)). In this regime light always interacts with one electron-hole pair regardless of the size. As long as the QD transitions do not become too broad nonlinear optical effects are possible. In the lead salt QDs the six fold crystal structure of the bulk is maintained and so every interior atom is at a site of inversion symmetry. Assessing the intrinsic polarity of strongly size-quantized electron states should be feasible. He states that coupling to polar phonons should vanish.

In 2020 Avdeev et. al. [10] theoretically studied the fine structure of lead chalcogenide QDs with a more accurate model that included a reduction of symmetry from the spherical case, but was still limited by only considering models of structures possessing T_d symmetry and equal numbers of cation and anion atoms. They

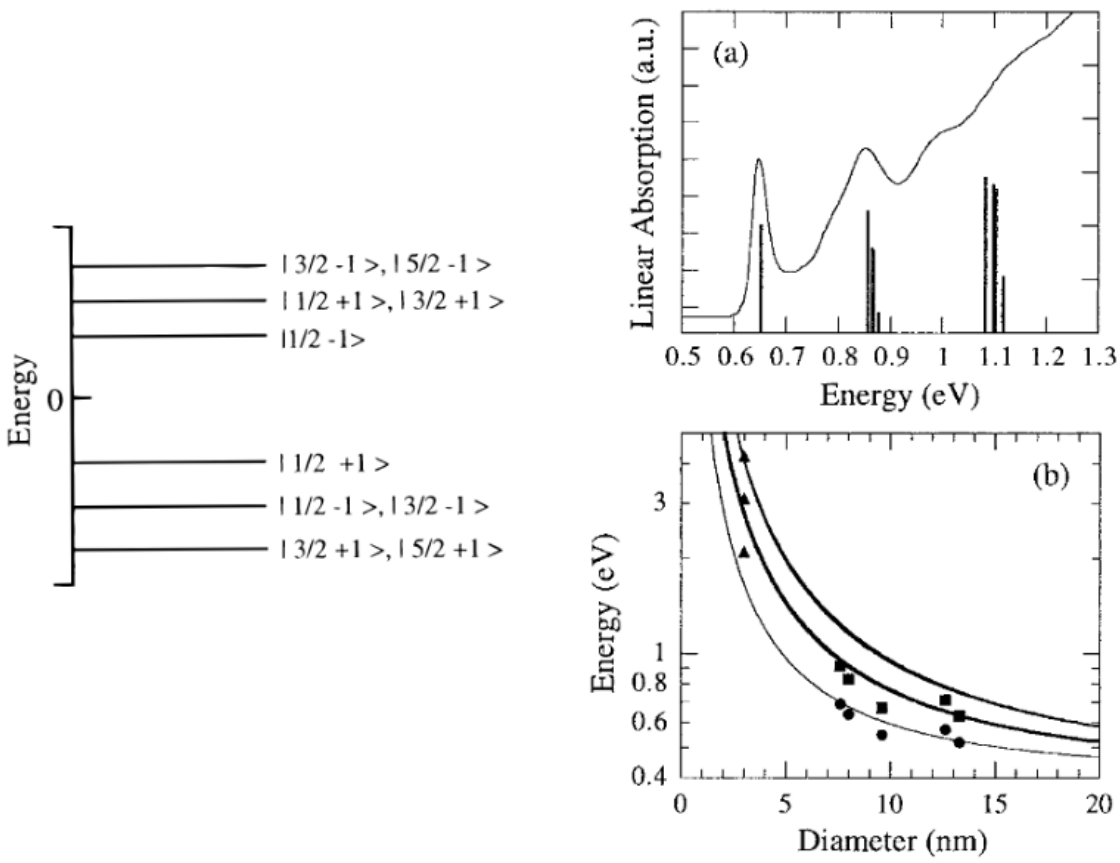

Figure 4.9: Data for PbS QDs from ref [33]. Left: General form of the first few electron and hole energy levels of PbS or PbSe QDs. The states are labled by the quantum numbers j (total angular momentum) and π (parity) $|\, j\pi\rangle$. (a) Absorption spectrum and calculated transition strengths of 8.5-nm-diameter PbS QDs in oxide glass. (b) Measured and calculated exciton energies (plotted on a logarithmic scale) as a function of the size of PbS QDs. The dark lines indicate nearly degenerate transitions between the states indicated in figure to the left. Reproduced with permission from [33]

find that the ground state exciton is influenced primarily by electron-hole exchange and valley mixing.

However these models miss the influence of more realistic non-symmetric and non-stoichiometric geometries which would alter the electronic environment within the dot. In quantum dots the lattice symmetry of the bulk is altered by surface termination. QDs have been shown to be crystalline and faceted with clearly recognizable XRD patterns (figure 4.10) [115]. The smallest QDs have been shown to be octahedral in shape with [111] polar facets which are metastable with ribbon-like nanodomains of polarity [116]. The [111] faces are Pb terminated, making the ratio

of Pb to X atoms as large as 3:1 [115]. As the QD grows in size, stable nonpolar [100] surfaces emerge until the cubic shape takes over (figure 4.11). These intermediate shapes have been described by the cuboctahedron geometry [115] [117] and this idealized description is useful for theoretical analyses. The effect of the deviation from stoichiometry in PbS QDs was studied by Kim et. al. in 2013 [118], where they found mid gap states and metallic behavior when the Pb:S ratio became unbalanced.

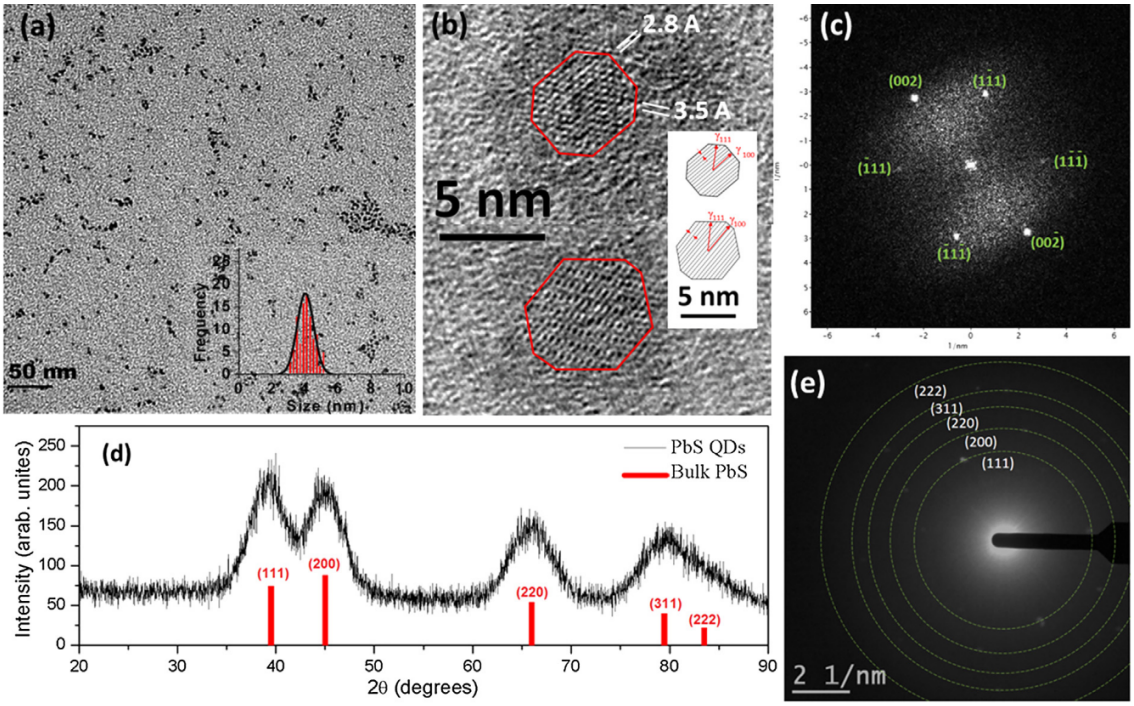

Figure 4.10: (a) TEM image of particles synthesized at 121 degrees C and 16 mins. Based on histogram plotted in inset, mean and standard deviation particle size are calculated 4nm and 12.36%, respectively. (b) HR-TEM images suggest the synthesis of single crystal and octahedron particles, (c) FFT pattern corresponding to the QDs observed in HR-TEM images, (d) XRD spectra and (e) SAED pattern confirm the synthesis of rock salt PbS QDs. Reprinted with permission from Elsevier [115]

The influence of the terminated surfaces plays a large role in the overall electronic properties. In 1999 Shim et. al. [119] studied the permanent dipole moment in colloidal QDs and concluded that these may be intrinsic attributes to all nonmetal particles. Their study indicated that the origin of the large dipole moment is not from the internal bonding structure but that the asymmetry of the overall shape is important. The point group symmetry of the shape along with the bond type drives the dipole moment. Surface localized charges on polar facets may explain origins of

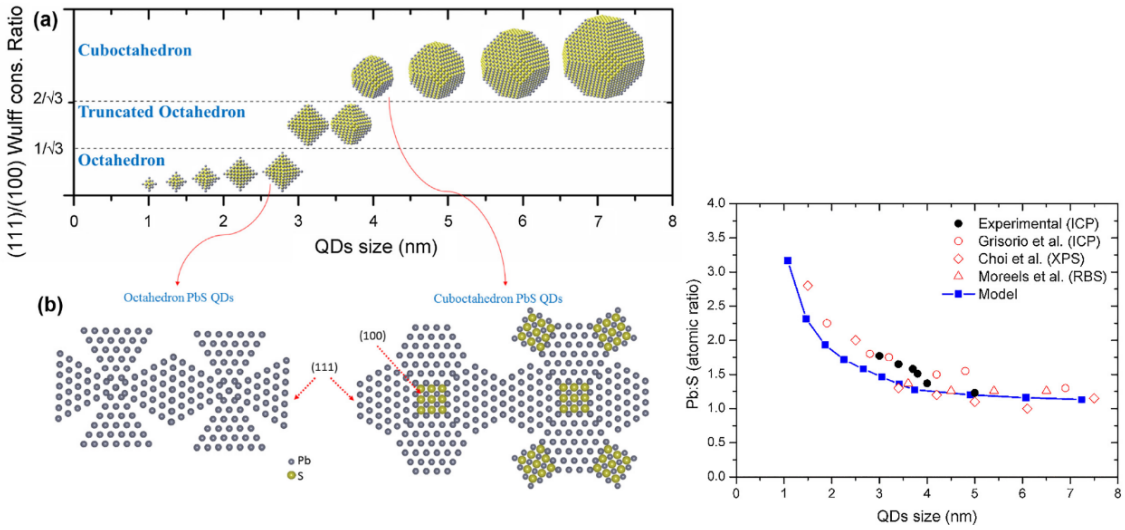

Figure 4.11: (a) Equilibrium shape of 1 to 7.5 nm PbS QDs. (b) arrangement of Pb and S atoms at the surface of octahedron and cuboctahedron PbS QDs. Bottom left: size dependent composition of PbS QDs. Reprinted with permission from Elsevier [115]

a dipole moment.

PbS QDs in one to two layer films were studied optically by Diaconescu in 2013 [120]. The data is taken from a broad distribution of QD samples with band gaps ranging from 0.7-1.2 eV. Results show a symmetric first transition, but the second transition absorption features the authors claim can only be explained by asymmetric transitions involving states of different symmetries. Their reasoning is the following: if anisotropy of electron and hole masses is considered in a model of the transitions in PbSe, the electronic states split in such a way that the 1P hole-1P electron parity conserving transitions occurs near the normally forbidden 1S hole-1P electron and 1P hole-1S electron transitions. However in PbS the splitting is too small. This along with the experimental observations strongly suggests the relaxation of parity conservation in PbS QDs is due to an internal electric field or an asymmetric distribution of atoms relative to the QD center.

In 2007 Harbold and Wise [13] used photoluminesence spectroscopy to study the low-energy states of PbSe QDs of 3.2, 3.7, and 4.6 nm diameter in dried thin films and solutions. They report several significant results. Using low temperature and room temperature spectroscopy allowed for detailed features including observation

of an asymmetric low energy tail in the emission spectra. Upon further investigation with a high photon energy source, this tail was shown to be the splitting of the lowest energy emission feature with a maximum splitting of about 100meV in the smallest QDs. The variation of the splitting with QD size suggests the tail is due to the coupling of equivalent L valleys. Selectively exciting this lowest energy feature showed significant anti-Stokes luminescence. This suggests the role of the surface states in the emission spectra. Additionally they notice that the fluorescence spectrum lines do not narrow as significantly as expected with size indicating a very broad single particle linewidth estimated at 25-50 meV, consistent with PbS samples. A redshift between samples of QDs in solution and QDs in deposited film was observed which is indicative of resonant energy transfer between smaller dots and larger dots in the film. Clark 2007 [121] extensively studied this FRET and a rough calculation resulted in a Forster radius of about 80 Å for PbS QDs.

As shown in theoretical studies confinement does play a large part in influencing the electronic states within nanostructures. Allan and Delerue in 2004 [122] looked at both quantum wells and quantum dots of PbSe to investigate how the rock salt structure behaves under confinement as compared to the more common zinc blende type nanostructures of most semiconductors. In figure 4.12 three planes within the rock salt crystal structure, the BZ, and the band structure calculated by Allan and Delerue are shown. With their analysis they confirm that the electronic states in PbSe are primarily p-like and as a consequence of this (even at the surfaces) the p orbitals remain strongly coupled with orbitals of atoms in the interior and so the [100] surfaces do not introduce states in the energy gap. Colloidal PbSe QDs have shown high efficiency band edge fluorescence and this lack of surface states may be the reason. They calculate the frequency dependent dielectric function for PbSe QWs and find a large anisotropy and large variations from the bulk values. The dielectric function is affected by the polarization of p bonds in different degrees of confinement. They find that critical points along the Σ line in the BZ are saddle points for the band edge states and therefore the effect of quantum confinement depends on the

orientation of the Σ axis with respect to the [001] axis. The confinement in the [001] direction gives rise to a redshift for the critical points in the [110], [-110], [1-10], and [-1-10] directions and a blue shift for others. Saddle points also occur along the Δ directions: the local minimum of the energy gap along [100] is a maximum along [001]. In addition to these features a permanent dipole moment is proposed as contributing to breaking the selection rule which leads to the normally forbidden (s-p) transition of the second peak. Mixing between s and p states in the four equivalent L point extrema is supported by tight binding calculations which show that the lowest conduction states and the highest valence states are grouped into well-defined multiplets of eight levels, but there are splittings in these levels due to intervalley coupling. These splittings result in either a twofold or a fourfold degeneracy.

Indeed the surface is where the bulk physics breaks down. Yazdani et. al. in 2020 [123] found evidence that the fundamental limits to emissions linewidths may be from undercoordinated atoms on the surfaces with localized vibrations coupling to interband transitions. They found a positive correlation between larger QDs and narrower line widths. Delerue in 2003 [124] studied the concept of the dielectric constant for nanosized systems and showed that macroscopic components of the electric field can still be obtained from the bulk dielectric function for sizes larger than 'a few fermi wavelengths', so the first 3-4 layers of the surface do not fall within this regime. These effects may be the missing piece for the open problem posed by Melnychuk in 2021 [15], that there is no good physical description of the effect for the relationship between quantum dot size and lifetime, and that there seems to be a 'universal' lifetime among quantum dots of different materials. Studying the lead salt QDs with their extreme characteristics is a good place to find some answers, as can be concluded by the plethora of work in the literature.

Another important aspect of QDs is the way they may couple to each other within a film. Mobility studies of charge carriers through QD films, the way they are actually used in applications, by Yazdani 2014 [125] shows an increase in hole

mobility with decreasing radius. The QD diameter they studied was between 2.4-4.2 nm so a large portion of these dots would have [111] surfaces. The authors primarily attribute the increased mobility with the increased kinetic energy of a carrier from the higher quantum confinement in a smaller QD. Yang and Wise in 2015 [126] used a tight-binding model to systematically study the effect of structural disorder on the electronic properties of QD films. To examine the conditions for band-like transport they calculated the coupling energy between QDs in film and found the critical disorder which eliminates delocalized states. Short range order has the largest impact as the coupling of distinct valleys uniquely impacts the charge transport through films of QDs.

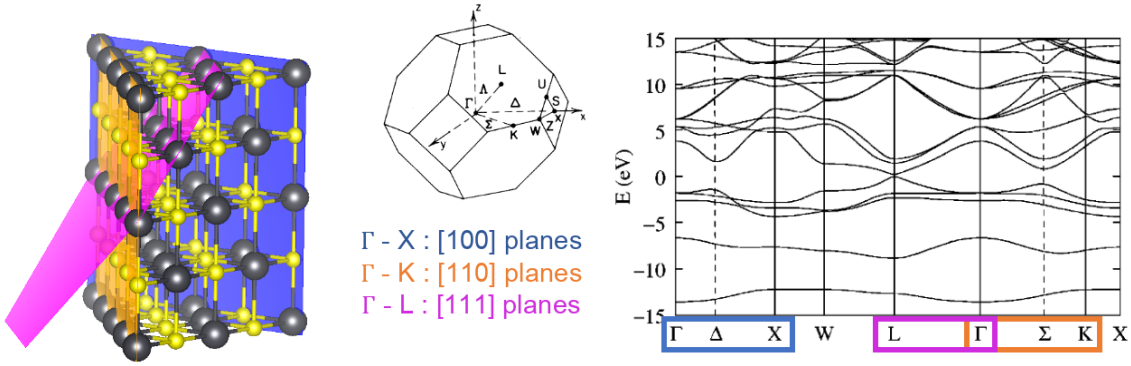

Figure 4.12: Properties of Bulk PbS. Right: Electronic band structure as calculated by ref [122] (Reproduced with permission). Three regions are highlighted by colored boxes on the x-axis labels which correspond to directions in the BZ and planes in the crystal. Center: BZ of bulk PbS and the directions within the BZ which correspond to planes of atoms in the bulk, all in colors matching to the corresponding information in the left and right figure. Right: planes of atoms in the bulk structure. The colors of the planes correspond to the labels of the same color listed in the center of the figure.

As discussed above bulk lead chalcogenides have been studied for decades with a recent discovery finding them to be included in a class of materials called incipient metals. Like other chalcogenide systems, PbS has been shown to exhibit metavalent bonding, a novel type of bonding somewhere between covalent and metallic, where competition between electron localization and delocalization causes unique properties. This type of bonding has brought new understanding into highly debated aspects of PbS properties.

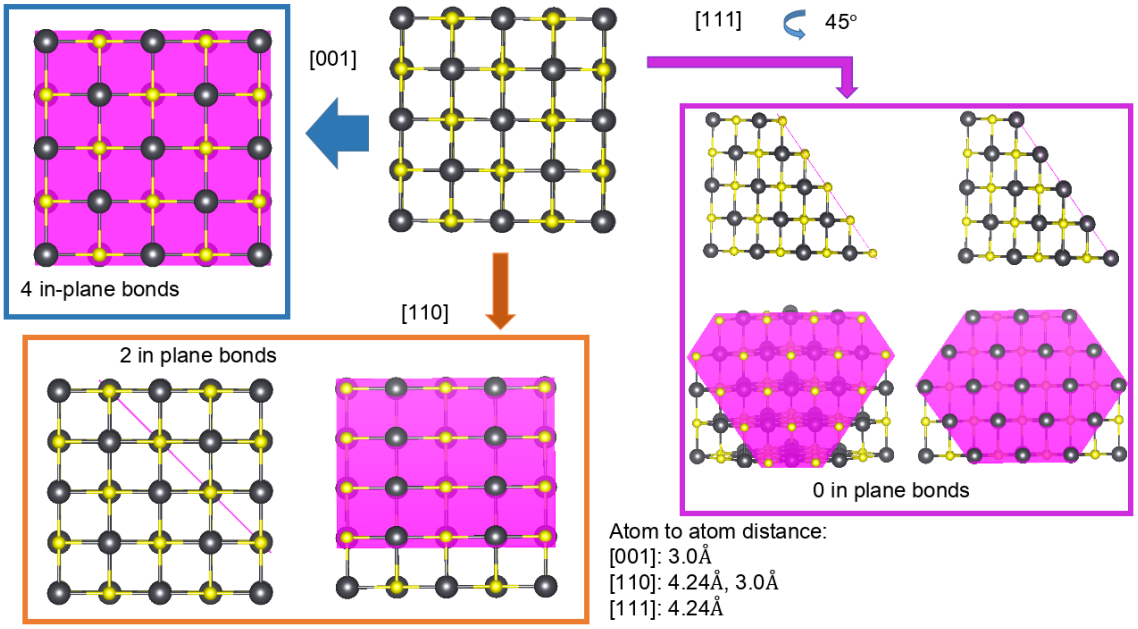

Figure 4.13: Planes in bulk PbS. The colors of the perimeter boxes correspond to the information in figure 4.12. The color of the plane itself holds no information.

The nature of the bonding plays a critical role in understanding the optical behavior of PbS. It is the local atomic arrangement and orbital character of the electronic states which determine the energetic landscape [127]. This governs how the material reacts to incoming light and how, once light is absorbed, excess charge moves through the material.

In the bulk, cubic IV-VI compounds including PbS, PbSe, and PbTe, have cubic atomic arrangement with an average of 3 valence electrons per atomic site. This arrangement leads to half filled p-bands, with the valence band maximum (VBM) mainly consisting of X-p character and the conduction band minimum (CBM) mainly consisting of Pb-p character. It is no surprise then that the bonds in PbX consist of p orbitals, however these bonds contain only one electron in a σ bond. This was predicted in 2004 by Allan and Delerue [122], and confirmed recently by the Wuttig group. These bonds do not conform to the character of covalent, metallic, or ionic bonds and are a balance between electron localization and delocalization. Changes in the atomic arrangement such as Peierls distortions can shift the balance and destroy the metavalent bonding.

Cheng 2020 [128] says that "compounds utilizing half-filled p-p σ bonds should

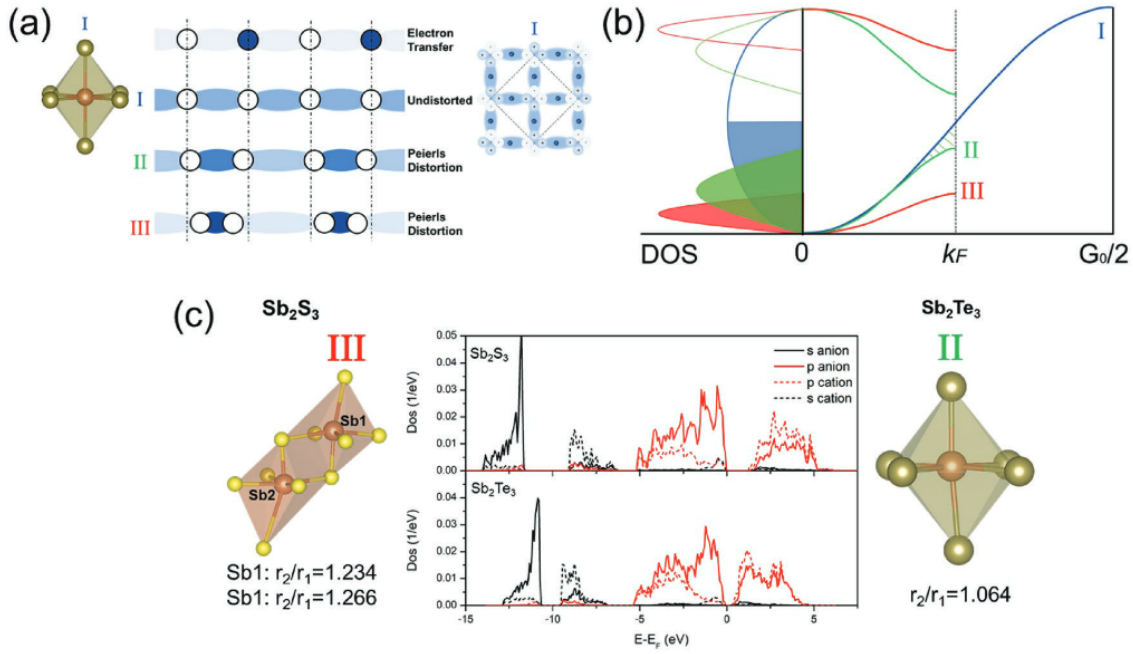

Figure 4.14: a) Octahedral atomic arrangement as observed to first approximation in GeTe and Sb_2Te_3. This arrangement is a consequence of the σ-bonds formed between adjacent atoms due to the half-filling of the p-band. Such a configuration is unstable, as shown for the schematic of an undistorted 1D atomic chain. Two options exist to lower the energy: electron transfer and atomic distortions (Peierls distortion). b) Both charge transfer and the Peierls distortion lead to an opening of a gap and hence a decrease in potential energy for the occupied states. c) This view is supported by the calculated density of states for Sb_2S_3 and Sb_2Te_3. The degree of Peierls distortion is described by the averaged radii of three short (r_1) and three long (r_2) bonds, that is, r_2/r_1. Note that for Sb_2S_3, there are two different cation positions acting as the center for two different octahedral motifs. These two octahedral motifs have therefore different level of distortion, as indicated by the different values of r_2/r_1. For both materials, the valence band is dominated by p-electrons, even though the octahedral motif is more distorted in Sb_2S_3. [128]

give rise to an ideal octahedral structure and metal-like properties with no band gap. However this electronic configuration is energetically unstable." The authors note that the energetic instability is usually resolved by a structural distortion (called Peierls distortions in the solid state and Jahn-Teller distortions in molecules) and in other chalcogenide compounds these distortions result in three long and three short bonds with an eventual transition to covalent bonding in the short bonds. The effect of the distortion on the electronic structure is illustrated via the DOS and is shown in figure 4.14. In figure 4.14(a), the structure labelled I is unstable and does not exist in nature for the Sb chalcogenides. We do not see this kind of

bond length distortion in the bulk PbX family. The stable atomic configuration is a cubic structure and exhibits the octahedral coordination of structure I. However the bulk PbX family are all semiconductors with a narrow band gap.

At this point it is interesting to note that the minimum band gap in the electronic band structure occurs at the L point for bulk PbX. Consider that lines in the BZ correspond to planes in the real crystal, as illustrated for selected planes shown in figures 4.12 and 4.13. The L point occurs along the [111] direction in k-space, which corresponds to [111] planes composed of one type of atom (see figure 4.12 and 4.13). There are two more larger band gaps in the PbS bulk band structure along $\Gamma - K(\Sigma)$ and $\Gamma - X(\Delta)$. The line between $\Gamma - K$ possesses high symmetry, denoted Σ, and corresponds to the [110] planes in real space. The line between Γ – X also possesses high symmetry, is denoted Δ, and corresponds to the [100] planes in real space. While in the bulk crystal the coordination number of every atom is the same, the number of in-plane bonds is different for these three families of planes. The [100] plane has 4 in-plane bonds, the [110] plane has 2 in-plane bonds, and the [111] plane has 0 in-plane bonds. This trend in bonds correlates to the change in band gap. Considering the orbital analysis outlined above, this trend in energy separation between VBM and CBM suggests that there is a significant amount of delocalized charge in bulk PbS which is not contained in the bonds. These delocalized states are high-energy states in the valence band, but the lowest energy states in the conduction band.

Another observation worth notice is that within the PbX family, the gap between the CBM and VBM at Δ narrows between PbS to PbSe to PbTe (figure 4.5). This gap is related to the [100] plane (figure 4.12) which contains the most bonds. The change in gap size across the PbX family correlates with the decreasing electronegativity (see figure 4.11) down the periodic table column from S to Se to Te where the frontier orbital energy is increasing causing larger p orbitals and more electron orbital interactions. The narrowing of the band energies agrees with the correlation to less localized electrons. For the band gap to become narrower the

electrons need to be in a metallic-like state where they are neither held tightly close to atoms (electron transfer or ionic bonding) or localized to a small region of space between atoms (electron sharing or covalent bonding). The band gap in the bulk PbX does not completely close however, indicating a small amount of localization in agreement with the metavalent bonding picture. In metavalent bonded systems, the ratio of long bonds to short bonds is an indication of the amount of electron sharing (figure 4.14 caption). The distance between bonded atoms is 3.0A in bulk PbS, and the distance between the unbonded atoms in the [110] and [111] planes is 4.24A.

4.7 Study Results

Toy Models

To understand how atomic coordination, local distortions, and non-stoichiometry effect the electronic environment we will study 3 toy models. Figure 4.15 A) and B) shows the unit cells and extended structure for the two 2D periodic slabs each consisting of 5 layers and with fixed bond length throughout. We will later explore the effect of letting the structure relax.

The slab in figure 4.15 A) is oriented with [001] planes in the (001) direction and is truncated along the z axis exposing [001] surfaces on the top and bottom of the slab. This geometry is referred to as the [001] slab in this study, after the exposed surfaces. Because of this spatial arrangement this slab has equal numbers of Pb and S atoms. Of the toy models studied here this slab is the simplest; it introduces the least complexity and is the closest configuration to the bulk. As discussed above, [001] terminated surfaces have been shown to be energetically stable and have been found on large nano-structures [115] [116]. This toy model was chosen for this study because it is relevant to experimental geometries, retains a majority of 6-fold coordinated atoms similar to the bulk, and only introduces two degrees of complexity: 5-coordinated atoms and broken symmetry at the surface.

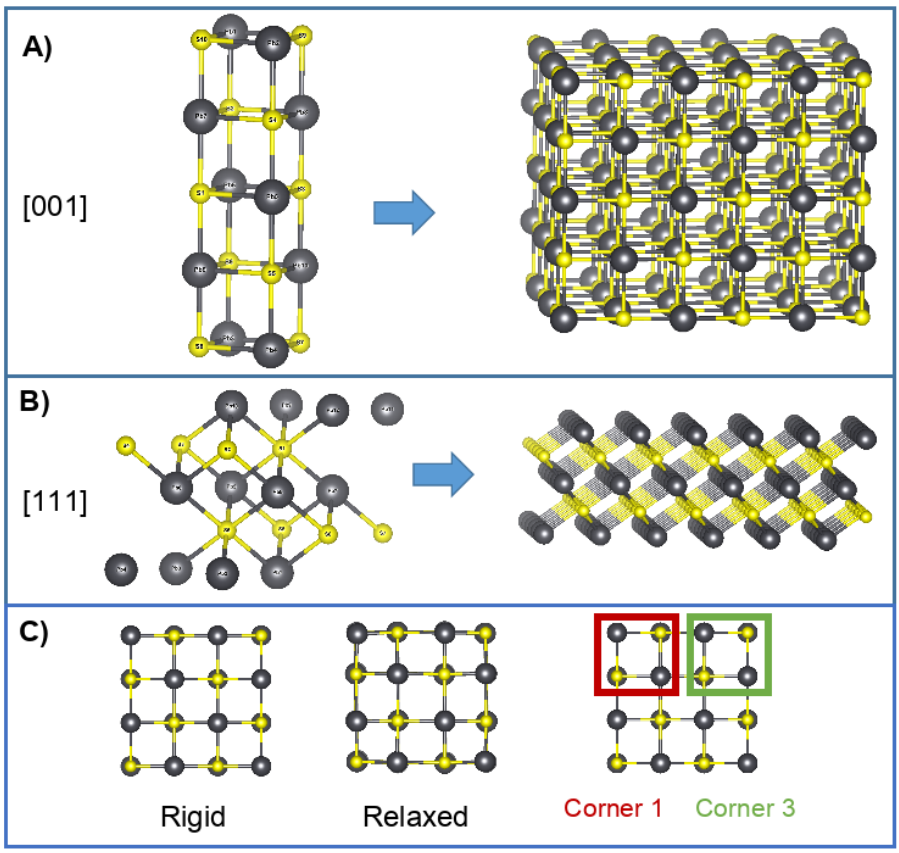

Figure 4.15: PbS toy models used in the calculations in this study. Panel A) shows the unit cell (left) and the crystal (right) of the [001] surface terminated 2D slab. Panel B) shows the unit cell (left) and the crystal (right) of the [111] surface terminated 2D slab. Panel C) shows the 64 atoms cube in the rigid configuration (left) the relaxed configuration (middle). The leftmost cube highlights in a red box corner 1 with a 3-coordinated Pb atom and in a green box corner 3 with a 3-coordinated S atom.

The slab in figure 4.15 B) is oriented with [111] planes along the (001) direction and is truncated along the z axis exposing [111] Pb-rich surfaces. This geometry is referred to as the [111] slab in this study, in reference to the exposed surfaces. This slab has a Pb to S ratio of 3:2 or 1.5 and has alternating layers of Pb and S atoms. These surfaces have been shown to be metastable and occur only in small nano-structures (<10nm diameter). In this slab there are 3-coordinated Pb atoms on the surface, attached to internal layers of 6-coordinated S and Pb atoms. This [111] slab toy model was chosen in order to study the effects of Pb-rich surfaces and low coordinated Pb atoms in an extended geometry.

Figure 4.15 C) shows the two configurations of the 64 atom cube toy models which

have equal numbers of Pb and S atoms. One of the cubes was kept at fixed bond length in order for ready comparison with the slab geometries as well as the bulk PbS. The other was allowed to geometrically relax until the total energy was less than 0.5 eV/A to investigate the effects of Peierls distortions within PbS nanostructures. Within both cubes special attention is paid to the corners. Plotting data specifically related to these corners allows us to distinguish the contributions from reduced coordination and varying bond lengths on the electronic properties.

In the bottom right of figure 4.15 panel C) two corners are highlighted in red (corner 1) and green (corner 3) squares. These 'corners' consist of 8 atoms in a cube configuration and differ in which species of atom are of which coordination. For example in corner 1, the 3-coordinated atom is Pb, with S 4-coordinated atoms, Pb 5-coordinated atoms, and an S 6-coordinated atom. The situation is reversed in corner 3 with an S atom in the 3-coordination position, Pb atoms in the 4-coordination positions, S atoms in the 5-coordinated positions, and a Pb atom in the 6-coordination position.

This specific arrangement of 64 atoms in a cube was chosen after the work by Kiran et. al. [129]. They not only found this structure to be energetically stable, but determined it is the smallest 'building block' of bulk PbS and therefore dubbed it a baby crystal. The 64 atom geometry is large enough to reflect bonding behavior in PbS nanocrystals but small enough to be studied using DFT computational methods.

For each of these toy models the electron localization function (ELF), density of states (DOS), and projected density of states (PDOS) have been calculated. The Octopus code outputs PDOS data for the s and p valence orbitals, in total and separated into contributions from each atom. Additionally, within the p valence orbitals p_x, p_y, and p_z orbitals are resolved and can be plotted separately.

4.8 2D Slabs

4.8.1 [001] Slab

Beginning with the [001] slab we can see the effects of introducing a surface and therefore breaking the 3D symmetry of the bulk environment as well as look at the effects of one missing bond in Pb and S atoms on the surface. In figure 4.16 the electron charge density and ELF are shown along the same [100] plane 2D cut. Due to the orientation and symmetry of this slab this is the only 2D cut shown for this geometry as it captures all of the relevant features. The three yellow ovals highlight Pb atoms.

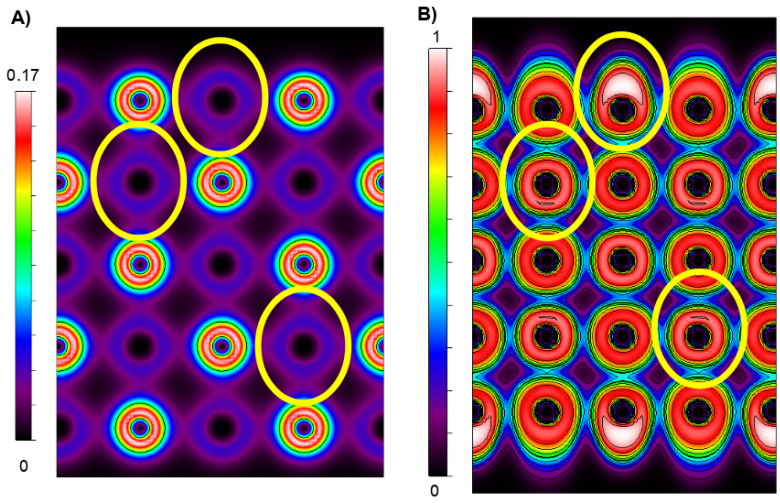

Figure 4.16: 2D slices of data taken along a [100] plane within the PbS [001] slab. A) electron charge density and B) ELF. The center atom is Pb. Yellow ovals highlight the same Pb atom in both plots.

As mentioned in section 2.4 the ELF data must be correlated to charge density data to understand how much charge is associated with the ELF values for a region of space. This is because the ELF data does not indicate how much charge is in a region, only the relative amount of kinetic energy the charge has. Upon inspecting figure 4.16 it can be seen that while the Pb atoms are surrounded by regions of high ELF, these regions contain low charge density. The highest ELF regions are found on the surface Pb atoms where the periodic symmetry in the z direction is broken. The ELF extends out from the surface but is still localized around each

atom. The white regions around the surface Pb atoms may appear to be lone pair electrons at first glance, but when comparing to the charge density plot there is no concentration of charge in this region. Instead these high ELF regions indicate a large Coulomb repulsion of the charge localized around the Pb atom away from the adjacent S atoms, and therefore large kinetic energy for the charge. The charge density concentrated around S atoms is significantly larger than the charge density around the Pb atoms, however the charge around both atoms is localized in an s orbital-like configuration. It should also be noted that there is no difference in the amount of charge in the surface atoms versus the interior atoms. There is however a difference in the ELF values. All of the interior atoms are six-fold coordinated while the atoms on the surface are five-fold coordinated.

In figure 4.16 B) a clear directionality of the ELF between bonded atoms appears. Some variation can be seen between surface atoms and the second layer, perpendicular to the surface, with higher ELF values in bonds between 6-coordinated interior atoms and 5-coordinated surface Pb atoms. The ELF between 5-coordinated Pb and S surface atoms, parallel to the surface, is consistent with the behavior inside the slab between 6-coordinated atoms.

To investigate the bonding regions further 1D line plots showing the profile of the ELF along particular directions were taken, as shown in figure 4.17 panel A). In figure 4.17 B) profile 1 and profile 2 show little difference between Pb and S surface atoms in the bonds perpendicular to the surface. Likewise within the structure the ELF values in the bonding regions (between atoms) are very similar. This is confirmed in 4.17 C) which shows line plot 3 and 5 concurrently; the data plotted together are for bonds parallel to the surface and between surface atoms and and interior atoms, respectively.

The uniformity of ELF in the bonding region may be largely due to the fact that the bond lengths are kept constant in this geometry. However observations about the nature of the bonding can be made. These observations can be assumed to apply also to bulk PbS since the bond length is the same and the coordination of

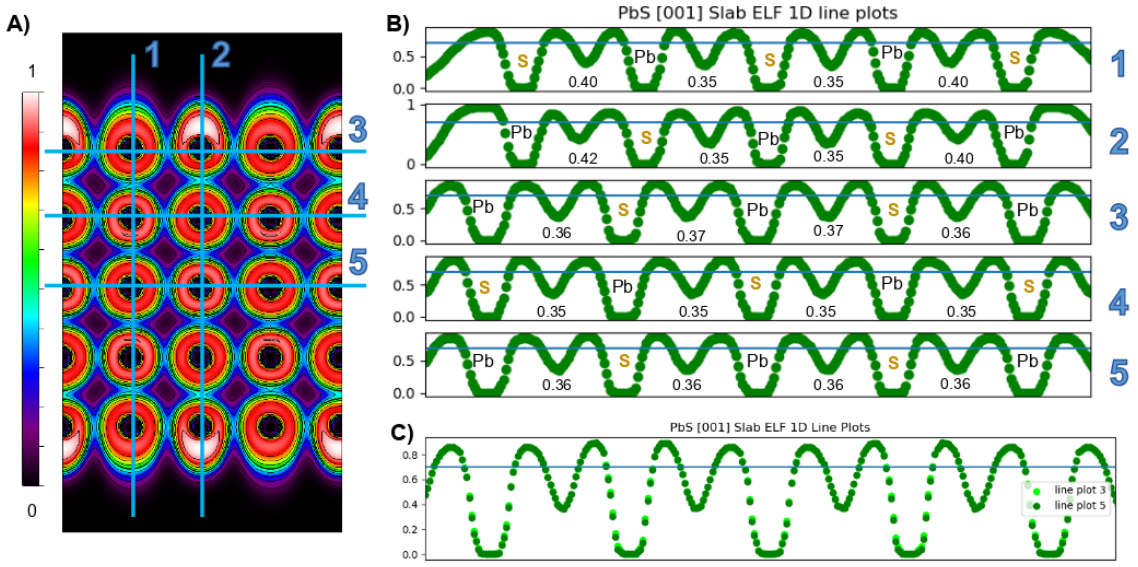

Figure 4.17: A) PbS [001] slab 2D ELF plot taken along a [100] plane with lines showing where the line plots in B) were taken. B) 1D ELF line profile plots corresponding to rows of atoms in panel A). Atom labels on the plots indicate the location of the nucleus of the atom. Numbers on the plots indicate the minimum value of the ELF in the region of the plot in which the number appears. C) plot 3 and 5 from panel B) plotted together.

the interior atoms is the same.

With certainty it can be said that the bonds in this geometry are not covalent, as between the atoms there is a lack of attractor or any strong ELF signature. Nor are the bonds ionic, as there is a low but significant value of ELF in the region between atoms. An argument could be made for dipole like bonding due to the 'v' shape of the profile between atoms, however the minimum value of the ELF in these regions is much higher than a typical dipole bond and is about the same as a hydrogen bond. Also dipole bonds are characterized by an unshared electron bond, and in the [001] plane shown here PbS is known to share electrons between the atoms. This leaves metavalent bonding, with a mixture of localized and shared electrons between atoms.

4.8.2 [111] Slab

The orientation and geometry of the [111] slab makes it less straightforward to analyze. A single 2D slice is not sufficient to capture all of the interactions between

atoms. Therefore four 2D cuts are taken along three planes: one along the [100] plane (figure 4.18), one along the [110] plane (figure 4.20), and two along the [111] plane (figure 4.21).

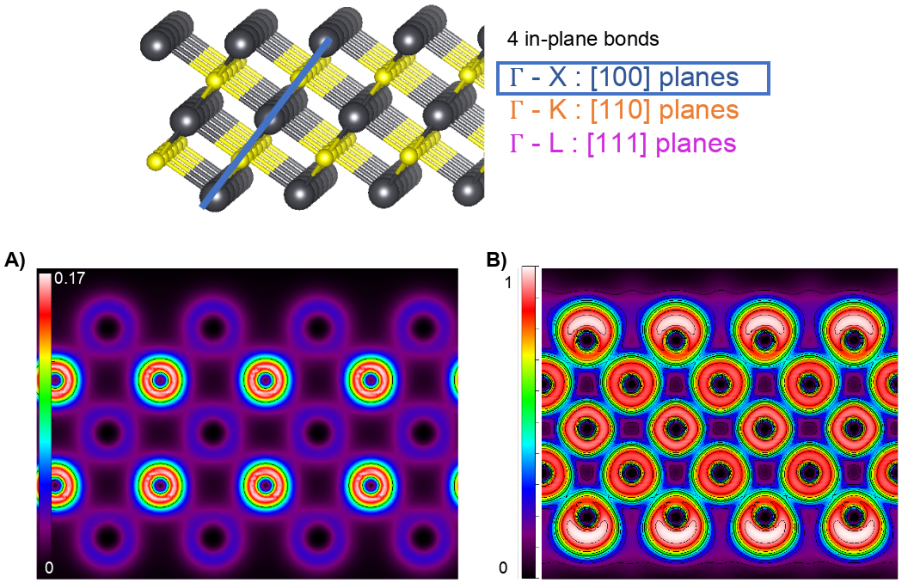

Figure 4.18: PbS [111] slab 2D cut along the [100] plane A) charge density plot and B) ELF plot. At the top of the figure a blue line shows the [100] plane from which the 2D slice was taken and identifies the corresponding BZ direction. This plane contains four in-plane bonds between Pb and S atoms.

In the [111] terminated surface, due to the geometry of the crystal structure, the first layer of atoms are all of the same type and are all 3-coordinated. Those 3-coordinated surface atoms are bonded to 6-coordinated atoms of the other type which make up the second layer. From experimental and theoretical studies it is known that PbS nano-structures are Pb rich, with Pb-terminated [111] facets [115] [116].

Figure 4.18 A) shows the charge density maintains the behavior observed in the [001] slab in that charge is localized around S and Pb atoms with significantly more charge around the S atoms. There is little difference in magnitude of charge density between the surface Pb atoms and the interior Pb atoms and the shape of the charge density around the atoms reflects the number of bonds. Figure 4.18 panel B) shows the ELF for the same plane as panel A). Similar to the [001] slab, the ELF in the [111] slab is localized around each atom with clear directionality between bonded

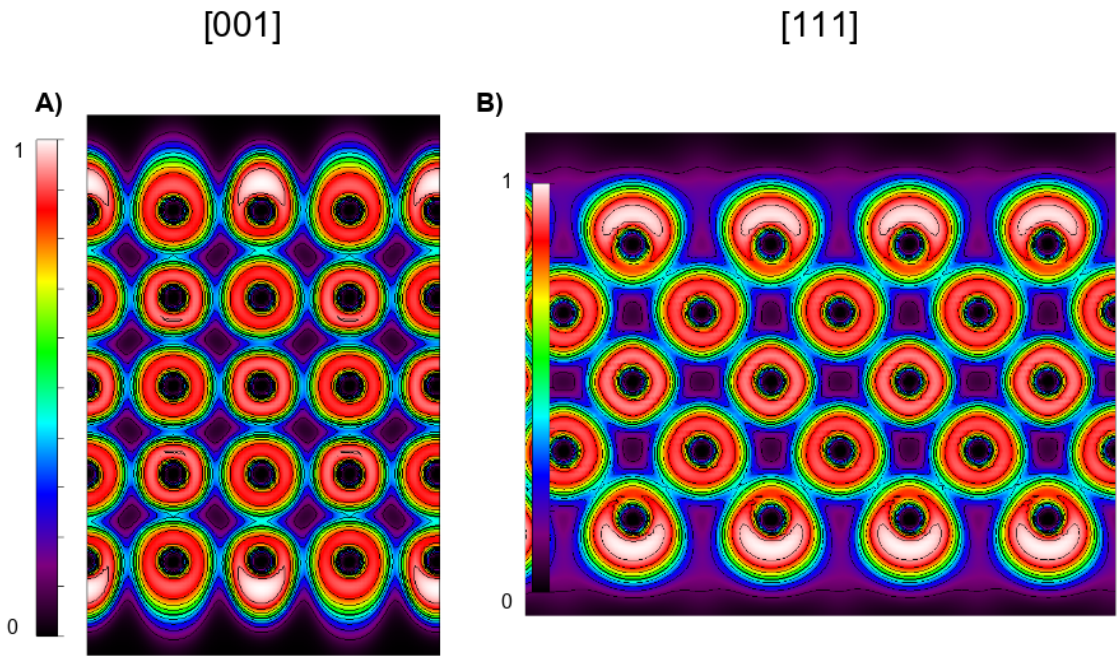

Figure 4.19: PbS [001] slab [100] plane 2D ELF and [111] slab [100] plane 2D ELF side by side for comparison.

atoms. Surface Pb atoms have regions of high ELF which are localized around the Pb atoms but extends away from the interior of the slab. These regions, shown in white in the ELF plot, are not lone pairs but regions of large kinetic energy. The surface atoms are 3-coordinated and not bonded to each other, however the region between these atoms has a non-zero ELF. This increased ELF between the surface atoms can be seen in all the ELF plots of the [111] slab and will be discussed further below.

Figure 4.19 shows ELF plots from both [001] and [111] slabs taken along the same [001] plane. The ELF of these two slabs is generally very similar, the bonding regions between the surface atoms and second layer show ELF regions that are green versus the interior atoms showing a cyan color. The biggest difference is the behavior at the surface indicating that the lower coordination Pb atoms may effect the bonding properties at the surface.

In figure 4.20 the charge density and ELF for the [110] plane within the [111] slab are presented. In both plots the bond direction is easily identified, with zero charge density in the regions between atoms where no bond is present. In the ELF

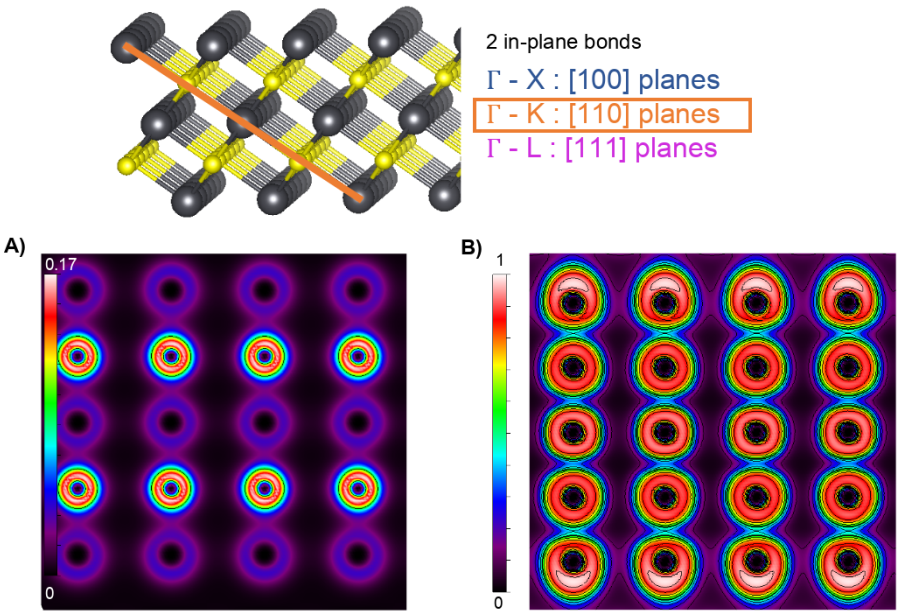

Figure 4.20: PbS [111] slab 2D cut along the [110] plane A) charge density plot and B) ELF plot. At the top of the figure an orange line shows the [110] plane from which the 2D slice was taken and identifies the corresponding BZ direction. This plane contains two in-plane bonds between Pb and S atoms.

plot shown in figure 4.20 B) the same white regions of high ELF can be seen around the Pb atoms on the surface, as well as purple regions between surface Pb atoms where no bonds are present.

This surface behavior is investigated more clearly in figure 4.21 where 2D slices have been taken along the [111] planes at both the surface and the interior, as shown at the top of the figure. While the charge density plots in figure 4.21 C) show no significant difference in charge present, the ELF plots in figure 4.21 A) and B) show distinct differences. Note that in this [111] plane there are no bonds (see figure 4.13) and that all slices are taken through the center of the atoms in the center of the bonding region. The ELF plot for the surface atoms shows that the white areas of high ELF not only extend away perpendicular from the surface but have a preferred orientation parallel to the surface. There is an extended region of constant ELF between the atoms however it is localized and too low in value to indicate a metallic state. In figure 4.21 B) a similar extended region of constant ELF occurs with maxima and minima forming a triangular pattern between the atoms. These ELF plots do not show characteristics of any particular bond, but they do show that

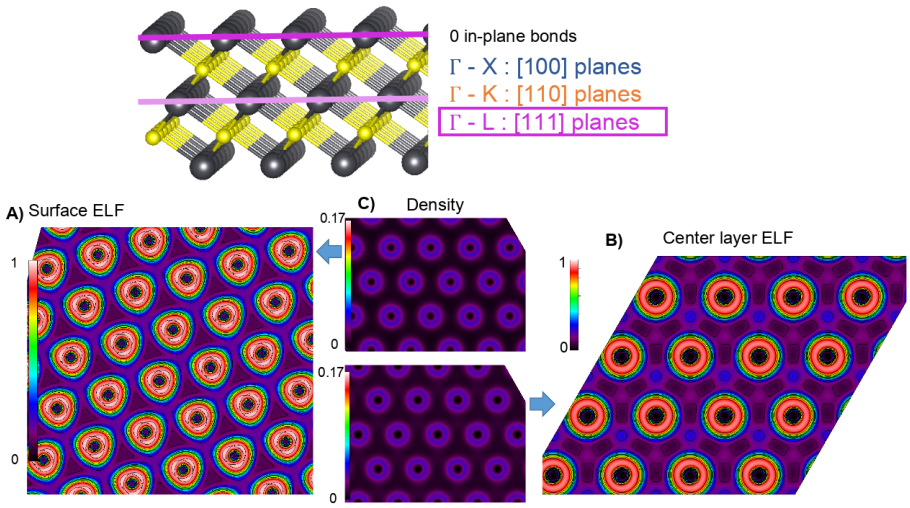

Figure 4.21: PbS [111] slab 2D cut along the [111] plane. Two slices were taken for this plane to show the contrast between the surface atoms and the interior atoms. At the top of the figure a magenta line shows the surface [111] plane from which the 2D slice shown in A) was taken and and the pink line shows the interior [111] plane from which the 2D slice shown in B) was taken. In panel C) the upper plot shows the charge density in the same plane as A). The lower plot in panel C) shows the charge density for the same plane as B). The magenta box in the upper right identifies the corresponding BZ direction for both of these planes. This plane contains zero in-plane bonds between Pb and S atoms.

electrons are less tightly localized around any particular atom in the [111] plane than in the [100] or [110] planes

Line profiles of the [110] plane ELF plot are shown in figure 4.22. Line profile 1 shows the ELF along the Pb-S bond, which is the same as for bonds in the [100] plane. Line profile 2 shows the ELF between surface atoms, which is the same as a line profile taken between atoms in the [111] surface plane. Line profiles 3 and 4 also show the ELF between non-bonding S and Pb atoms, respectively, and give the same values as would be obtained by taking a line profile in the [111] plane. Considering line profile 1 first, we again see a slightly higher ELF value in the bonds that include surface atoms. It is also clear from this plot that at the surface the ELF is concentrated in a direction perpendicular to the slab and away from the interior, as seen by the taller and wider peak on the far right and far left of line profile 1. Line profile 2 shows the ELF in the region between non-bonding surface Pb atoms with a small but significant minimum value of 0.11. The surface is directly compared to non-bonding regions between both S and Pb interior atoms in panel C) where the

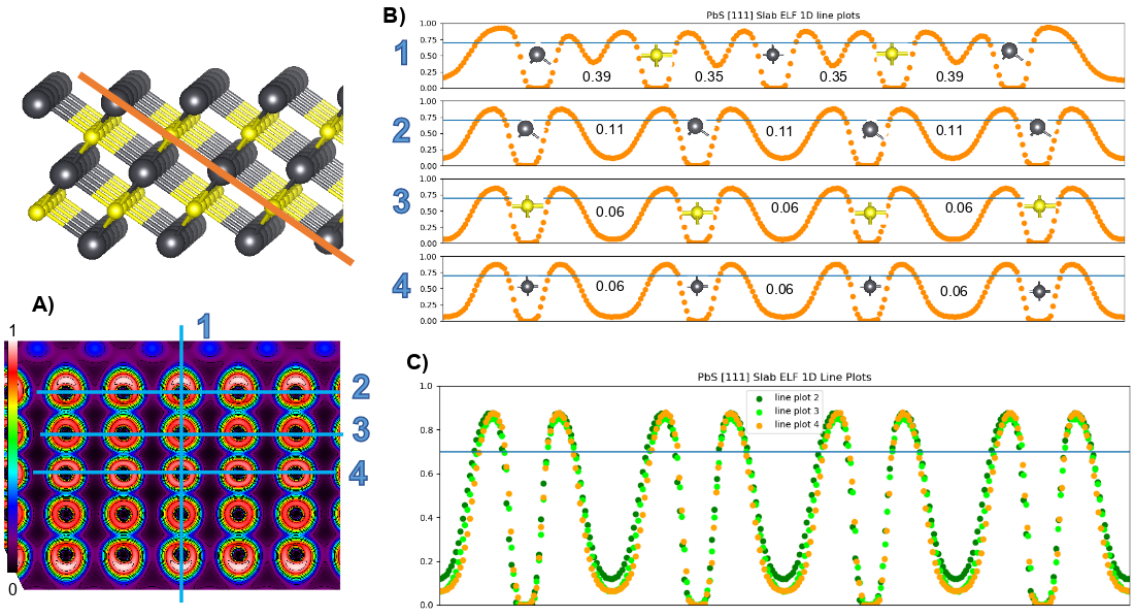

Figure 4.22: PbS [111] slab ELF 1D line profile plots along the [110] plane. Atom on the plots indicate the location of the nucleus of the atom. Orange line in the upper left shows the plane from which A) the ELF 2D plot was taken. B) shows the line profiles for each line indicated in A). Black atoms are Pb and yellow atoms are S. The numbers indicate the value of the ELF at the minimum between the atoms where they appear. C) shows line profiles 2, 3, and 4 plotted together.

behavior found at the surface is clearly only a feature of the surface.

In figure 4.23 the DOS for both the [001] slab and the [111] slab are plotted together in panel A), with the PDOS for S-s, S-p, Pb-s, and Pb-p orbitals separated by the contribution from atoms within each layer in panels B)-D). This allows for the comparison between the influence of 3-coordinated and 6-coordinated Pb atoms as well as the influence of stoichiometric and Pb-rich geometries.

The most apparent difference between the total DOS in figure 4.23 A) is that the [001] slab is of semiconducting character and the [111] slab is metallic. At the Fermi level there is a depletion of [001] slab valence band states and an enhancement of [111] valence band states. In figure 4.23 B) the PDOS contributions from the surface layer atoms from both slabs are plotted. For the [111] slab data (dashed lines) the greatest contribution to the Fermi level states from any of the atoms comes from the surface Pb-p orbitals. The contribution at the Fermi level correlates with the high ELF values around these atoms, indicating that the electrons localized around the surface have a high kinetic energy.

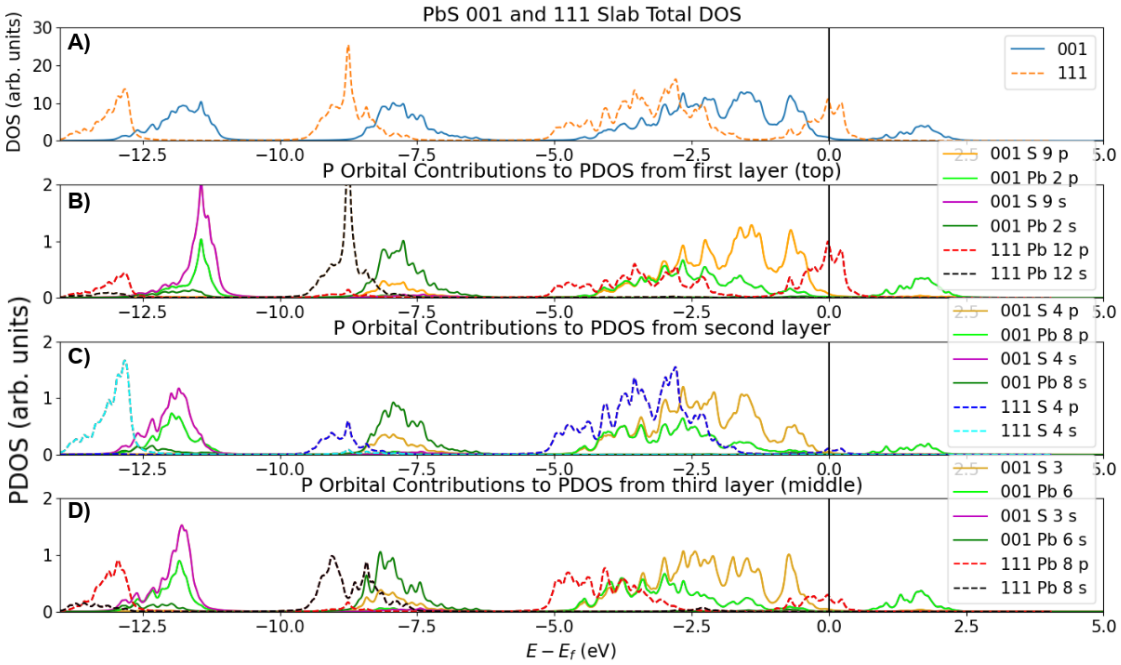

Figure 4.23: PbS [001] and [111] 2D slabs DOS and PDOS plots. Both slabs are plotted together with dotted lines indicating data from the [111] slab. Colors correspond to contributions from individual atoms s and p orbitals, as indicated in the legend. A) total DOS for both [001] and [111] slabs. B) PDOS from atoms comprising the first layer of the slabs. C) PDOS from atoms comprising the second layer of the slabs. D) PDOS from atoms comprising the third layer, also the middle layer, of the slabs. Due to symmetry only data from the first three layers needs to be considered.

The influence of the S-p states is crucial to the optical properties of nanostructured PbS. As can be seen in the [111] DOS, the Pb layers have metallic character with no gap between the occupied and unoccupied states. It is only in the [001] layers, with the addition of S atoms in plane, that a gap above the Fermi level opens. The forming of p-p-sigma bonds between the S-p states and the Pb-p states lowers the overall energy, creating bonding and antibonding states and opening the gap at the Fermi level. It should also be noted that in the pure S [111] layers there is not a significant number of states at the Fermi level for significant optical activity. These layers are [111] layers in plane, but out of plane are connected in the [110] and [001] planes. Pb orbitals are higher in energy than S orbitals, and so once Pb electrons are bonded the bond is of lower energy than the original orbital. This provides the higher energy unoccupied states but there is no gap without the bonding between Pb-p states and S-p states creating bonding and anti-bonding states.

Overall there is a significant difference between the [001] slab and [111] slab. In considering first the [001] slab, The ELF data in figure 4.17 C) shows no difference in the bonding region parallel to the surface in the first two layers (between the 5-coordinated surface atoms and the 6-coordinated interior atoms). In the direction perpendicular to the surface (figure 4.17 B) 1 and 2)), there is increased ELF surrounding the surface atoms indicating a higher kinetic energy of the electrons at the surface. The higher energy is reflected in the DOS in figure 4.23 B) and C) where there are more higher-energy states in the surface layer atoms than the interior atoms.

The situation in the [111] slab is different due to the all-Pb 3-coordinated atoms on the surface layer of the slab. Figure 4.22 C) indicates there is a difference in the inter-atom regions (parallel to the surface) in the surface atoms versus the interior atoms. Whether the layers are of Pb atoms or S atoms, 6-coordinated single layers show the same behavior. On the other hand, 3-coordinated Pb atoms behave differently than 6-coordinated Pb atoms. The result is an overall metallic character of the slab and an extended region of significant ELF between atoms in regions where there is not bonding. It is interesting to note that there is not a significant difference in the ELF in the bonding regions when comparing surface bonds and interior bonds as there is in the [001] slab. This suggests that the non-bonding regions are more important for electronic behavior in the [111] slab which correlates with the metallic behavior seen in all DOS and PDOS plots (figure 4.23).

4.9 Cubes

4.9.1 Rigid Cube

In examining the cubes several 2D slices were selected for plotting the ELF. Figure 4.24 shows a side view of the rigid 64 atom PbS cube with two planes highlighted: [001] and [010]. The symmetry of the cube, especially when all of the bond lengths are held equal as in the rigid cube, means that the [100], [010], and [001] planes

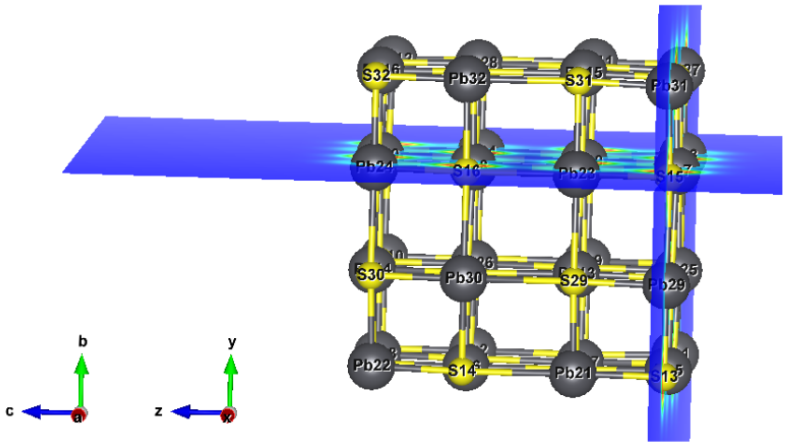

Figure 4.24: PbS rigid 64 atom cube. The blue planes show the surface and interior [100] planes that appear in figure 4.25.

are equivalent, and for clarity they will be called [100] planes here. However, the planes in figure 4.24 encompass atoms of varying coordination. Also examined for the cubes are the [110] plane (figure 4.26) and two [111] planes: one comprised of S atoms (figure 4.28) and one comprised of Pb atoms (figure 4.27).

In figure 4.25 the charge density and ELF 2D slices are shown next to the 3D plot where the slice on the left of each panel is indicated by a blue plane on the right of each panel. The top two panels, A) and C) contain atoms only on the surface of the cube, while panels B) and D) contain surface and interior atoms. The white dashed boxes in panels C) and D) indicate the cross-section between the two slices; the atoms inside the box are the same.

In figure 4.25 A) and B) we note that the charge density is extremely similar for all atoms of each type, regardless of if they are on the surface, edge, corner, or interior of the cube. For this reason charge density plots will not be shown for the other planes, the [110] and [111] planes. The behavior of the charge density is the same as in the slabs, where charge density is localized around the atoms with a clear directionality in bonding directions. There is significantly more charge density around S atoms than Pb atoms.

In figure 4.25, C) and D) also appear to be very similar to each other in addition to having similar features as the slab ELF plots: The ELF is localized around each atom with a clear directionality between atoms indicating a lack of metallic bonding,

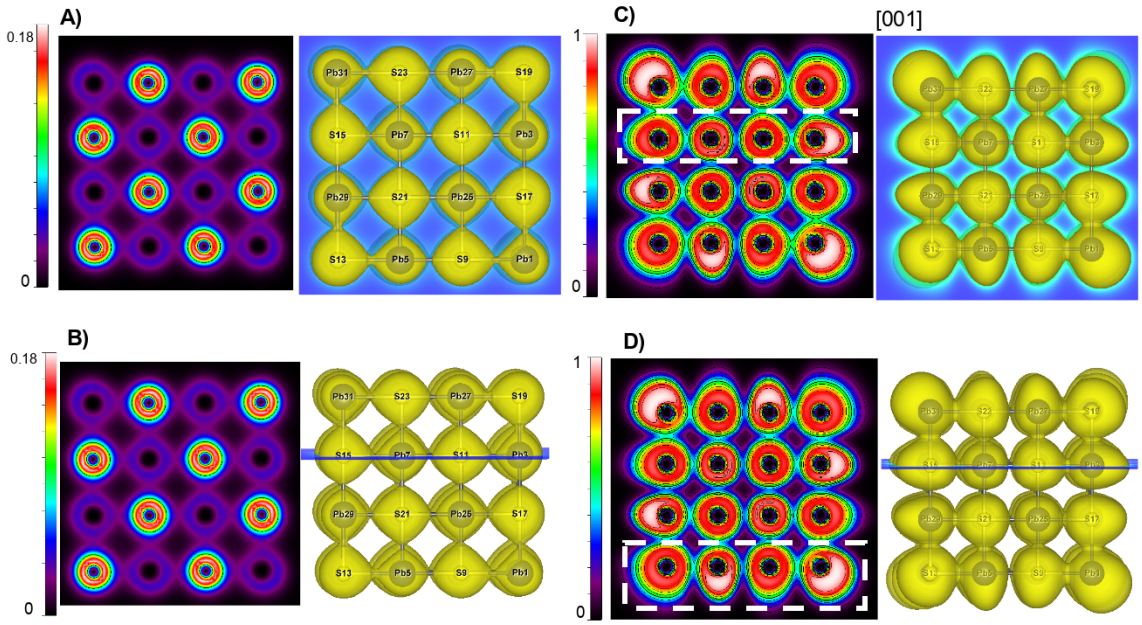

Figure 4.25: PbS rigid 64 atom cube, top left corner atom is Pb. A) surface and B) interior 2D charge density plots for two [100] planes. C) surface and D) interior 2D ELF plots for the same two [100] planes as A) and B) respectively. The white dashed box encloses the same atoms in both C) and D) and is intended purely as an aid to the eye.

there is non-zero ELF in the region between atoms indicating a lack of ionic bonding, there is no bond attractor indicative of covalent bonding, and Pb atoms show regions of white extending perpendicularly away from the interior. Unique from the slab behavior however is what appear to be clusters of atoms more strongly connected to each other. This is most apparent in the 3D ELF plots on the right of each panel. There is a vertical and horizontal disconnect across the center of the cube. The ELF disconnect is not purely a surface phenomenon as the interior 6-coordinated atoms in figure 4.25 D) also show a decrease in the ELF between atoms in the center-vertical and center-horizontal region. This observation of clustering has led to further study of where the concentration of ELF occurs: the 'corners' of this 64 atom cube. By corner it is meant the 3-coordinated corner atom and the seven nearest atoms comprising of the connected cube surrounding the 3-coordinated atom. As this 64 atom cube is highly symmetric it is not necessary to evaluate all eight corners of the cube. Instead two have been selected, as shown in figure 4.15 C). These corners and the space between them are evaluated further in section 4.9.3

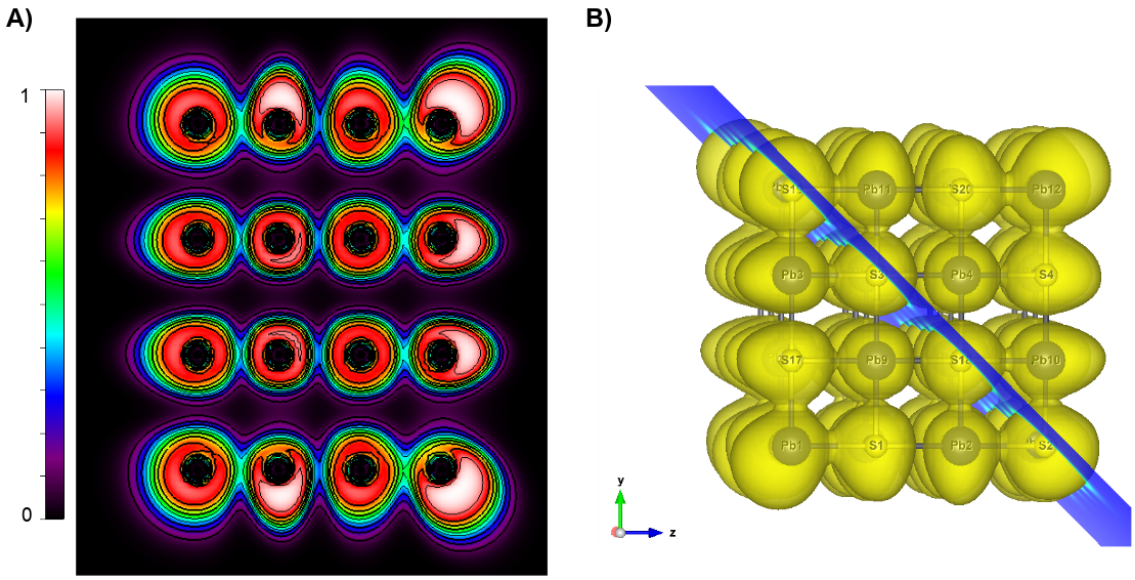

Figure 4.26: PbS rigid 64 atom cube, top left atom is S. A) 2D ELF plot of the [110] plane shown in B).

below.

Signatures of this clustering are evident also in the other planes under study. Figure 4.26 shows the ELF 2D and 3D plots for the [110] direction. In this plane every horizontal row of atoms alternates S-Pb-S-Pb. There is a clear bonding direction horizontally, however regions of purple can be seen vertically between atoms. There is a noticeable difference in ELF in the center bonds (light blue color) where the ELF is lower than the bonds to the left or right of center (green color).

In figure 4.28 and 4.27 the ELF 2D and 3D plots are shown for the [111] direction. In these plots it is noted that there are no bonds in this plane, and the center atom is 6-coordinated while the others are either 5-coordinated or 3-coordinated. There are clear differences between S planes and Pb planes. In figure 4.28 there is a region of continuous ELF which is shared by all of the surface atoms and extends around the perimeter of the plane. In figure 4.27 there is a similar region of extended ELF, however it is on the interior of the cube and contains inner blue regions of higher intensity. The blue regions surrounding the center 6-coordinated atom do not quite connect to other atoms, however between the corner 3-coordinated atoms and the 5-coordinated atoms (which are in the same corner) there is a connection indicating metallic-like behavior. This is similar to the behavior observed in the [111] slab

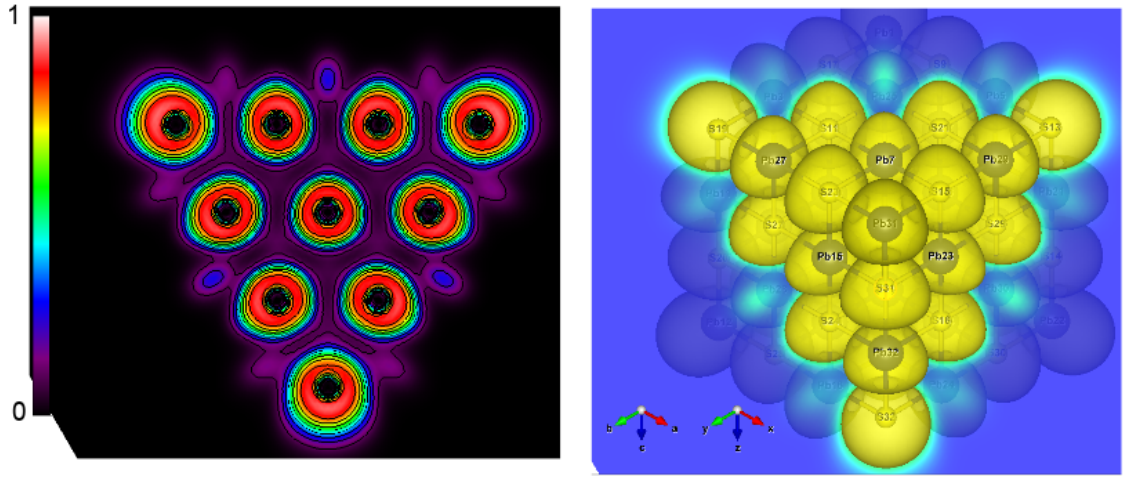

Figure 4.27: PbS rigid 64 atom cube, all atoms are S. Left: 2D ELF plot of the [111] plane shown on the right.

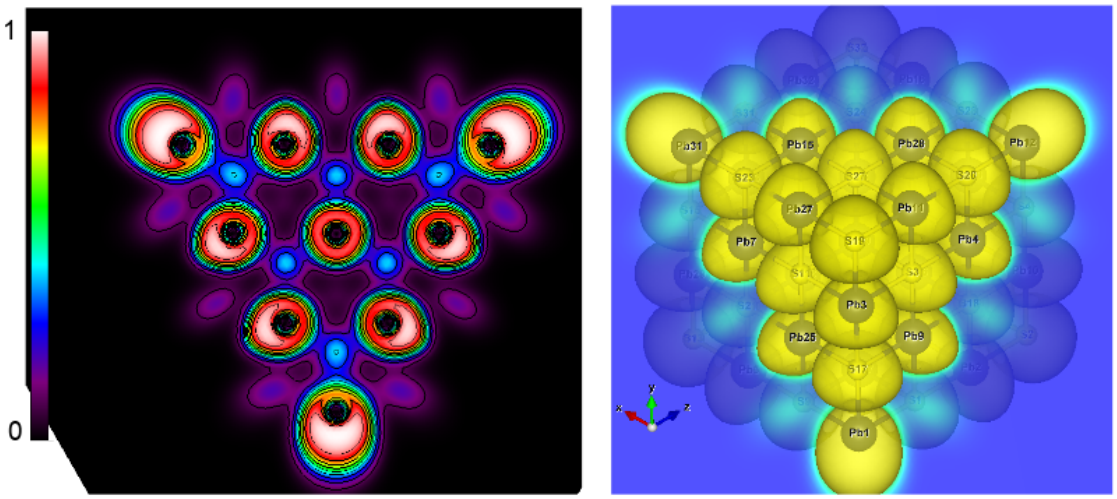

Figure 4.28: PbS rigid 64 atom cube, all atoms are Pb. Left: 2D ELF plot of the [111] plane shown on the right.

surface Pb atoms.

To investigate the behavior of the ELF further, we plotted the 1D profile of the ELF along lines indicated in figure 4.29. The atoms intersected by the line plots belong to two planes, the [110] plane indicated by orange and the [100] plane indicated by blue. Figure 4.30 shows the profiles. It is clear that there is a significantly high value of ELF in the horizontal bonding direction (blue line plots in figure 4.30) that distinguishes it from the non-bonding direction (orange line plots in figure 4.30). This directionality and localization of the charge provide further evidence that the character of the bonding is not metallic.

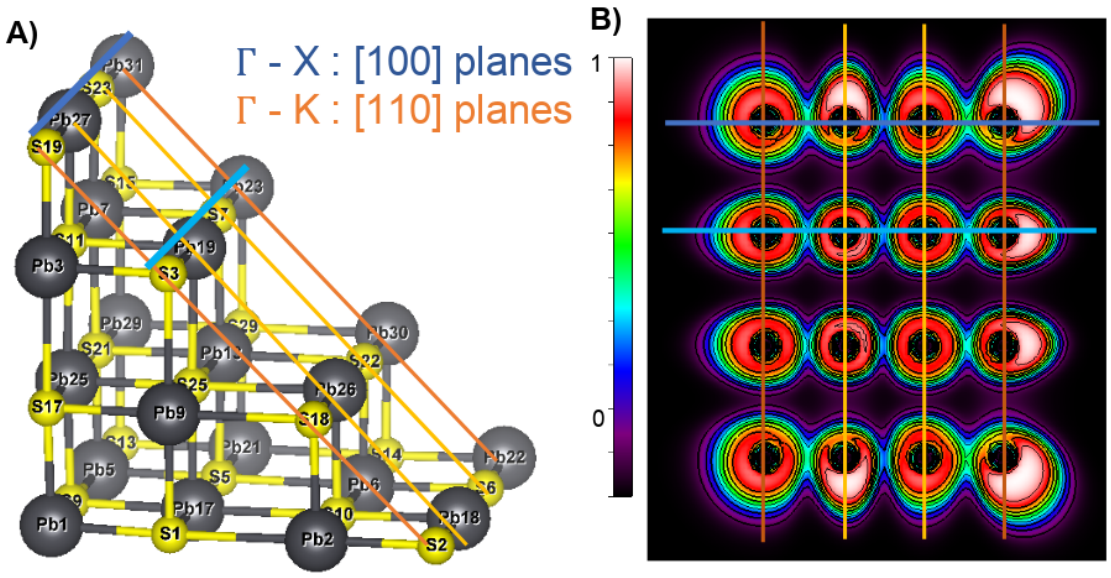

Figure 4.29: A) Truncated PbS rigid cube. Lines show where 1D ELF line profiles were taken. Colors coordinate across this figure and figure 4.30. B) 2D ELF plot through the same [110] plane as indicated by the exposed atoms on the left. Top left atom is S.

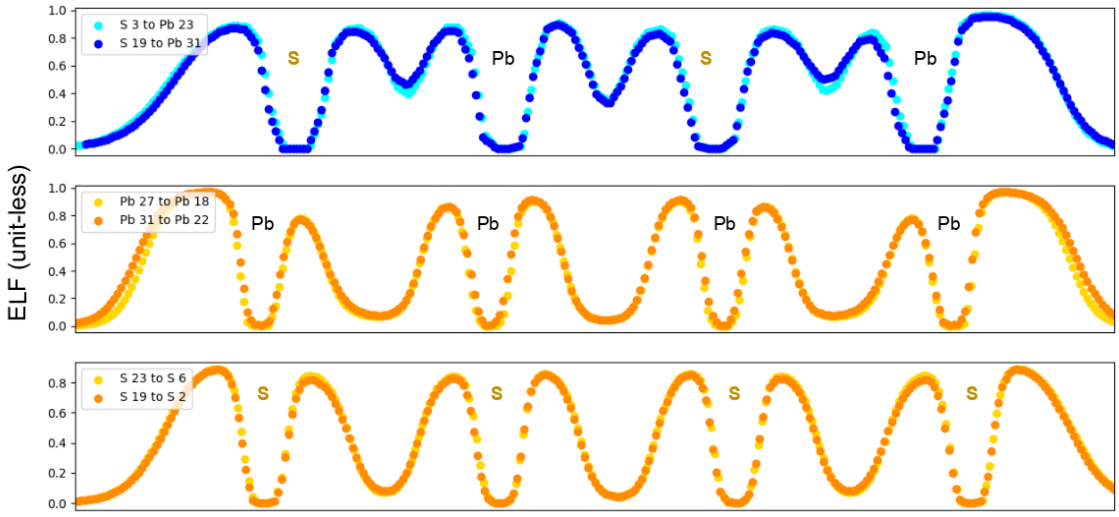

Figure 4.30: PbS rigid 64 atom cube. 1D ELF line profile plots across the atoms indicated in figure 4.29. Atom labels on the plots indicate the location of the nucleus of the atom.

Even though the bond lengths are all the same in this geometry we can still see the effects of coordination on the electronic behavior. In comparing the two [100] line plots, S19-Pb31 and S3-Pb23 (blue line plots figure 4.30), the ELF value in the 3-coordinated atom (S19 and Pb31) bonds is larger than in the 5-coordinated atom (S3 and Pb 23) bonds. However at the center the ELF values are nearly identical. This is a counter-intuitive result since the atoms involved in bonding at this region of space are 4-coordinated (dark blue) and 6-coordinated (light-blue).

Looking at the ELF line profiles in the [110] planes (orange line plots figure 4.30) we observe that the value of the ELF is nearly the same in all regions between atoms, as is expected since this is not a bonding direction. There is a difference however in the shape of the ELF line profile. The shape of the curve around S atoms is almost constant, with a symmetric valley between all S atoms. In the Pb line profiles the valley is slightly skewed towards the 6-coordinated atoms. This is in conjunction with an uneven distribution of ELF on either side of the 5-coordinated Pb atoms at the two ends of the line profiles. The interior atom line plot (Pb27-Pb18) is also slightly narrower than the surface atom line plot. These trends are indicative of the regions of high ELF as identified by white regions in the 2D plot. As has been noted in the slab geometries as well, these regions of high ELF occur around Pb atoms and extend away from the interior of the geometry perpendicular to the surface. The symmetric shape of the valley between the two interior 6-coordinated Pb atoms however, suggests that these two atoms do not share charge.

The total DOS and the PDOS broken out by atom coordination are shown in figure 4.31. Three trends are immediately apparent when comparing the PDOS plots. First, the unoccupied Pb-p states near 2eV change little. Second, the contribution near the Fermi energy from the S-p states decreases as coordination increases. Third, the energy of the lowest band of states becomes lower in energy as coordination increases. The significant Pb-p states in the lowest energy band together with the change in energy support the existence of metavalent bonding in this small system, consistent with the observation that p-p σ bonds are the primary bond in

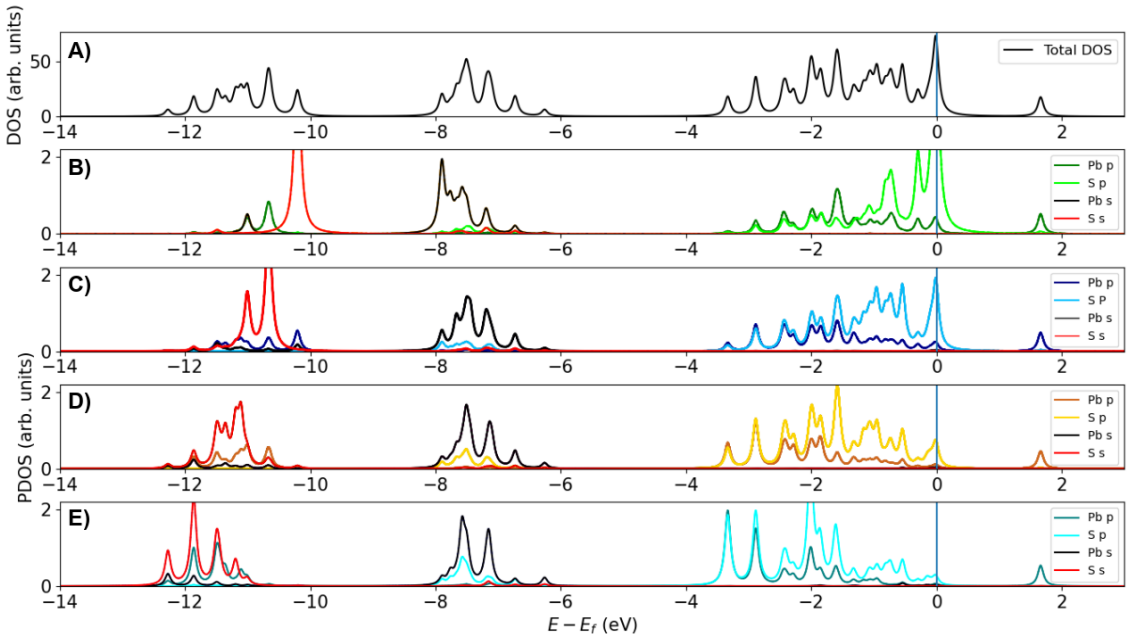

Figure 4.31: PbS rigid 64 atom cube. A) total DOS for the entire cube. B) PDOS of the 3-coordinated atoms within the rigid cube. C) PDOS of the 4-coordinated atoms within the rigid cube. D) PDOS of the 5-coordinated atoms within the rigid cube. E) PDOS of the 6-coordinated atoms within the rigid cube.

the metavalent scheme.

Metavalent bonding is a unique balance between electrons shared and electrons transferred between atoms. Overlaps in Pb and S states indicates bonding states, which also produce anti-bonding states at higher energies. As the unoccupied states near 2eV do not change with atomic coordination, the bonding states may be delocalized over multiple atoms of different coordinations. In low-coordinated atoms there is a peak in states at the Fermi level, with only the 6-coordinated atoms in panel E) of figure 4.31 resembling the behavior of the slabs.

The directional behavior of the ELF of the interior 6-coordinated atoms indicates non-local behaviors of the electronic properties. This has consequences for bulk PbS in that defects and domains within bulk crystalline environment likely have an impact on an extended scale.

4.9.2 Relaxed Cube

The Wuttig group has published several manuscripts investigating metavalent bonding. Particular attention is placed on the relationship between metavalent bonding and structural distortion in several systems: in ref [130] GeS and two phases of GeTe are examined, and in [131] Sb_2S_3 and Sb_2Te_3 among others. In examining GeTe and GeS the authors note "the Peierls distortion effect is to localize the electrons that are delocalized in the symmetric rocksalt structure." [130]. In all of these systems under study it is found that the bonding is from a half-filled band of p-electrons concurrent with very little s-p orbital mixing so that the p-electrons govern bond formation [128]. In order to minimize the overall energy these p-electrons form σ bonds resulting in the 6-fold coordination of each atom. However this electronic configuration is unstable and leads to either a structural distortion (Pierels distortion) or charge transfer between adjacent atoms. Either of these mechanisms reduces the potential energy and causes an increase of the electronic energy gap at the Fermi level. This situation will prove important in this section.

In real PbS QDs the bonds do not remain at 3.0 Å due to Pierels distortions which reduce the overall energy of the structure [132] [133] [128]. Therefore the 64 atom cube geometry was allowed to relax. Figures 4.33 - figure 4.39 presents the same information for the relaxed cube as was presented for the rigid cube in order to enable a direct comparison. Figure 4.32 shows the relaxed cube with some selected atoms labeled. In table 2 the bond lengths of these atoms are given. To follow the analysis of [94], the R_{long}/R_{short} value is calculated. All of the lengths in this relaxed cube fall within the range for metavalent bonding.

In figure 4.33, panels A) and B) show that the change in atomic positions and bond lengths does not alter the charge density much. The clustering around the 3-coordinated atoms at the corners is more apparent but the charge density is still largely localized around the atoms with a clear directionality in the bonding regions. The S atoms still show a much larger intensity of charge density than the Pb atoms. In panels C) and D) the clustering is very prominent with an extended region of

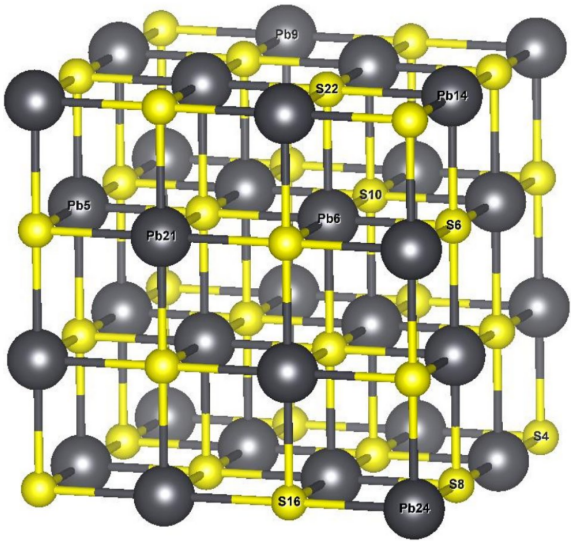

Figure 4.32: PbS relaxed 64 atom cube. Several atoms are labeled which were used to analyze the geometric distortions due to geometry relaxation.

significantly high ELF surrounding each cluster. In addition to the white regions localized around the Pb atoms on the surface, a significant region of white appears on the 5-coordinated and 6-coordinated atoms. The direction of these white regions toward the center of the plane indicate a depletion of charge in the center, in contrast to the extended state within a cluster with relatively high electron localization between the atoms. The behavior of the extended ELF regions is too localized to be classified as metallic bonding but definitely does not exhibit the characteristics of covalent bonding. It does however fit the description of metavalent bonding.

In figure 4.34 - 4.36 the effects of the clustering at the corners is more visible. In figure 4.34 there is no bonding in the vertical direction however we see a region of low ELF vertically between atoms in the same cluster, indicated by purple in figure reffig:relaxed110elf A). There is still no appreciable ELF in the center horizontal region between the top eight atoms and the bottom eight atoms. In figure 4.35 and 4.36 the extended region around the perimeter and interior, respectfully, is gone and instead only encompasses individual clusters at each corner. However in both S and Pb layers there is an extension of the ELF away from the interior of the cube.

Figure 4.37 shows the directions for which the ELF line profile plots in 4.38 were taken. Each of these plots is analogous to figure 4.30 for the rigid cube. In

PbS 64 atoms	Coordination	R_{long} (Å)	R_{short} (Å)	R_{long}/R_{short}
S4	3	2.65	2.65	1
Pb 24	3	2.64	2.64	1
S 8/16	4	3.16	2.64	1.196
		3.16	2.70	1.170
		2.70	2.64	1.022
Pb 9/14	4	3.16	2.65	1.192
		3.16	2.69	1.185
		2.69	2.65	1.015
S 6	5	3.13	2.69	1.163
S 22		3.13	2.77	1.129
		2.77	2.69	1.029
Pb 5/21	5	3.13	2.70	1.159
		3.13	2.76	1.134
		2.76	2.70	1.022
S 10	6	3.10	2.76	1.123
Pb 6	6	3.10	2.77	1.119

Table 2: Data for the atoms labeled in figure 4.32.

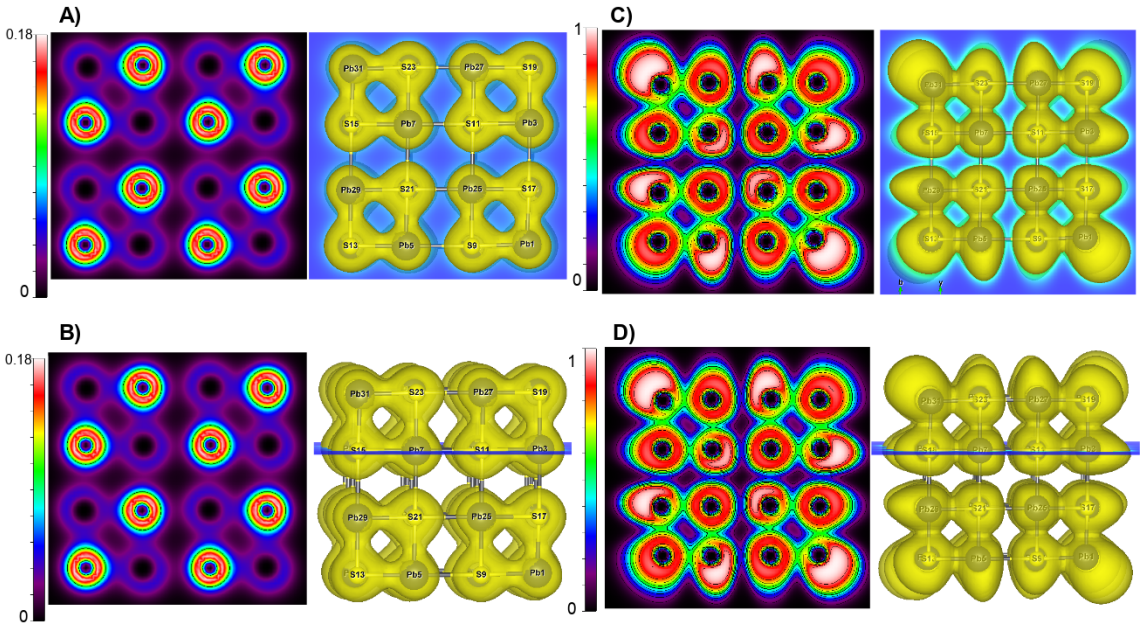

Figure 4.33: PbS relaxed 64 atom cube, top left corner atom is Pb. A) and B) 2D charge density plots for two [100] planes. C) and D) 2D ELF plots for the same two [100] planes as A) and B) respectively.

table 4.2 The minimum value of the ELF between each pair of atoms is listed for comparison. In the blue line plots the ELF in the 3-coordinated atoms bonding region has intensified from the rigid cube (S 19-Pb 27 and S 23-Pb 31) and the ELF in the region between the clusters has diminished (Pb 27-S 23). As in the rigid cube, the orange profiles between Pb atoms are the most distorted and show asymmetry in

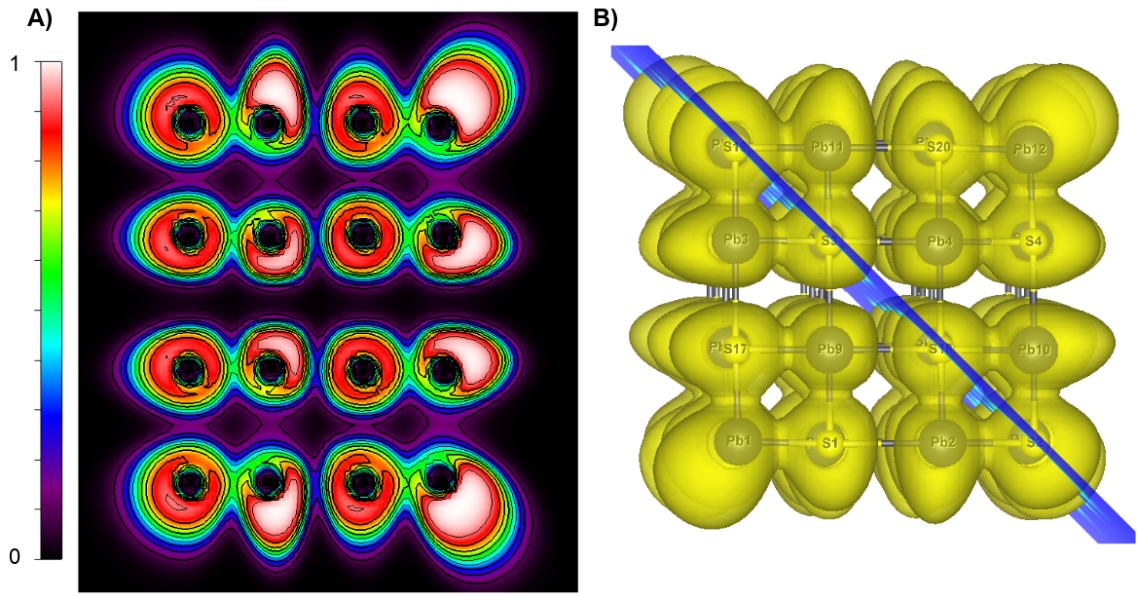

Figure 4.34: PbS relaxed 64 atom cube, top left atom is S. A) 2D ELF plot of the [110] plane shown in B).

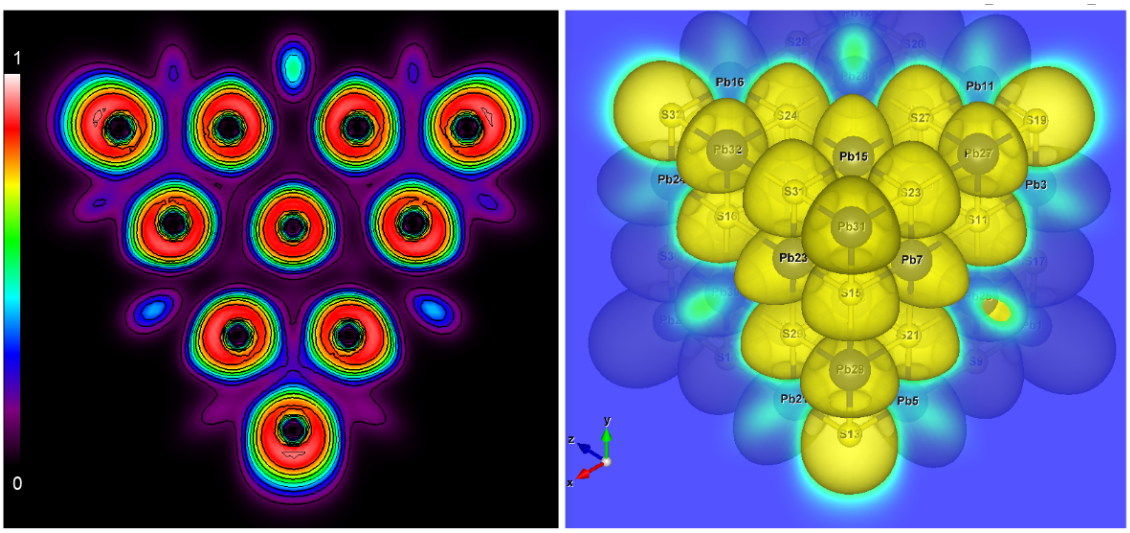

Figure 4.35: PbS relaxed 64 atom cube, all atoms are S. Left: 2D ELF plot of the [111] plane shown on the right.

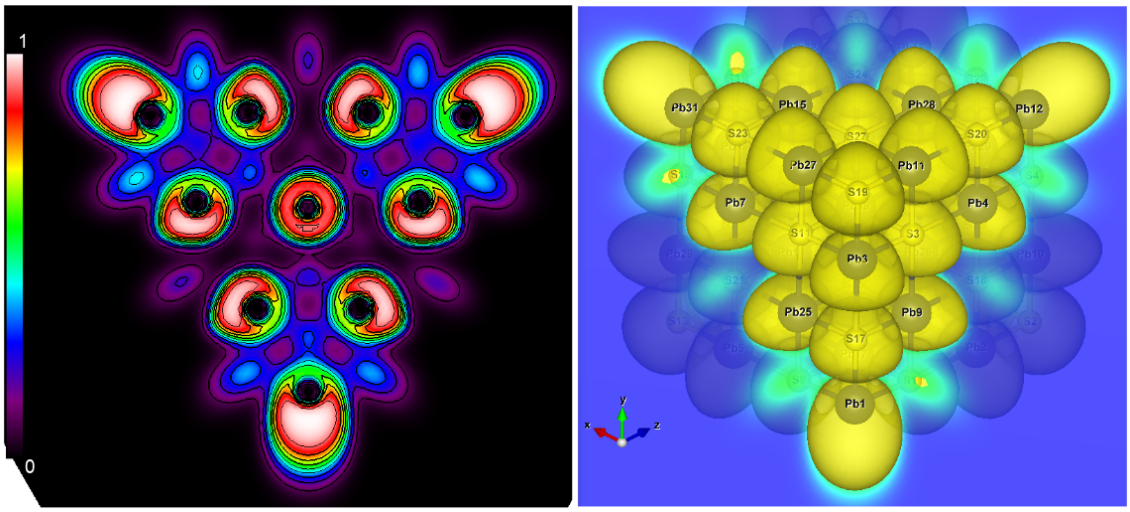

Figure 4.36: PbS relaxed 64 atom cube, all atoms are Pb. Left: 2D ELF plot of the [111] plane shown on the right.

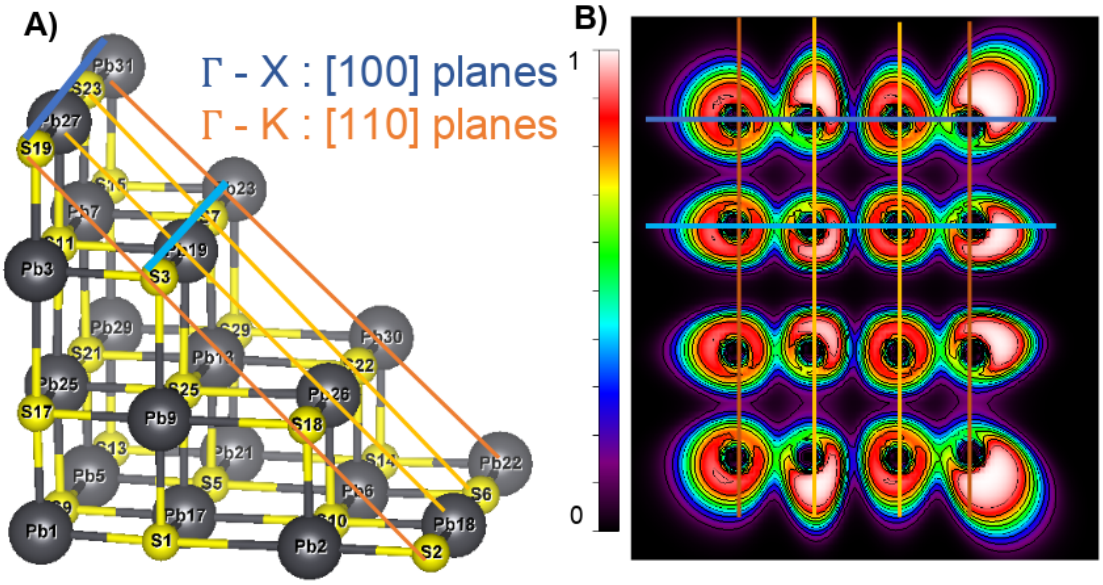

Figure 4.37: A) Truncated PbS relaxed cube. Lines show where 1D ELF line profiles were taken. Colors coordinate across this figure and figure 4.30. B) 2D ELF plot through the same [110] plane as indicated by the exposed atoms on the left. Top left atom is S

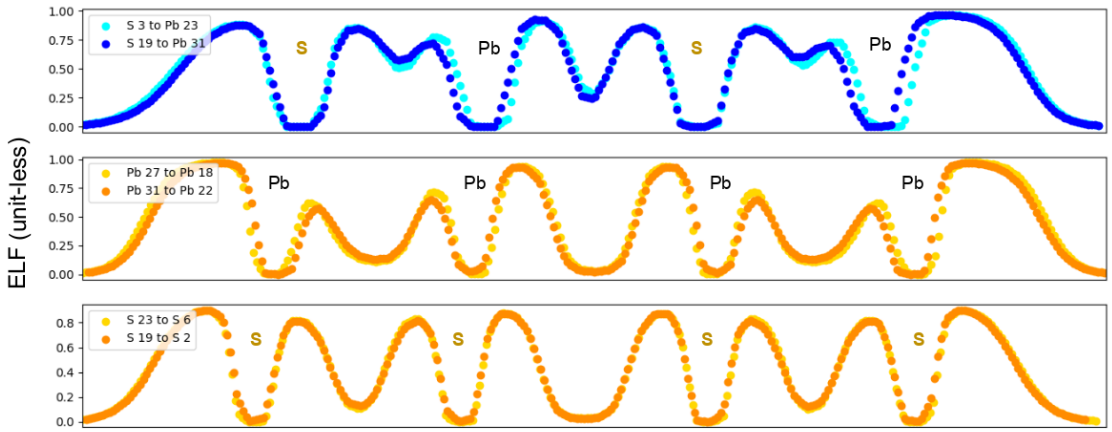

Figure 4.38: PbS relaxed 64 atom cube. 1D ELF line profile plots across the atoms indicated in figure 4.37. Atom labels on the plots indicate the location of the nucleus of the atom.

the valley between 5-coordinated Pb and 6-coordinated Pb. Essentially the interior atoms (lighter lines in all three plots in figure 4.22) look like exterior atoms.

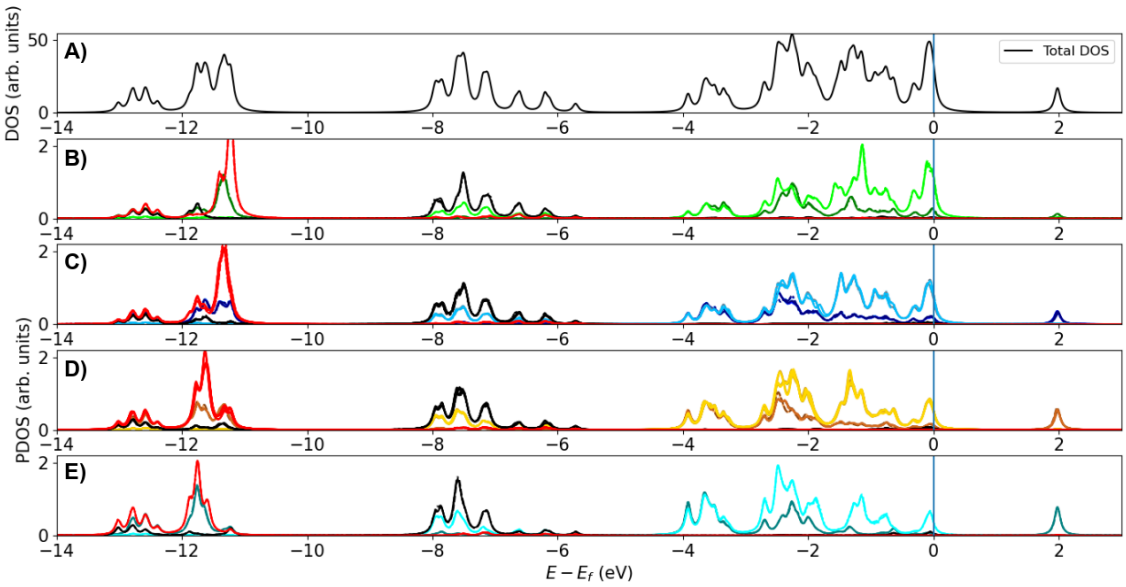

Figure 4.39: PbS relaxed 64 atom cube. A) total DOS for the entire cube. B) PDOS of the 3-coordinated atoms within the relaxed cube. C) PDOS of the 4-coordinated atoms within the relaxed cube. D) PDOS of the 5-coordinated atoms within the relaxed cube. E) PDOS of the 6-coordinated atoms within the relaxed cube. In each plot the colors are the same as for figure 4.31, namely red lines are S-s orbitals, black lines are Pb-s orbitals, dark colors are Pb-p orbitals, and light colors are S-p orbitals.

The DOS and PDOS of the relaxed cube shown in figure 4.39 is markedly different than the rigid cube. A peak around the Fermi level now appears for all atoms,

Atoms	Rigid Cube	Relaxed Cube
S 19 - Pb 27	0.46	0.58
Pb 27 - S 23	0.33	0.23
S 23 - Pb 31	0.50	0.59
S 3 - Pb 19	0.39	0.50
Pb 19 - S 7	0.34	0.28
S 7 - Pb 23	0.42	0.52
S 19 - S 3	0.08	0.12
S 3 - S 18	0.04	0.02
S 18 - S 2	0.08	0.12
S 23 - S 7	0.07	0.10
S 7 - S 22	0.04	0.02
S 22 - S 6	0.07	0.10
Pb 27 - Pb 19	0.06	0.10
Pb 19 - Pb 26	0.04	0.02
Pb 26 - Pb 18	0.07	0.10
Pb 31 - Pb 23	0.07	0.12
Pb 23 - Pb 30	0.04	0.02
Pb 30 - Pb 22	0.07	0.12

Table 4.2: The minimum ELF value between atoms in both the rigid cube and the relaxed cube.

and it is clearly separated from the next lower energy peak. Indeed four clusters of states can be identified between -4eV and 0eV in all of the plots in figure 4.39. Additionally, there is an effect on the unoccupied states with an increase of coordination. The peak at 2eV is of higher energy than the unoccupied peak in the rigid cube, due to the lowering in energy of the bonding states creating higher energy anti-bonding states. This is supported by an increase in the PDOS at -4eV as the coordination increases. The presence of Pb-p states at the Fermi level also diminishes as coordination increases.

It is interesting that the overall shape of the PDOS does not change much in the relaxed cube as coordination changes. Especially when comparing to the rigid cube which shows marked differences between the PDOS of atoms of different coordination. It suggests that the electrons are tightly bound in the clusters at the corners.

4.9.3 Corners

Due to the symmetry of a cube, within the 64 atom cube there are four equivalent corners with S atoms in the 3-coordinated position and four equivalent corners with Pb atoms in the 3-coordinated position. We choose to study the Pb 31 and S 19 corners in the relaxed cube, which we will refer to as corner 1 and corner 3. We observe a wide range of bond lengths between these 16 atoms which are represented by a histogram in figure 4.40. Two groupings of bond lengths are apparent, the shorter bond length grouping centered around 2.7 Å are found within atoms in each corner and the longer bond length grouping centered around 3.15 Å occur between the corners. In figure 4.41 and table 3, a more in-depth view of the Pierels distortion and its effect on the bonding character is shown. In the ELF line profile plots in figure 4.41, the green line represents the ELF profile of the isolated S atom. Within the corner (figure 4.41 A) and C)) the ELF profile of the S atoms is very similar to the isolated atom profile even though the bond length is much shorter than the sum of the VdW radius of an S atom in both plots.

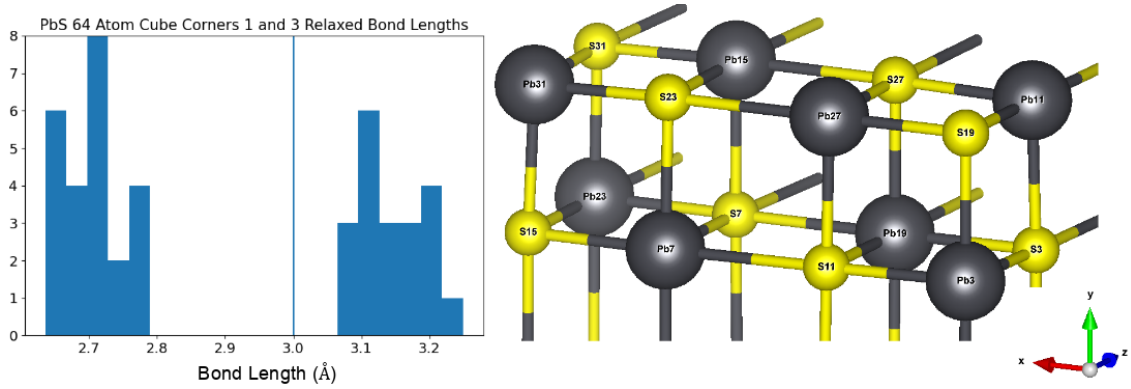

Figure 4.40: Right: Cartoon of PbS relaxed cube corners 1 and 3 with atoms labeled. Left: Histogram of bond lengths with the bulk bond length marked at 3.0 Å with a vertical line

In figure 4.41 B), the two lines are similar: the region between corners does not show much difference in the ELF between interior (S 7-Pb 19) and edge (S 23-Pb 27) atoms. The ELF profile shape and magnitude around the S and Pb atoms is similar to that of the [001] slab in the [100] plane. The bond length of the edge atoms experiences a small distortion (3.1 Å) while the interior atom bond length mainly

remains the same (3.0 Å). The ELF profile around the S atom is contracted in this direction as compared to the S atoms in panel A) and C) as well as the isolated S atom (green line). However as shown in table 3 the maximum value of ELF of the S atom stays roughly the same across all three sites.

Overall this evidence suggests that there is a minimum of electron sharing between the corners, however there is a bond present in this region. The value of the ELF alone suggests a dipole bond however the bond length is similar to the bulk bond length. We conclude that the small but not insignificant value of ELF in this region is indicative of one electron being localized in the form of a p-p σ bond. That the profiles in panel B) appear the same despite atoms S 7 and Pb 19 participating in 11 bonds and atoms S 23 and Pb 27 participating in 7 bonds, indicates the charge is not shared equally between all the bonds in contrast to the case in the bulk. The extra charge is instead concentrated in the bonding regions between atoms in the corners.

To determine which atoms in the corners contribute to this shared charge the PDOS has been broken into contributions from each atom and are plotted for the rigid cube in figure 4.42 and the relaxed cube in figure 4.43. In the rigid cube corner 1, the largest contributions to the unoccupied peak close to 2eV is from the 3-coordinated and 5-coordinated Pb-p orbitals. The 3-coordinated Pb-p orbitals however have a larger contribution at the Fermi level. These contributions from the Pb-p orbitals are dwarfed by the PDOS from the 4-coordinated S-p orbitals. The 6-coordinated S-p orbitals play a smaller role at the Fermi level but contribute significantly at energies a few eV below the Fermi level. Largely the same trends are observed in corner 3: 6-coordinated and 4-coordinated Pb-p orbitals comprise the unoccupied states and the Fermi level is dominated by 3-coordinated S-p states.

In the relaxed cube (figure 4.43) the major change is the reduction in the intensity of the PDOS peaks and the shift of the unoccupied states to higher energy. In both corners it is the lowest coordination S atoms which contribute the most at the Fermi level, those of 4-coordination for corner 1 and the 3-coordination in corner 3.

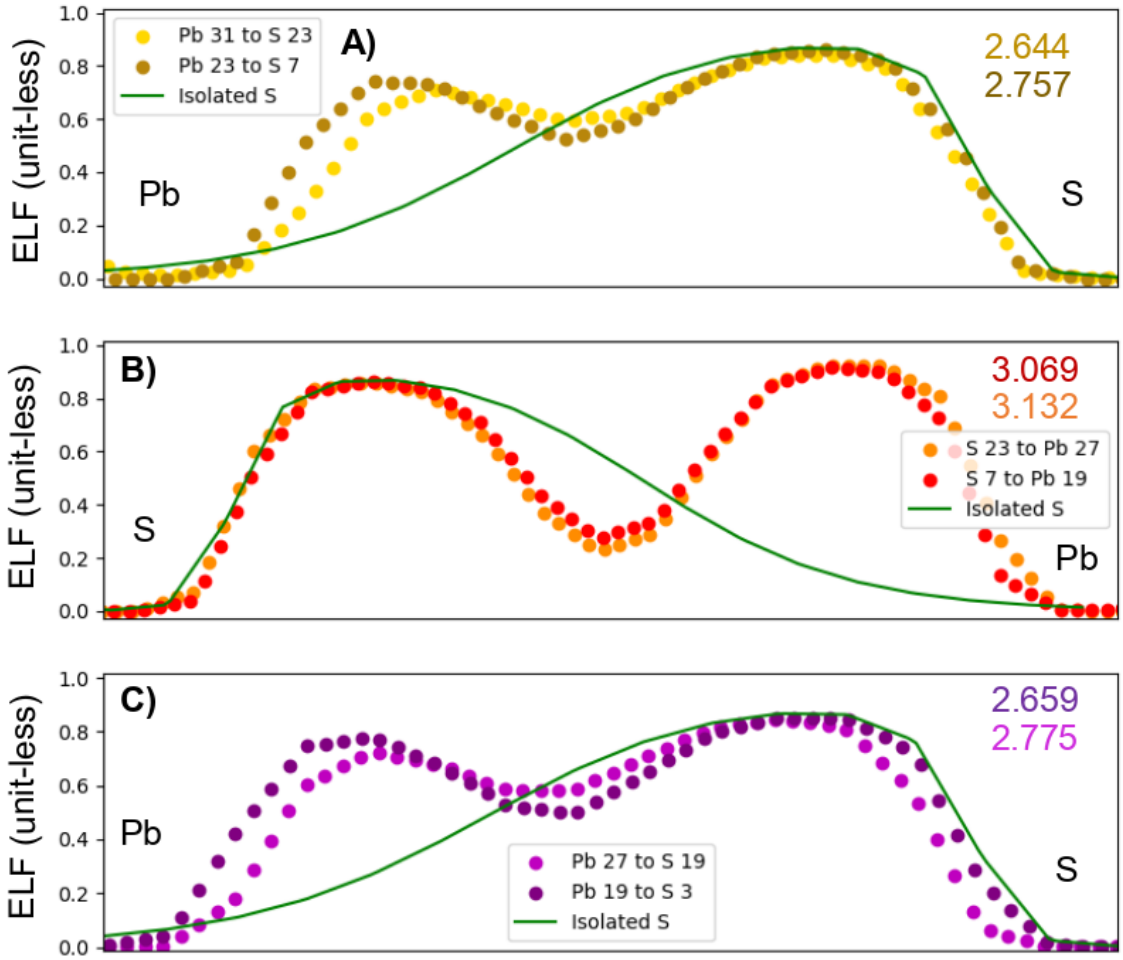

Figure 4.41: PbS relaxed 64 atom cube ELF line profile plots for atom pairs within the corners. Atom names on the plot indicate the location of the nucleus. Numbers in the top right corner correspond to the bond length between atoms for the matching color pair. Green line represents the ELF line profile of an isolated S atom.

Edge Atoms	Bond length between atoms	MAX ELF value at Pb	Min ELF value between atoms	MAX ELF value at S
Pb31-S23	2.644	0.711	0.594	0.842
S23-Pb27	3.132	0.922	0.230	0.857
Pb27-**S19**	2.775	0.721	0.582	0.846

Interior Atoms	Bond length between atoms	MAX ELF value at Pb	Min ELF value between atoms	MAX ELF value at S
Pb23-S7	2.757	0.740	0.526	0.861
S7-Pb19	3.069	0.918	0.282	0.865
Pb19-S3	2.659	0.784	0.507	0.857

Table 3: Two tables containing data for the ELF line profile plots in figure 4.41. Pb31 and S19 are in bold font to emphasize they are 3-coordinated corner atoms. The values which correspond to the ELF and bond length between corners is in red font to emphasize the large variation, which is not the case for the S atom ELF values. Bond length is given in Å.

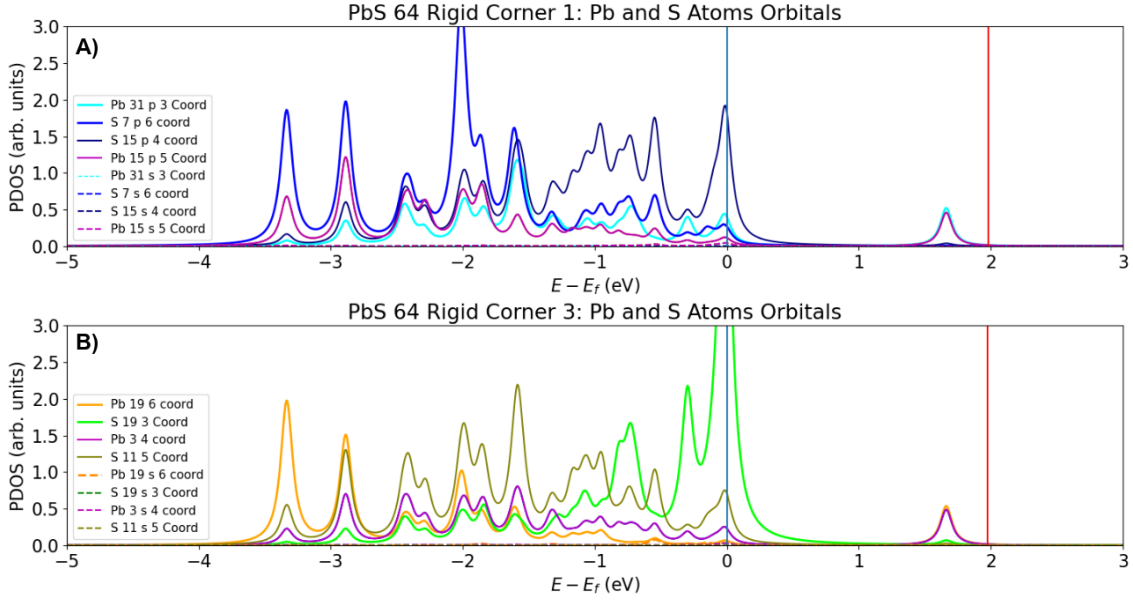

Figure 4.42: PbS rigid 64 atom cube PDOS for A) corner 1 and B) corner 3. Vertical red line indicated the energy of the unoccupied state in the relaxed cube.

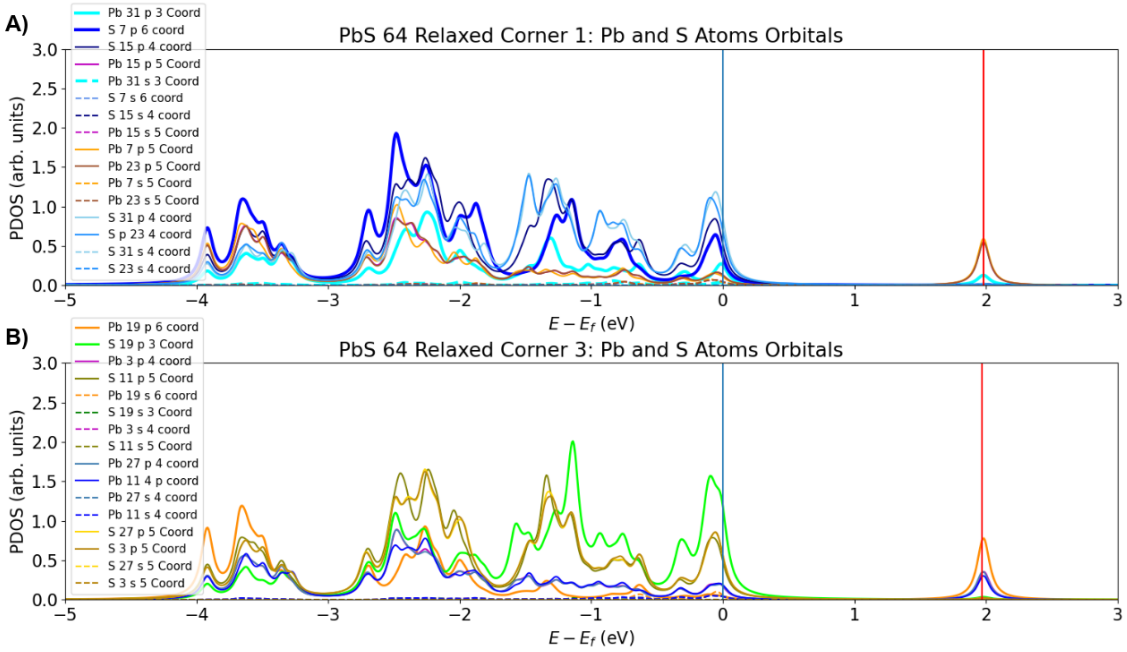

Figure 4.43: PbS relaxed 64 atom cube PDOS for A) corner 1 and B) corner 3.

4.10 Discussion

The data presented here offer valuable insights into the electronic environment of nanoscale PbS structures. Multiple unanswered questions are able to be answered by considering the 2D and 1D ELF plots for the slabs and cubes, which according to the authors of ref [43] can uniquely characterize the bonding character. Accompanied by the DOS and PDOS, a picture can be obtained of how the low coordination of surface atoms change the occupations of the energy levels. This data can also show effects of Pb-rich [111] surfaces on the overall character of the system.

Bonding

First to be addressed is the nature of the bonding in PbS QDs. In the bulk, PbS shows metavalent bonding behavior characterized by p-p σ bonds between each atom and a delicate balance between electrons shared and electrons transferred. This is reflected in ELF plots of bulk lead chalcogenides by areas of constant ELF showing directional orientation between bonded atoms (figure 4.44). It is known however that metavalent bonding can give way to ionic or covalent bonds if the crystal structure

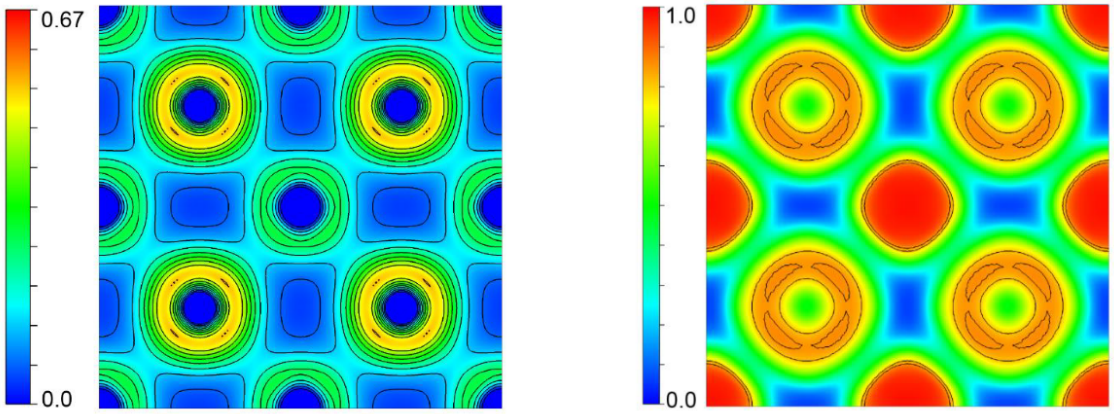

Figure 4.44: Valence charge density (paw cores omitted, left) and valence ELF (right) for PbTe. The representation is made in the [100] plane. Pb atoms are at the center of the figures. [42]

is distorted enough [94]. Given the known structural distortion in PbS surfaces [133] does metavalent bonding break down in nanoscale geometries?

From the analysis of the ELF plots as well as the bond lengths, the answer is no. In the slabs where the bond length was kept constant at the bulk bond length of 3.0 Å, all of the regions between atoms in the bonding directions typical of the rock-salt structure lack signatures of ionic, covalent, or metallic bonding. The minimum value of the ELF in these regions is larger than any Van der Walls interaction or dipole bond save the hydrogen bond. This indicates a strong interaction between atoms that correlates with the description of the metavalent bond.

However even with metavalent bonding, an overall metallic characteristic can be seen in the [111] slab DOS and PDOS data (figure 4.23) due to the ratio of Pb:S atoms in the [111] slab deviating from stoichiometry (Pb:S = 1.5). This metallic character manifests in an extended metallic-like state in the surface [111] plane of the [111] slab which can be seen in the ELF plots in figure 4.22 B) plot 2 and figure 4.21 A). The influence of this surface state propagates through the slab and induces a similar, if reduced, behavior in the second and third layers from the surface. This effect can be seen in the PDOS in figure 4.23 B), C), and D) as well as the ELF in figure 4.21 B). This result encourages a further analysis of the effect coordination plays on the occupation of the electronic states which is achieved through study of

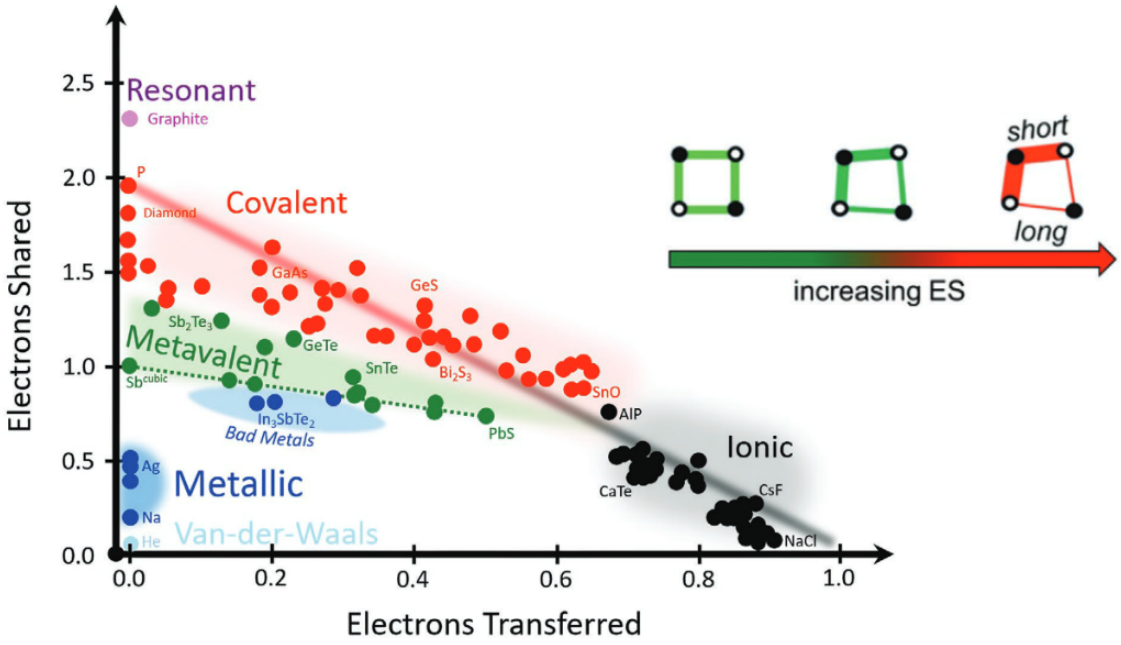

Figure 4.45: 2D map classifying chemical bonding in solids. The map is spanned by the number of electrons shared between adjacent atoms and the electron transfer renormalized by the formal oxidation state. The dotted lines denote the pseudo-binary lines connecting material systems which demonstrate the transfer from metavalen (green) to covalent (red) bonding. Upper right: a scheme demonstrating the effect of increased electron sharing on the R_{long}/R_{short} ratio. [94]

the 64 atom cubes.

Before focusing on the role of low coordinated atoms, signatures of metavalent bonding do appear in the 64 atom cubes. Metavalent bonding breaks down when the crystal structure distorts so much that the balance between electrons shared and electrons transferred tips too far in one direction (figure 4.45). In the rigid cube, while an increased amount of ELF is observed between atoms in the corner clusters, there is not an accompanying increase of electron charge in these regions (figure 4.25). The increase in ELF can be understood as increased electron sharing in the corner clusters at the expense of electron sharing between corners. The charge density remaining essentially the same as in the 2D slabs indicates the same σ bonding is occurring in the 64 atom cube. The high ELF in the corner clusters of the relaxed cube is more pronounced, supporting the idea that the R_{short} bonds created from the Pierels distortion is a result of more electron sharing. While there is clearly more charge density between atoms within a corner cluster in the relaxed

cube (figure 4.33, as compared to the rigid cube and slabs (figures 4.25, 4.16 and 4.18), there is still charge density between the corners as well as a significant value of ELF.

Analyzing the difference between the DOS and PDOS in the rigid cube and the relaxed cube non-bonding directions may give further insight into the electronic environment of nanostructured PbS. Looking first at the rigid cube, with bond lengths between all atoms the same as in the slabs, the PDOS from the 3-coordinated Pb atoms indeed shows a small concentration of states at the Fermi level (figure 4.31 B)). The reduced amount of PDOS in the rigid cube compared to the [111] slab surface atoms may be a result of the fact that these 3-coordinated rigid cube atoms are bonded to 4-coordinated S atoms, whereas in the [111] slab the 3-coordinated Pb atoms are bonded to 6-coordinated S atoms. As shown in figure 4.9.2, the R_{long}/R_{short} ratio is within the limits for metavalent bonding to occur as outlined in ref [94].

In the ELF line profile plots in figure 4.41 B), the two lines are similar: the region between corners does not show much difference in the ELF between interior (S 7-Pb 19) and edge (S 23-Pb 27) atoms. The ELF profile shape and magnitude around the S and Pb atoms is similar to that of the [001] slab in the [100] plane. The bond length of the edge atoms experiences a small distortion (3.1 Å) while the interior atom bond length mainly remains the same (3.0 Å). The ELF profile around the S atom is contracted in this direction as compared to the S atoms in panel A) and C) as well as the isolated S atom (green line). However as shown in table 3 the maximum value of ELF of the S atom stays roughly the same across all three sites.

Overall this evidence suggests that there is a minimum of electron sharing between the corners, however there is a bond present in this region. The value of the ELF alone suggests a dipole bond however the bond length is similar to the bulk bond length. We conclude that the small but not insignificant value of ELF in this region is indicative of one electron being localized in the form of a p-p σ bond. That the profiles in panel B) appear the same despite atoms S 7 and Pb 19 participating

in 11 bonds and atoms S 23 and Pb 27 participating in 7, indicates the charge is not shared equally between all the bonds in contrast to the case in the bulk. The extra charge is instead concentrated in the bonding regions between atoms in the corners. This concentration of charge is consistent with the breakdown of metavalent bonding as discussed in ref [94] and figure 4.45, however as stated above there is enough evidence to argue that the metavalent bonding has not completely broken down. It is likely much weaker than the bulk.

Atomic Coordination

Returning to the role of the low-coordination atoms to the overall electronic environment, it is important to identify which orbital interactions are playing the biggest roles. From the DOS plots of all the toy models it is clearly the p-orbitals which dominate the interactions around E_f, in agreement with the literature. However the number of bonds an atom participates in has an effect on the DOS due to the change in number of electrons participating in bonding and antibonding orbitals and the energies which the electrons occupy. In the rigid cube (figure 4.31) the lowering in energy of the lowest energy states (between -10eV and -12eV) confirm the greater energetic stability of more coordination. This is accompanied by an increase in the density of energy levels near -4eV. The unoccupied energy states do not change with coordination.

The situation in the relaxed cube changes quite significantly. A prominent peak around the Fermi level appears for all atoms, and there is a more pronounced separation between the next lower energy peak. The highest energy occupied states roughly form four clusters between -4eV and 0eV in all of the plots in figure 4.39. The presence of four clusters in the PDOS is readily identified regardless of coordination of the atoms. There is also a non-negligible difference in s-orbital DOS at the fermi level between rigid and relaxed cubes

Additionally there is an effect on the unoccupied states with an increase of coordination. The relaxed cube unoccupied states peak is at 2eV, which is higher in

energy than the unoccupied peak in the rigid cube. This is likely due to the lowering in energy of the bonds in the relaxed cube from the Pierels distortions in the geometry. This is supported by an increase in the PDOS at -4eV as the coordination increases. The presence of Pb-p states at the Fermi level also diminishes as coordination increases.

The changes from the bulk bond length (3.0 Å) in the relaxed cube suggests there may be a large deviation from the bulk electronic environment, as would be consistent with experimental evidence [33] [11] [13]. The clustering behavior observed in the ELF and the PDOS of the relaxed cube is certainly unique to the nano-regime. That it can be identified in the rigid cube data indicates that it is a result of effects from low-coordinated atoms at the surfaces propagating in a non-local way through the material. However as clustering is not observed in the 2D periodic slabs, the effect from the surface atoms is a slight increase in the ELF in the regions around the surface atoms. It appears a sufficient number of low coordinated atoms is needed to produce the clustering behavior. What the sufficient number is cannot be answered by the results of this study and is a topic of future work.

Quantum Confinement

Not discussed so far is how quantum confinement might affect the metavalent bonding. Quantum confinement increases the kinetic energy of the electron states and leads to larger separation between discrete energy levels. This leads to higher kinetic energy of the electrons which is reflected in the ELF values, as can be seen in the max mid-bond ELF value of 0.39 in 3-coord PbS slab to 0.59 in 3-coord cube, and the high intensity ELF regions on the surface of the cube. With many atoms participating in fewer bonds, the electrons are less localized in a particular direction. The regions with very high ELF are more spread out over space. Quantum confinement may be the reason why, despite the clustering of electron sharing at the corners, the evidence for metavalent bonding still persists.

4.11 Conclusions

We studied nanoscale PbS structures using the Octopus DFT code, a software package specifically created to study finite structures at the atomic scale through real-space calculations. An analysis of the bonding character was undertaken by examining electron localization functions, density of states, projected density of states, and bond lengths.

Within the relaxed, stoichiometric, 64 atom cube we found evidence that the metavalent bonding of the bulk PbS persists, but supports small clusters of atoms with increased ELF in the regions between the atoms. These regions are reminiscent of a metallic type bond, but differ in that they are localized in particular planes between the atoms. The overall character of the nanostructure, however, does not become metallic.

The bonding in nanostructued PbS is strongly affected by atomic coordination. It appears that an enhanced bonding state occurs in PbS nanostructures which contain a large amount of low coordinated atoms with respect to higher coordinated atoms. Further study is required to determine the exact ratio of 6-coordinated atoms to lower coordinated atoms which allows for the formation of clusters. In our study the clustering behavior was not observed in the slab geometries, regardless of stoichiometry, where 40% of the atoms were of low coordination residing on the surface. The 64 atom cube did show this behavior, with 87% of the atoms being low coordinated and on the surface. The effect was enhanced when the geometry was allowed to relax and the bond lengths were allowed to change.

Quantum confinement also plays a large role in the spatial distribution of electrons which directly effects the atomic bonds. The maximum mid-bond ELF value for a 3-fold coordinated Pb bond in the [111] slab was found to be 0.39, where in the 3-fold coordinated Pb bond in the 64 atom cube it was found to be 0.59. Quantum confinement increases the kinetic energy of the electron states which may lead to different behavior from that which is seen in the bulk. Specific planes of atoms, which correspond to specific directions in the Brillouin Zone (see figure 2.4), show high

Atom	VdW radius (Å)	Sum of VdW radii (Å)	Electronegativity	Electron Affinity (eV)	
Pb	2.02		2.33	0.36	
S	1.80	PbS:3.82	2.58	2.07	
Se	1.90	PbSe:3.92	2.55	2.02	
Te	2.06	PbTe: 4.08	2.1	1.97	
Ge	2.11	GeSe:2.01 GeTe:2.09	2.01	1.35	
Sb	2.06	SbTe:2.06	2.05	1.07	
Bi	2.07		2.02	0.94	
Sn	2.17		1.96	1.2	

Table 4: Van der Wall Radii, electronegativities, and electron affinities for selected atoms.

levels of ELF between atoms even in the absence of a bond. In particular, the [111] planes of atoms which correspond to the bulk band gap and are therefore important for optical properties, show significant values of ELF in non-bonding regions in the slabs as well as the 64 atom cube. Correlating the number of bonds an atom has to the PDOS in the 64 atom cube, there is an effect from coordination to the number of states near the Fermi level, as can be seen from figure 4.39. Both the S states and the Pb states are affected by the atomic coordination. S states at the Fermi level are at a maximum with lower coordination, while Pb states above the Fermi level are at a maximum with higher coordination.

Observations indicate that if the Pb:S ratio is too much disturbed however, the semiconducting state is lost and an overall metallic character prevails, as shown in the [111] slab. The exact ratio of Pb:S atoms for which the material transitions from semiconducting to metallic is at this point unknown. In this study we have examined structures with a Pb:S ratio of 1 and 1.5. Kim et. al. [118], a semiconducting to metallic transition was found for Pb:S ratios somewhere between 1 and 1.44. Because of the FCC crystal structure of PbS, finding the exact geometries which produces the ratios which are close to the transition point is challenging and requires further study.

Chapter 5

Summary and Outlook

Within the realm of solid state physics, the effects of symmetry on the properties of materials has been studied and described in a mathematically rigorous way for close to a century [134] [135] [136] [137] [138]. Physicists have successfully traced the cause of several macroscopic phenomena back to atomic symmetry origins. However applying this theory to real systems continues to be a formidable challenge. In this dissertation we have studied the effect of atomic symmetry and spatial arrangement on the nature of the atomic bonds.

First, in chapter 3, we examined the spatial symmetry within a bulk crystal and its effects on the elastic deformation properties of LiMg alloys as characterized by the elastic constants. The amount of energy required to cause deformations in a crystal is influenced by the arrangements of the atoms. For example, slip planes usually occur in close-packed directions and move in a direction perpendicular to a relatively longer bonding direction. Either making the lattice parameters equal, as in cubic structures, or different enough to remove a singular low energy preference will encourage competition between possible deformation mechanisms and increase ductility. While at the onset our goal was to find cubic structures, we made no restrictions to our structure search and systematically looked for realizable structures. We found a rich array of structures at varying compositions and symmetries. After calculating the elastic constants we observe that the addition of Li to Mg does not necessarily cause the resulting crystal structures to be more symmetric, but it

does introduce changes to the crystal structure that improve the elastic properties. These effects can be seen in our results though the low-Li content cubic Li_1Mg_3 and monoclinic Li_1Mg_{13}, which have similar values of elastic constants despite drastically different symmetries. This result suggests that continuing the search for a lightweight yet ductile alloy should shift to considering more than just the symmetry. Given the results of the binary search, a promising next step would include expanding the search space by including a third element to the composition.

Second, in chapter 4, we examined the effects of reduced symmetry within spatially restricted PbS nano-structures on the character of atomic bonds and the redistribution of charge as characterized by the electron localization function and the density of states. While PbS nano-structures continue to be the subject of intense research [139], some of their properties are not fully understood. Given the recent discovery and characterization of metavalent bonding in bulk PbS [93] it is relevant to investigate the nature of the bonding in nanoscale structures of PbS.

Our results show that metavalent bonding does persist in the nano-regime, however the reduced symmetry at the surfaces has a profound impact on the electron localization within the bonds. When examining just one terminated surface, modeled by a 2D periodic slab terminated in either the [001] or [111] plane, it was found that deviation in stoichiometry has the ability to change the character of the electronic states from semiconducting to metallic. It was also possible to observe an influence of the lower-coordinated surface atoms propagating through the structure to the interior atoms. Looking further at the effects of coordination by studying a 64 atom cube, it was found that small clusters of atoms form a state which looks metallic, however it is localized spatially and energetically so that the overall structure remains of semiconducting character. These states are a result of the low coordinated atoms at the edges and corners of the cube and the influence they have on the surrounding atoms.

A stronger analysis of the bonding behavior of nano-structured PbS would result from a proper calculation of electrons shared and electrons transferred between

atoms, as is done in refs [94] and [42]. These quantities are calculated through integration of the Bader basins and ELF basins around each atom. The critic2 software [140] is designed to perform integrations of the charge density and ELF data. A next step in quantifying the bonding behaviour would be to use the critic2 package to calculate exact values for electrons shared and electrons transferred.

The PbS toy models studied here have demonstrated the benefits of understanding the primary mechanisms which influence a material's properties. However in reality we know the situation is much more complicated. PbS nano-structures do not exist in a vacuum; there are ligands, solvents, atmospheric effects such as pressure and temperature, as well as background electric fields or even bias voltages in some applications. We would also like to further investigate the effect of overall shape on the energy states and electron localization inside the nanostructure. A more realistic cuboctahedron shape, and shapes with more internal 6-coordinated atoms, could reveal the extent of the influence low-coordination atoms have overall. Including any of these considerations into the model is an important next step in fully understanding the properties and performance of these materials.

5.1 Future Work

Preliminary data in figures 5.1-5.7 shows that further analysis in optically active nanoscale systems can be carried out. A closer inspection of not only the atomic contribution to the PDOS, but the contribution from individual orbitals may reveal direction specific features of the electronic environment. These can be correlated in real space by inspection of the wave functions. These features may then be shown to contribute to the optical absorption through the optical selection rules and the strength function.

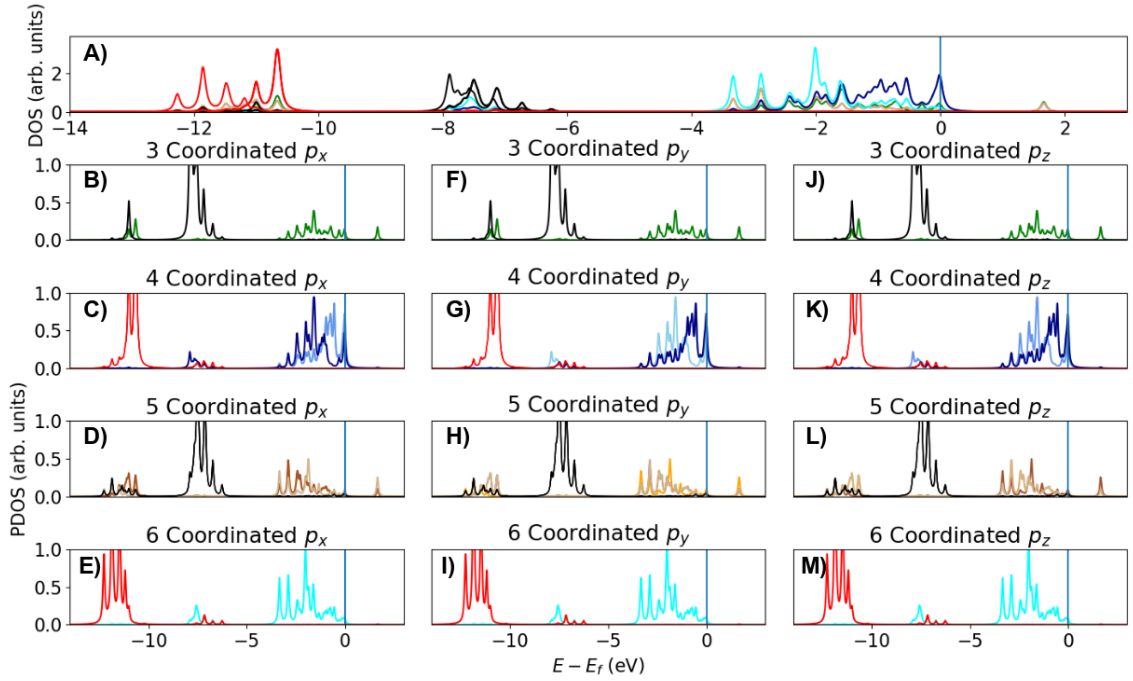

Figure 5.1: PbS rigid 64 atom cube corner 1 DOS and PDOS for p and s orbitals.

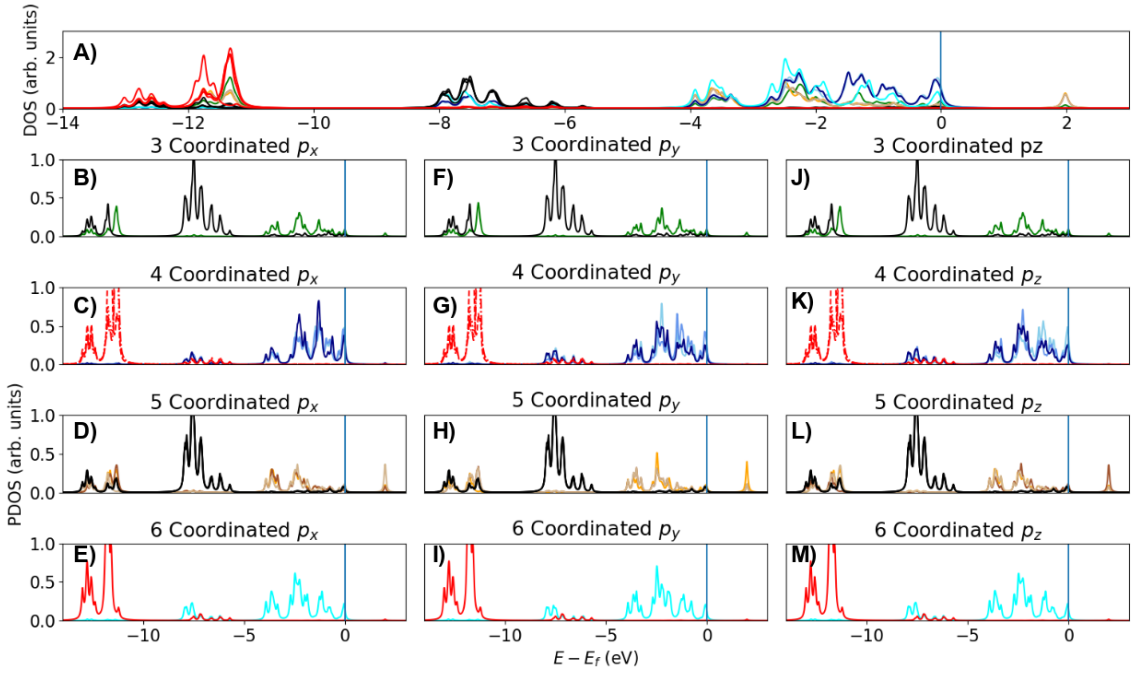

Figure 5.2: PbS relaxed 64 atom cube corner 1 DOS and PDOS for p and s orbitals.

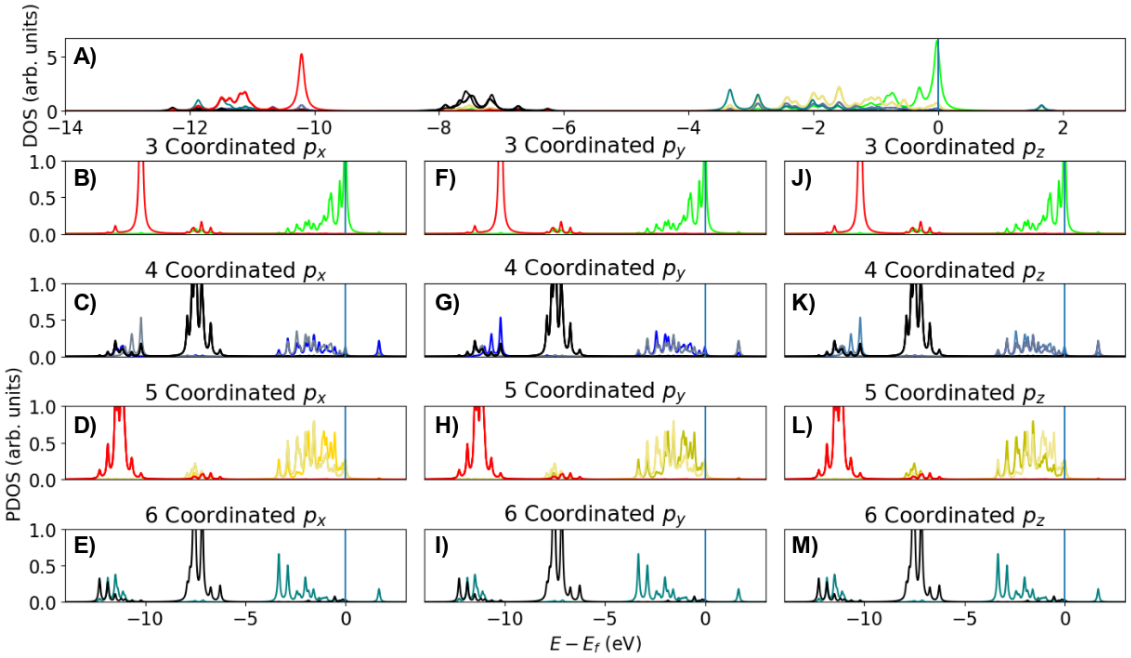

Figure 5.3: PbS rigid 64 atom cube corner 3 DOS and PDOS for p and s orbitals.

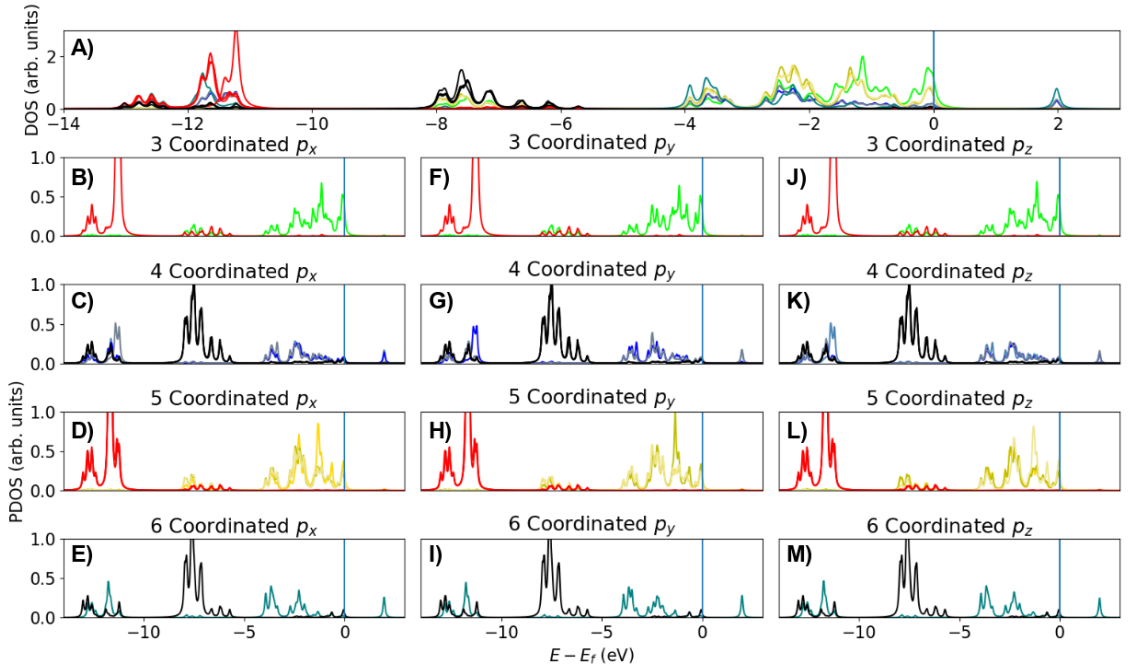

Figure 5.4: PbS relaxed 64 atom cube corner 3 DOS and PDOS for p and s orbitals.

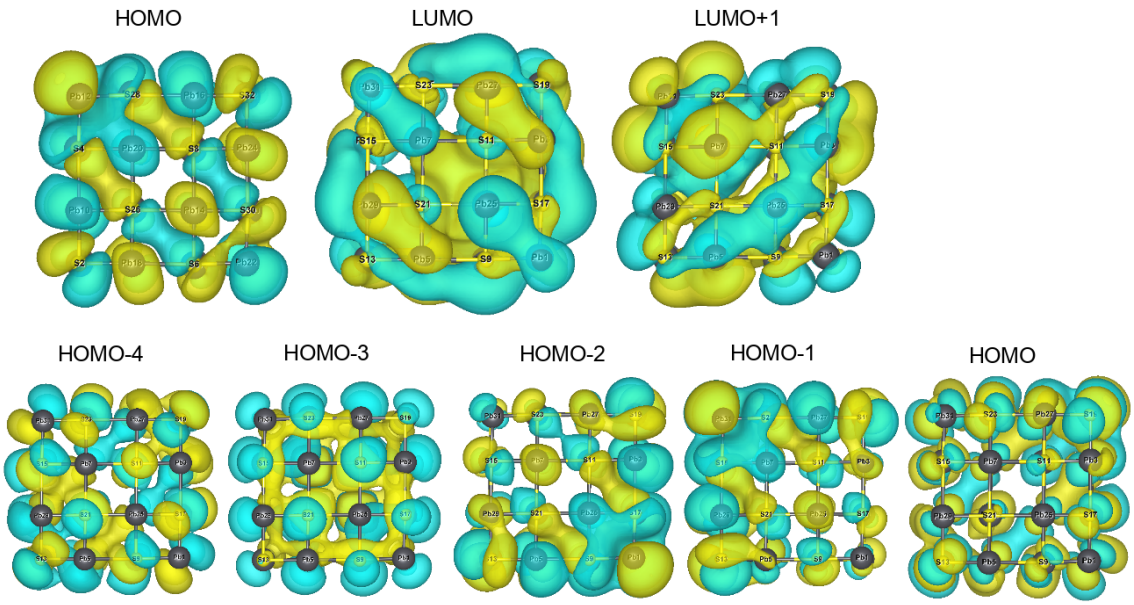

Figure 5.5: The PbS relaxed 64 atom cube wave functions for states around the Fermi level. The HOMO wave function is plotted twice showing two different orientations.

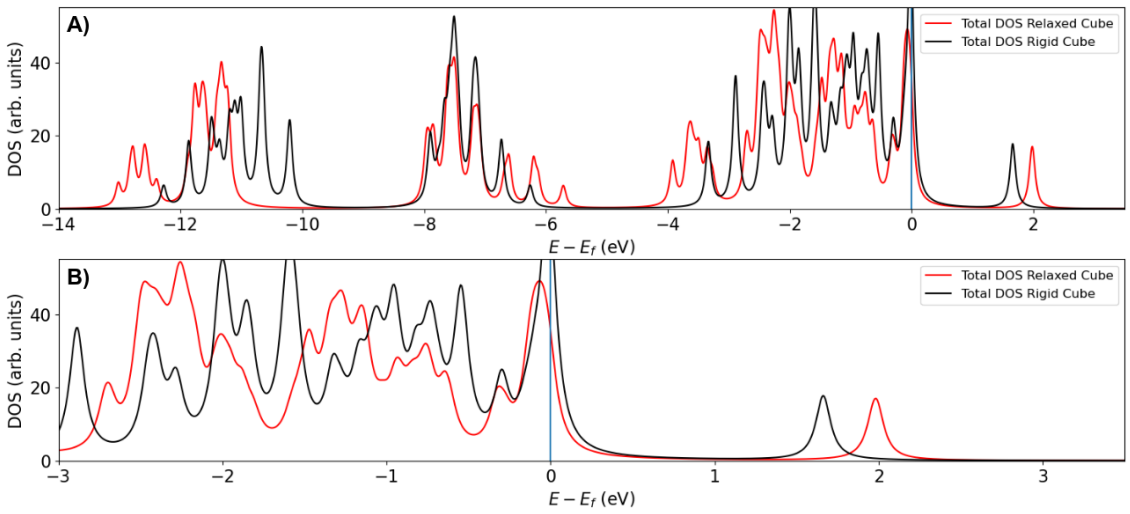

Figure 5.6: PbS relaxed and rigid 64 atom cube DOS plotted together. A) is the total energy spectrum and B) is zoomed in around E_f.

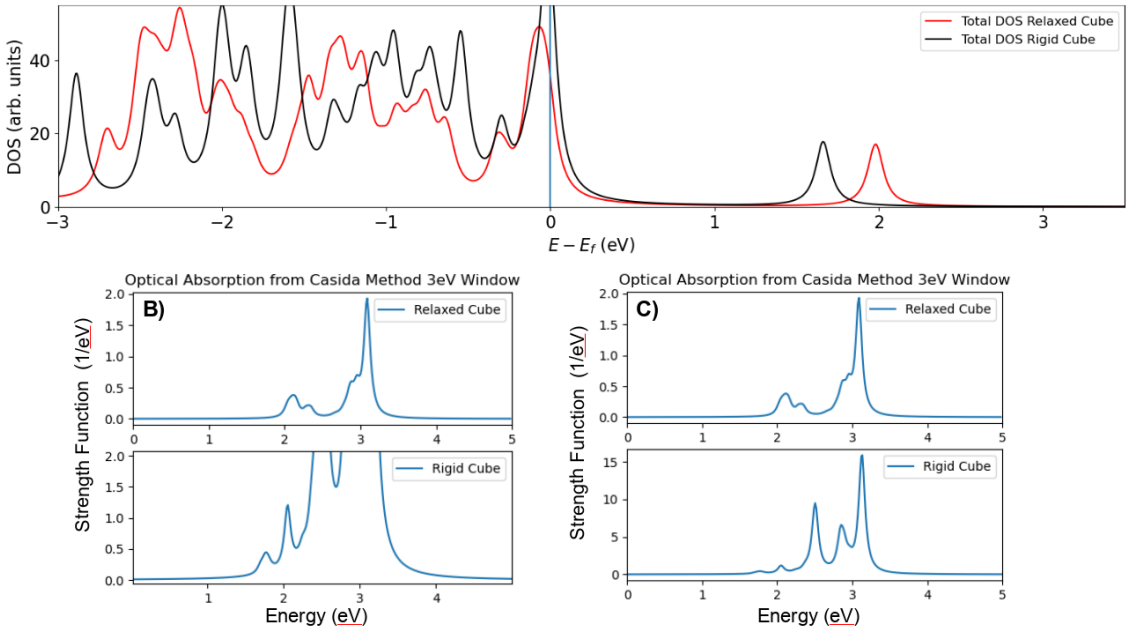

Figure 5.7: The 64 atom rigid and relaxed 64 atom cube optical absorption as given by the strength function. Top panel shows total DOS for both cubes plotted together. B) shows the full function for the relaxed cube (top) and the zoomed function for the rigid cube (bottom). C) is the same as B) but showing the full energy range for both rigid and relaxed cubes.

Appendix A

Adventures in Open Source Software

A.1 Introduction

In the timeline of when the work in this dissertation was carried out, the author learned the VASP code and carried out the LiMg study (chapter 3) calculations first. In hindsight this was a fortuitous circumstance. The major advantage was that the knowledge and experience gained during this study allowed for the PbS study of chapter 4 to be carried out. The experience of using the VASP code was also much more pleasant.

While both DFT codes essentially do the same job, it is worth nothing that VASP is a complete, commercially licensed code. For the user this means fully functional capabilities, minimal bugs, and a robust support system to include an extensive base of users accessible though an online forum. In using VASP, and the post-processing codes which interface with VASP, the author had minimal issues with the code itself. The situation with Octopus however was markedly different.

In the sections below an overview of both the DFT codes utilized in this dissertation are given. This is followed by a demonstration of some of the roadblocks and pitfalls experienced by the author upon attempting to study the lead chalcogenides (PbX) using the Octopus DFT code.

A.2 VASP DFT

The Vienna Ab initio Simulation Package is a commercial code for atomic scale materials modeling. It utilizes plane wave basis sets as the mathematical foundation for solving the Schrodinger equation within the Density Functional Theory. This means that all of the calculations need to employ periodic boundary conditions, and so it is primarily suitable for 3D bulk structures. Calculations can be performed on non periodic structures, such as 2D slabs or isolated molecules, but special care needs to be applied to setting up the input geometry. In these cases a repeated unit cell with periodic boundary conditions is still used, however the atoms inside are placed in such a way that there is enough empty space between unit cells in directions that should not be extended, as described in section 2.1.2 above and shown in figure 2.5. [141]

There are many advantages to using a well-established commercial code in that most bugs have been found and fixed, there is a team of developers that reliably maintain the code and respond to inquiries, and there are numerous sources of information on how to run the code. It is also an advantage that since you have purchased the code it comes with a level of trust, that the developers have tested and verified the components and the results can be trusted without meticulous scrutiny. The major disadvantage is of course the requirement to purchase a license and the restrictive nature of that license.

A.3 Octopus DFT

The Octopus code is an open source and freely available simulation package for Time-Dependent DFT calculations in real space for electron-ion dynamics in 1, 2, and 3 dimensional finite systems subject to time dependent electromagnetic fields. It uses a regular mesh in real space to expand all quantities and solve the time dependent Schrodinger equation in the Kohn-Sham scheme. Its main advantage is for finite systems since working in real space means that only one unit cell is required. It is

also advantageous for studying quantities that are inherently expressed in real space terms such as the density and the wave functions.

There are advantages to using an open source code in that it is freely available and able to be modified by the user (provided the user has sufficient knowledge and skill in the programming language). However there are a number of disadvantages. Octopus is not nearly as robust as it is described to be, with many features only half implemented or still under development. The amount of users is more limited than with a well-established commercial code and so resources for assistance with calculations are scarce. Many functionalities, variables, and tutorials on the website are vaguely described or not described at all. The most noticeable disadvantage are the numerous warnings in the outputs and the constant reminder that the code is not guaranteed by the developers, that no results should be considered valid without a large amount of scrutiny. It is good to always be somewhat skeptical of any data used as scientific evidence, but this caveat is somewhat unsettling.

To illustrate the hazards associated with using any number of open-source codes, here we review a few examples of what went wrong over the course of producing chapter 4.

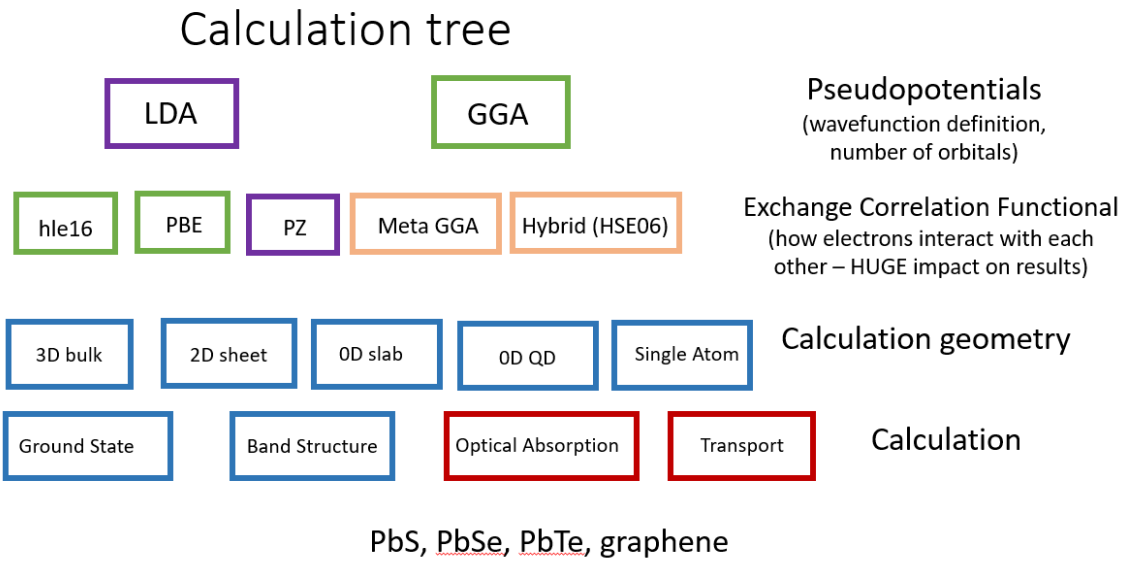

Figure A.1: A cartoon depicting the scope of the PbX study (chapter 4) circa December of 2020.

When the PbX study received full funding in Fall of 2020, the scope of the project was to investigate all three PbX compounds in various spatial configuration geometries and in relation to an interface with graphene. Figure A.1 shows a cartoon of what the author had hoped to accomplish. The first hurdle encountered was choosing the pseudopotential and exchange correlation (XC) functional.

There is not much good DFT simulation data which is good for benchmarking in the literature for spatially confined PbX geometries. There is however an abundance of this type of data for bulk PbX geometries. Therefore the author felt most comfortable in benchmarking the test calculations for pseudopotential and XC functionals on bulk structures, and then using the best choice to carry out calculations on 2D and 0D structures. This was a time intensive and laborious process which in the end did not produce conclusive results. Ultimately the choice of pseudopotential was made following the study by Murphy et. al. [26] which demonstrated that the HGH LDA pseudopotentials [29] correctly reproduce the band edge states in bulk PbTe, without SOC.

```
***************************** FATAL ERROR ******************************
*** Fatal Error (description follows)
*----------------------------------------------------------------------
* GGA with spinors not implemented.
************************************************************************
```

Figure A.2:

Studying the optical properties of a material, which was the overall goal of the study at the onset, demands that the band edge states be described accurately so that electron transitions are accurately described. However choosing an XC functional at a higher level than GGA (see 2.6) quickly limits the functionality of the Octopus code by the types of calculations that work and by time it takes the calculation to complete. Ultimately the GGA XC functional was chosen for two reasons: it worked, and it is the most commonly used XC functional in the literature which makes comparisons with published results possible.

The second hurdle encountered was in trying to optimize the geometry of the

```
Info: Generating external potential
      done.
Info: Octopus initialization completed.
Info: Starting calculation mode.

** Warning:
**   Geometry optimization for periodic systems is under development.
**   It might not work or produce wrong results.


** Warning:
**   Optimization of cell parameters during geometry optimization
**   of periodic systems is currently not implemented.
```

Figure A.3:

structures under study. There is a geometry optimization routine in the Octopus code, however as figure A.3 shows, it is not fully implemented for periodic systems. Therefore when using the 2D slab geometry we used the well known lattice constants for the bulk system. To study structure relaxation we utilized the single-unit cell 64-atom cube where the geometry optimization successfully ran.

The scope was further reduced from a study of all three PbX to only PbS due to how long the calculations were taking to converge. Much more time is needed to get a full set of data for PbSe and PbTe. PbS was the first material for which all of the calculations converged and a full analysis was able to be made. Originally the study was also to include graphene calculations, however the time taken to test the pseudopotential and XC functional choices ate into the study timeline. It was decided to leave the graphene, PbSe, and PbTe systems for future study.

Octopus provides three ways to study the optical properties of a system: the time-dependent propagation, the Sternheimer method, and the Casida method. Understanding all three and deciding which should be used was a task in itself, as the Octopus developers provide little in the way of explaining the differences, or in how to run the calculations. In addition, these methods don't always work. As shown in figure A.4, the Casida method will not work in periodic systems. It was therefore possible to calculate the transition strength function for the 64 atom cube models, but none of the other toy models. A future direction for this study would be to in-

```
Info: Generating external potential
      done.
Info: Octopus initialization completed.
Info: Starting calculation mode.

** Warning:
**   Casida oscillator strengths will be incorrect in periodic systems.


*************************** FATAL ERROR ****************************
*** Fatal Error (description follows)
*----------------------------------------------------------------------
* Casida with k-points not implemented.
************************************************************************
```

Figure A.4:

vestigate the other two methods for studying the optical properties, the Sternheimer method and time dependent propagation. Both methods are time intensive.

To better investigate the bonding in materials, ref [42] use the Bader basins and ELF basins to determine the number of electrons that are shared or transferred between atoms. This analysis requires the integration of the Bader basins and ELF basins. In theory Octopus provides this data, as shown in figures A.6 and A.5, respectively. However the information printed in these files is not well labeled and does not clearly match the other Bader and ELF output files, such as the 3D visualizations. The author attempted to ask the code developers two separate times to explain the content of the files in figures A.6 and A.5, but never received a reply. Additional software will be necessary to perform the analysis and this work is a next step for the project.

```
Number of basins =    10

#     1
  position = (   -3.822479,   -2.206909,   -1.040347) A
  value =     0.856316
  volume =     2.917383 A^3
  population =     0.470950
#     2
  position = (   -1.557306,   -0.899111,    1.271535) A
  value =     0.862589
  volume =     5.260921 A^3
  population =     1.244160
#     3
  position = (   -1.557306,    0.899111,   -1.271535) A
  value =     0.862589
  volume =     5.164611 A^3
  population =     1.240132
#     4
  position = (    0.637080,   -0.040869,   -0.462376) A
  value =     0.560211
  volume =    20.138772 A^3
  population =    12.532827
#     5
  position = (    0.000000,    1.798222,    1.271535) A
  value =     0.862589
  volume =     4.416204 A^3
  population =     1.008802
#     6
  position = (   -0.000000,   -1.798222,   -1.271535) A
  value =     0.862589
  volume =     5.375289 A^3
  population =     1.248865
#     7
  position = (    1.557306,   -0.899111,    1.271535) A
  value =     0.862589
  volume =     4.418210 A^3
  population =     1.008855
#     8
```

Figure A.5:

```
Number of basins =    37

#     1
  position = (   -4.176412,   -2.329515,   -1.733912) A
  value =     1.523206
  volume =     0.120387 A^3
  population =     0.109842
#     2
  position = (   -3.256186,   -1.961697,   -1.387129) A
  value =     0.060842
  volume =     2.796996 A^3
  population =     0.360164
#     3
  position = (   -0.566293,   -0.081737,    0.809159) A
  value =     0.646121
  volume =     5.222798 A^3
  population =     1.258755
#     4
  position = (   -2.123600,   -1.144323,    1.618318) A
  value =     1.527508
  volume =     0.198639 A^3
  population =     0.185418
#     5
  position = (   -0.920226,   -0.122606,    0.346782) A
  value =     0.646252
  volume =     0.315013 A^3
  population =     0.180358
#     6
  position = (    0.707867,   -0.408687,    0.577971) A
  value =     0.649433
  volume =    19.015158 A^3
  population =     5.625625
#     7
  position = (   -0.424720,   -0.899111,   -0.115594) A
  value =     0.645067
  volume =     0.678181 A^3
  population =     0.330670
#     8
```

Figure A.6:

Appendix B

LiMg Ground State Phonons

As noted in chapter 3, phonon plots for the structures on the convex hull are included below.

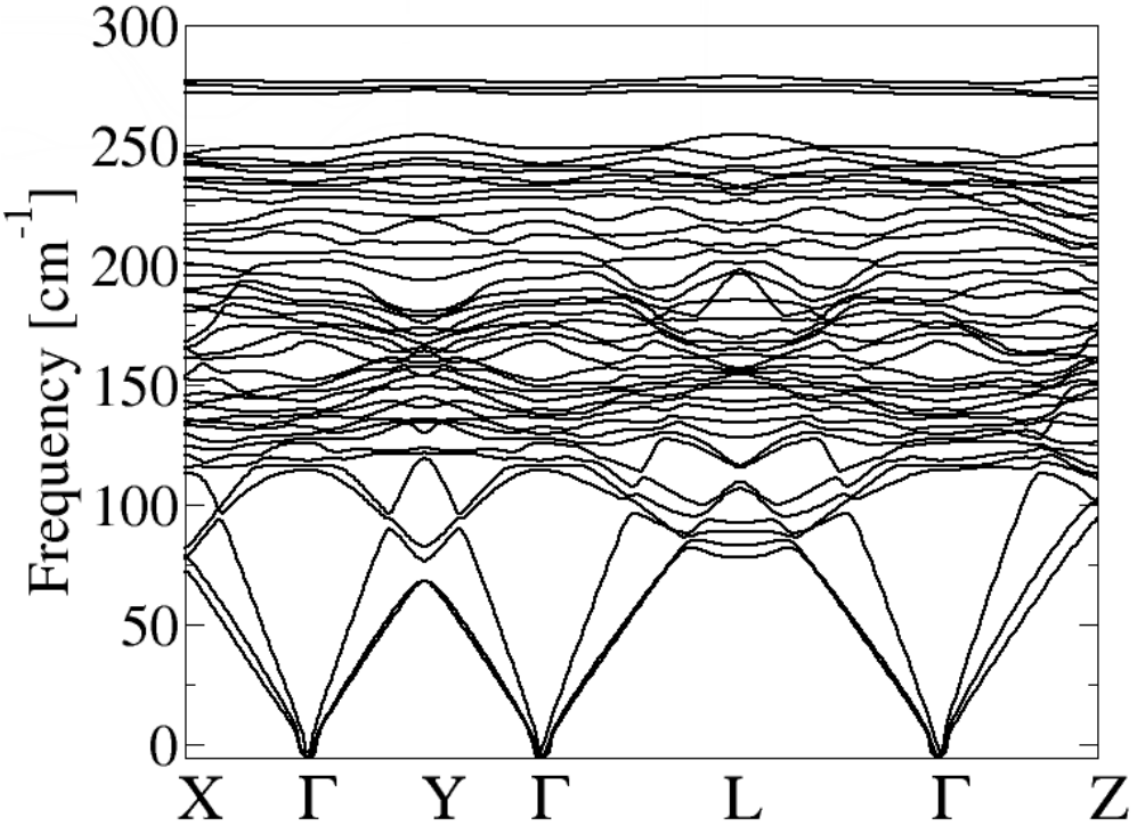

Figure B.1: Li_1Mg_{13} phonon spectra along high symmetry direction in momentum space.

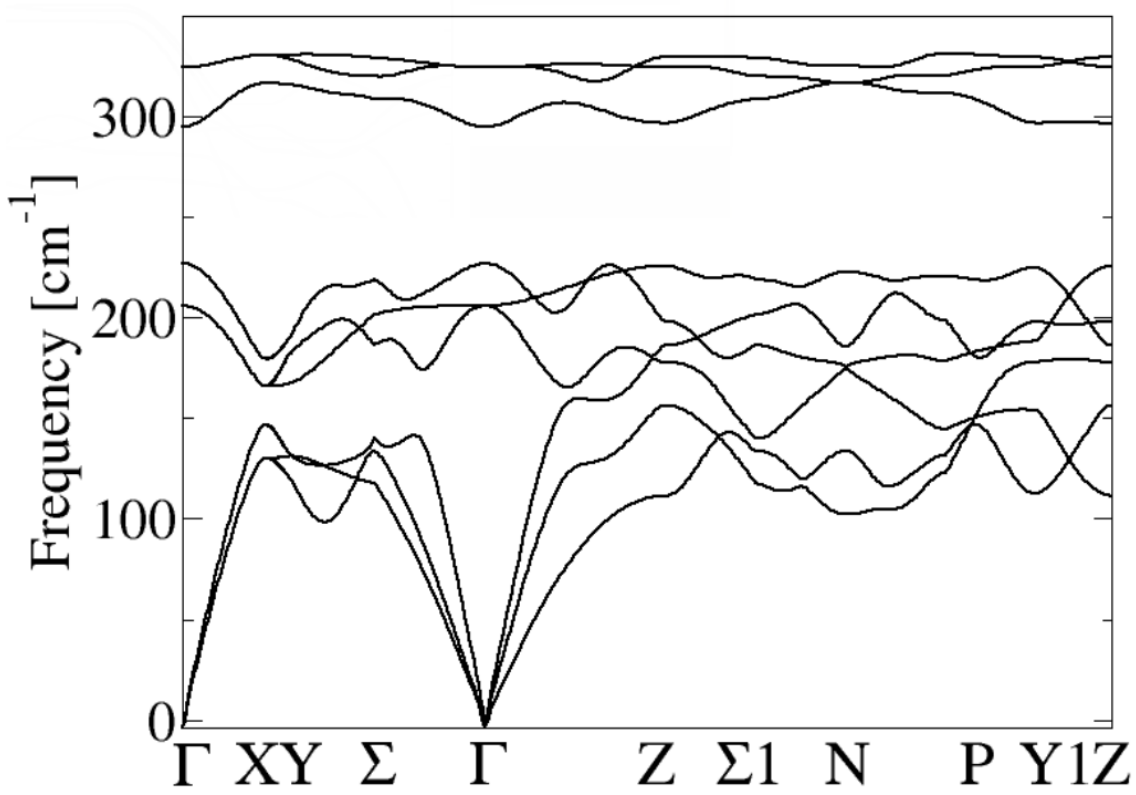

Figure B.2: Li_1Mg_2 (139) phonon spectra along high symmetry direction in momentum space.

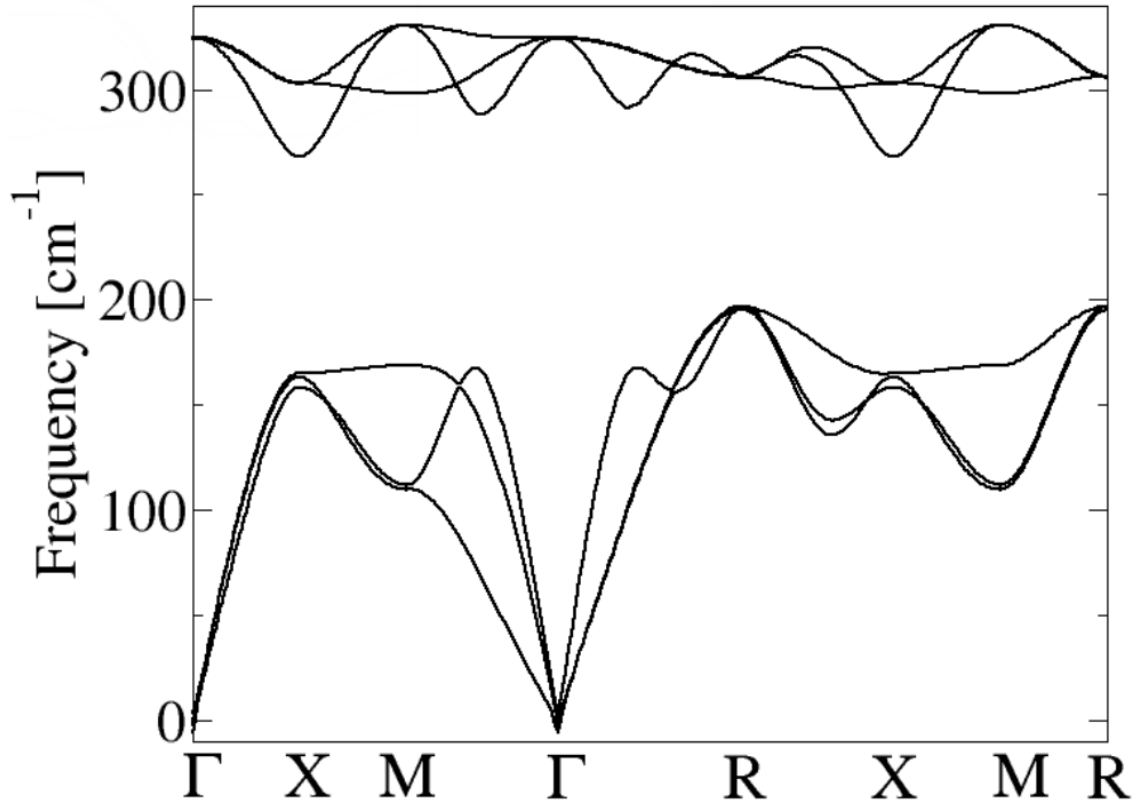

Figure B.3: Li_1Mg_1 phonon spectra along high symmetry direction in momentum space.

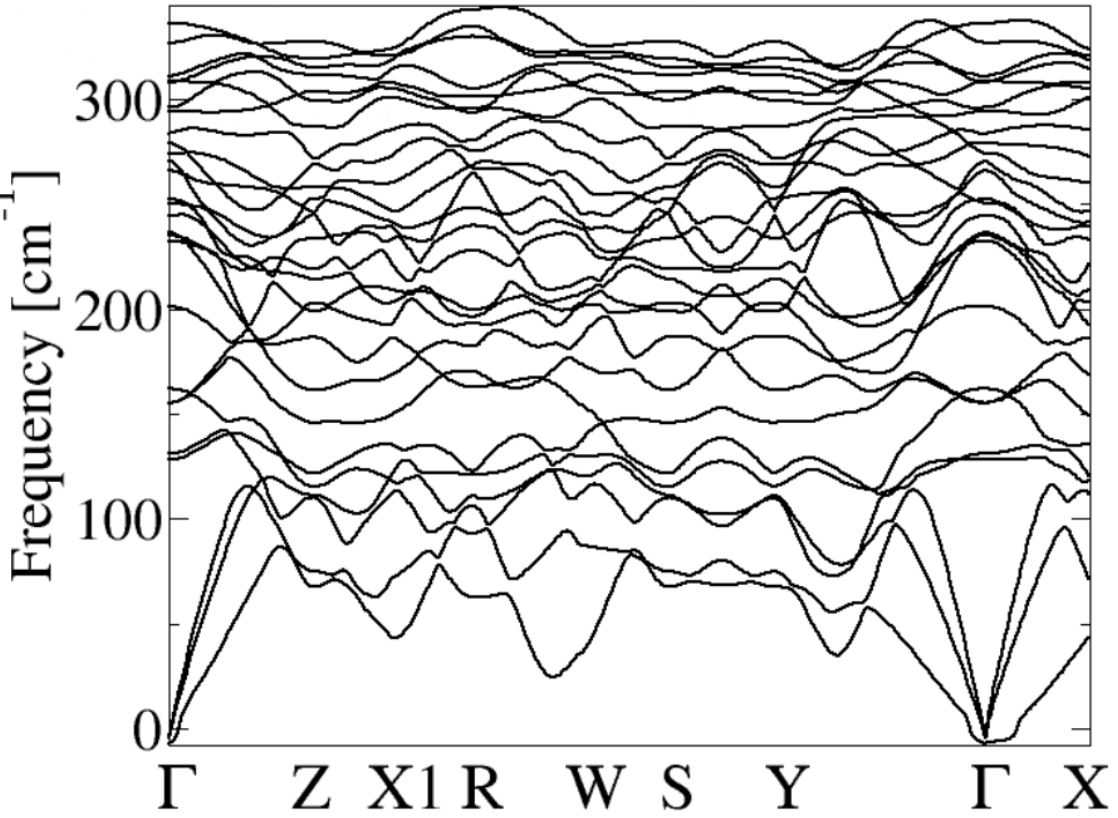

Figure B.4: Li_7Mg_2 phonon spectra along high symmetry direction in momentum space.

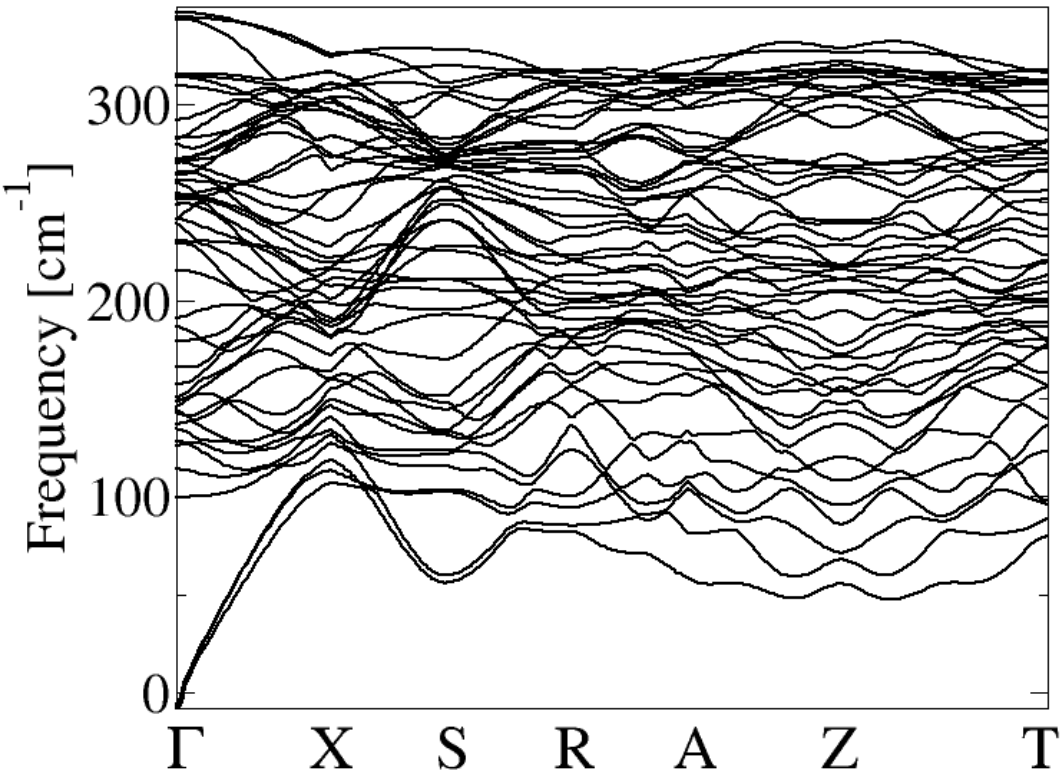

Figure B.5: $Li_{15}Mg_1$ phonon spectra along high symmetry direction in momentum space.

Bibliography

[1] *papers that cite VASP - Researchgate*. URL: https://www.researchgate.net/topic/VASP/publications (visited on 02/07/2023).

[2] *Octopus - papers citing octopus*. URL: https://octopus-code.org/new-site/10/articles/ (visited on 02/07/2023).

[3] Koichi Momma and Fujio Izumi. "*VESTA 3* for three-dimensional visualization of crystal, volumetric and morphology data". In: *Journal of Applied Crystallography* 44.6 (Dec. 2011), pp. 1272–1276. ISSN: 0021-8898. DOI: 10.1107/S0021889811038970. URL: https://scripts.iucr.org/cgi-bin/paper?S0021889811038970 (visited on 06/21/2023).

[4] G. Kresse and J. Furthmüller. "Efficient iterative schemes for *ab initio* total-energy calculations using a plane-wave basis set". en. In: *Physical Review B* 54.16 (Oct. 1996), pp. 11169–11186. ISSN: 0163-1829, 1095-3795. DOI: 10.1103/PhysRevB.54.11169. URL: https://link.aps.org/doi/10.1103/PhysRevB.54.11169 (visited on 01/31/2023).

[5] G. Kresse and D. Joubert. "From ultrasoft pseudopotentials to the projector augmented-wave method". en. In: *Physical Review B* 59.3 (Jan. 1999), pp. 1758–1775. ISSN: 0163-1829, 1095-3795. DOI: 10.1103/PhysRevB.59.1758. URL: https://link.aps.org/doi/10.1103/PhysRevB.59.1758 (visited on 02/07/2023).

[6] Nicolas Tancogne-Dejean et al. "Octopus, a computational framework for exploring light-driven phenomena and quantum dynamics in extended and finite systems". en. In: *The Journal of Chemical Physics* 152.12 (Mar. 2020),

p. 124119. ISSN: 0021-9606, 1089-7690. DOI: 10.1063/1.5142502. URL: http://aip.scitation.org/doi/10.1063/1.5142502 (visited on 01/05/2022).

[7] Xavier Andrade et al. "Real-space grids and the Octopus code as tools for the development of new simulation approaches for electronic systems". en. In: *Physical Chemistry Chemical Physics* 17.47 (2015). arXiv: 1501.05654, pp. 31371–31396. ISSN: 1463-9076, 1463-9084. DOI: 10.1039/C5CP00351B. URL: http://arxiv.org/abs/1501.05654 (visited on 12/16/2020).

[8] Alberto Castro et al. "octopus: a tool for the application of time-dependent density functional theory". en. In: *physica status solidi (b)* 243.11 (Sept. 2006), pp. 2465–2488. ISSN: 0370-1972, 1521-3951. DOI: 10.1002/pssb.200642067. URL: https://onlinelibrary.wiley.com/doi/10.1002/pssb.200642067 (visited on 01/05/2022).

[9] M Marques. "octopus: a first-principles tool for excited electron–ion dynamics". en. In: *Computer Physics Communications* 151.1 (Mar. 2003), pp. 60–78. ISSN: 00104655. DOI: 10.1016/S0010-4655(02)00686-0. URL: https://linkinghub.elsevier.com/retrieve/pii/S0010465502006860 (visited on 01/05/2022).

[10] Ivan D. Avdeev, Mikhail O. Nestoklon, and Serguei V. Goupalov. "Exciton Fine Structure in Lead Chalcogenide Quantum Dots: Valley Mixing and Crucial Role of Intervalley Electron–Hole Exchange". en. In: *Nano Letters* 20.12 (Dec. 2020), pp. 8897–8902. ISSN: 1530-6984, 1530-6992. DOI: 10.1021/acs.nanolett.0c03937. URL: https://pubs.acs.org/doi/10.1021/acs.nanolett.0c03937 (visited on 01/23/2021).

[11] J. M. An et al. "The Peculiar Electronic Structure of PbSe Quantum Dots". en. In: *Nano Letters* 6.12 (Dec. 2006), pp. 2728–2735. ISSN: 1530-6984, 1530-6992. DOI: 10.1021/nl061684x. URL: https://pubs.acs.org/doi/10.1021/nl061684x (visited on 12/27/2021).

[12] S. V. Goupalov. "Selection rules for optical transitions in PbSe nanocrystal quantum dots: Drastic effect of structure inversion asymmetry". en. In: *Physical Review B* 79.23 (June 2009), p. 233305. ISSN: 1098-0121, 1550-235X. DOI: 10.1103/PhysRevB.79.233305. URL: https://link.aps.org/doi/10.1103/PhysRevB.79.233305 (visited on 02/09/2022).

[13] Jeffrey M. Harbold and Frank W. Wise. "Photoluminescence spectroscopy of PbSe nanocrystals". en. In: *Physical Review B* 76.12 (Sept. 2007), p. 125304. ISSN: 1098-0121, 1550-235X. DOI: 10.1103/PhysRevB.76.125304. URL: https://link.aps.org/doi/10.1103/PhysRevB.76.125304 (visited on 01/23/2021).

[14] Weyde M. M. Lin et al. "Nanocrystal Quantum Dot Devices: How the Lead Sulfide (PbS) System Teaches Us the Importance of Surfaces". en. In: *CHIMIA* 75.5 (May 2021), p. 398. ISSN: 2673-2424, 0009-4293. DOI: 10.2533/chimia.2021.398. URL: https://chimia.ch/chimia/article/view/2021_398 (visited on 06/05/2023).

[15] Christopher Melnychuk and Philippe Guyot-Sionnest. "Multicarrier Dynamics in Quantum Dots". en. In: *Chemical Reviews* 121.4 (Feb. 2021), pp. 2325–2372. ISSN: 0009-2665, 1520-6890. DOI: 10.1021/acs.chemrev.0c00931. URL: https://pubs.acs.org/doi/10.1021/acs.chemrev.0c00931 (visited on 03/01/2022).

[16] Walter Kohn. *kohn-lecture.pdf*. 1998. URL: https://www.nobelprize.org/uploads/2018/06/kohn-lecture.pdf (visited on 02/07/2023).

[17] Klaus Capelle. *A bird's-eye view of density-functional theory*. en. arXiv:cond-mat/0211443. Nov. 2006. URL: http://arxiv.org/abs/cond-mat/0211443 (visited on 01/09/2023).

[18] Steven H. Simon. *The Oxford Solid State Basics*. eng. First edition. Oxford: OUP Oxford, Jan. 2013. ISBN: 978-0-19-968076-4.

[19] Mois I. Aroyo, ed. *International tables for crystallography. A: Space-group symmetry / edited by Mois I. Aroyo*. eng. 6. ed. ISSN: 1574-8707. Chichester: Wiley, 2016. ISBN: 978-0-470-97423-0.

[20] Felix Bloch. "Uber die Quantenmechanik der Elektronen in Kristallgittern". German. Uber die Quantenmechanik der Elektronen in Kristallgittern, Zeits. f. Physik 52.7-8 555-600. (1928). PhD. Universitat Leipzig, 1928.

[21] *Fourier Transform – from Wolfram MathWorld*. URL: https://mathworld.wolfram.com/FourierTransform.html (visited on 02/07/2023).

[22] Giuliano Carchini et al. "How Theoretical Simulations Can Address the Structure and Activity of Nanoparticles". en. In: *Topics in Catalysis* 56.13-14 (Sept. 2013), pp. 1262–1272. ISSN: 1022-5528, 1572-9028. DOI: 10.1007/s11244-013-0093-3. URL: http://link.springer.com/10.1007/s11244-013-0093-3 (visited on 05/16/2021).

[23] John P. Perdew et al. "Prescription for the design and selection of density functional approximations: More constraint satisfaction with fewer fits". en. In: *The Journal of Chemical Physics* 123.6 (Aug. 2005), p. 062201. ISSN: 0021-9606, 1089-7690. DOI: 10.1063/1.1904565. URL: http://aip.scitation.org/doi/10.1063/1.1904565 (visited on 02/07/2023).

[24] Kerstin Hummer, Andreas Grüneis, and Georg Kresse. "Structural and electronic properties of lead chalcogenides from first principles". en. In: *Physical Review B* 75.19 (May 2007), p. 195211. ISSN: 1098-0121, 1550-235X. DOI: 10.1103/PhysRevB.75.195211. URL: https://link.aps.org/doi/10.1103/PhysRevB.75.195211 (visited on 12/16/2021).

[25] A. Svane et al. "Quasiparticle self-consistent GW calculations for PbS, PbSe, and PbTe: Band structure and pressure coefficients". en. In: *Physical Review B* 81.24 (June 2010), p. 245120. ISSN: 1098-0121, 1550-235X. DOI: 10.1103/PhysRevB.81.245120. URL: https://link.aps.org/doi/10.1103/PhysRevB.81.245120 (visited on 12/16/2021).

[26] Aoife R. Murphy et al. "Acoustic deformation potentials of n -type PbTe from first principles". en. In: *Physical Review B* 98.8 (Aug. 2018), p. 085201. ISSN: 2469-9950, 2469-9969. DOI: 10.1103/PhysRevB.98.085201. URL: https://link.aps.org/doi/10.1103/PhysRevB.98.085201 (visited on 12/16/2021).

[27] M. C. Payne et al. "Iterative minimization techniques for *ab initio* total-energy calculations: molecular dynamics and conjugate gradients". en. In: *Reviews of Modern Physics* 64.4 (Oct. 1992), pp. 1045–1097. ISSN: 0034-6861, 1539-0756. DOI: 10.1103/RevModPhys.64.1045. URL: https://link.aps.org/doi/10.1103/RevModPhys.64.1045 (visited on 01/09/2023).

[28] *The VASP Manual - Vaspwiki*. URL: https://www.vasp.at/wiki/index.php/The_VASP_Manual (visited on 01/31/2023).

[29] C. Hartwigsen, S. Goedecker, and J. Hutter. "Relativistic separable dual-space Gaussian pseudopotentials from H to Rn". en. In: *Physical Review B* 58.7 (Aug. 1998), pp. 3641–3662. ISSN: 0163-1829, 1095-3795. DOI: 10.1103/PhysRevB.58.3641. URL: https://link.aps.org/doi/10.1103/PhysRevB.58.3641 (visited on 03/16/2021).

[30] Roland Winkler. *Spin-orbit coupling effects in two-dimensional electron and hole systems*. en. Springer tracts in modern physics v. 191. Berlin ; New York: Springer, 2003. ISBN: 978-3-540-01187-3.

[31] Nouredine Zettili. "Quantum mechanics : concepts and applications / Nouredine Zettili." eng. In: (Jan. 2009). Edition: 2nd ed. Publisher: Wiley. ISSN: 9780470026786.

[32] L. H. Thomas. "The Motion of the Spinning Electron". en. In: *Nature* 117.2945 (Apr. 1926), pp. 514–514. ISSN: 0028-0836, 1476-4687. DOI: 10.1038/117514a0. URL: https://www.nature.com/articles/117514a0 (visited on 02/07/2023).

[33] Frank W. Wise. "Lead Salt Quantum Dots: the Limit of Strong Quantum Confinement". en. In: *Accounts of Chemical Research* 33.11 (Nov. 2000),

pp. 773–780. ISSN: 0001-4842, 1520-4898. DOI: 10.1021/ar970220q. URL: https://pubs.acs.org/doi/10.1021/ar970220q (visited on 12/16/2020).

[34] Inuk Kang and Frank W. Wise. "Electronic structure and optical properties of PbS and PbSe quantum dots". en. In: *Journal of the Optical Society of America B* 14.7 (July 1997), p. 1632. ISSN: 0740-3224, 1520-8540. DOI: 10.1364/JOSAB.14.001632. URL: https://www.osapublishing.org/abstract.cfm?URI=josab-14-7-1632 (visited on 01/23/2021).

[35] John P. Perdew. "Density functional theory and the band gap problem". en. In: *International Journal of Quantum Chemistry* 28.S19 (June 2009), pp. 497–523. ISSN: 00207608, 1097461X. DOI: 10.1002/qua.560280846. URL: https://onlinelibrary.wiley.com/doi/10.1002/qua.560280846 (visited on 12/16/2021).

[36] M. Thambidurai et al. "High performance infrared photodetectors up to 28 µm wavelength based on lead selenide colloidal quantum dots". en. In: *Optical Materials Express* 7.7 (July 2017), p. 2326. ISSN: 2159-3930. DOI: 10.1364/OME.7.002326. URL: https://www.osapublishing.org/abstract.cfm?URI=ome-7-7-2326 (visited on 12/16/2020).

[37] Long Hu et al. "Enhanced mobility in PbS quantum dot films *via* PbSe quantum dot mixing for optoelectronic applications". en. In: *Journal of Materials Chemistry C* 7.15 (2019), pp. 4497–4502. ISSN: 2050-7526, 2050-7534. DOI: 10.1039/C8TC06495D. URL: http://xlink.rsc.org/?DOI=C8TC06495D (visited on 12/16/2020).

[38] Maximilian Amsler. "Crystal Structure Prediction Based on Density Functional Theory". PhD thesis. University of Basel, 2014. URL: https://edoc.unibas.ch/33436/1/main.pdf (visited on 02/07/2023).

[39] Maximilian Amsler and Stefan Goedecker. "Crystal structure prediction using the minima hopping method". en. In: *The Journal of Chemical Physics* 133.22 (Dec. 2010), p. 224104. ISSN: 0021-9606, 1089-7690. DOI: 10.1063/

1.3512900. URL: http://aip.scitation.org/doi/10.1063/1.3512900 (visited on 01/31/2023).

[40] A. Martín Pendás, E. Francisco, and M.A. Blanco. "Electron–electron interactions between ELF basins". en. In: *Chemical Physics Letters* 454.4-6 (Mar. 2008), pp. 396–403. ISSN: 00092614. DOI: 10.1016/j.cplett.2008.02.029. URL: https://linkinghub.elsevier.com/retrieve/pii/S0009261408002017 (visited on 07/18/2022).

[41] B. Silvi and A. Savin. "Classification of chemical bonds based on topological analysis of electron localization functions". en. In: *Nature* 371.6499 (Oct. 1994), pp. 683–686. ISSN: 0028-0836, 1476-4687. DOI: 10.1038/371683a0. URL: http://www.nature.com/articles/371683a0 (visited on 06/30/2022).

[42] Jean-Yves Raty et al. "How to Identify Lone Pairs, Van der Waals Gaps, and Metavalent Bonding Using Charge and Pair Density Methods: From Elemental Chalcogens to Lead Chalcogenides and Phase-Change Materials". en. In: *physica status solidi (RRL) – Rapid Research Letters* 15.11 (Nov. 2021), p. 2000534. ISSN: 1862-6254, 1862-6270. DOI: 10.1002/pssr.202000534. URL: https://onlinelibrary.wiley.com/doi/10.1002/pssr.202000534 (visited on 10/08/2022).

[43] Konstantinos Koumpouras and J Andreas Larsson. "Distinguishing between chemical bonding and physical binding using electron localization function (ELF)". en. In: *Journal of Physics: Condensed Matter* 32.31 (July 2020), p. 315502. ISSN: 0953-8984, 1361-648X. DOI: 10.1088/1361-648X/ab7fd8. URL: https://iopscience.iop.org/article/10.1088/1361-648X/ab7fd8 (visited on 06/09/2022).

[44] Z. Yang et al. "Review on Research and Development of Magnesium Alloys". In: *Acta Metallurgica Sinica (English Letters)* 21.5 (2008), pp. 313–328. ISSN: 1006-7191. DOI: https://doi.org/10.1016/S1006-7191(08)

60054-X. URL: https://www.sciencedirect.com/science/article/pii/S100671910860054X.

[45] J. Trivisonno and Charles S. Smith. "Elastic constants of lithium-magnesium alloys". In: *Acta Metallurgica* 9.12 (1961), pp. 1064–1071. ISSN: 0001-6160. DOI: https://doi.org/10.1016/0001-6160(61)90175-4. URL: https://www.sciencedirect.com/science/article/pii/0001616061901754.

[46] M. J. Phasha et al. "Link between structural and mechanical stability of fcc- and bcc-based ordered Mg–Li alloys". In: *Intermetallics* 18.11 (2010), pp. 2083–2089. ISSN: 0966-9795. DOI: https://doi.org/10.1016/j.intermet.2010.06.015. URL: https://www.sciencedirect.com/science/article/pii/S0966979510002736.

[47] Ilgyou Shin and Emily A. Carter. "First-principles simulations of plasticity in body-centered-cubic magnesium–lithium alloys". In: *Acta Materialia* 64 (2014), pp. 198–207. ISSN: 1359-6454. DOI: https://doi.org/10.1016/j.actamat.2013.10.030. URL: https://www.sciencedirect.com/science/article/pii/S1359645413007933.

[48] B. R. Sahu. "Electronic structure and bonding of ultralight LiMg". In: *Materials Science and Engineering: B* 49.1 (1997), pp. 74–78. ISSN: 0921-5107. DOI: https://doi.org/10.1016/S0921-5107(97)00068-8. URL: https://www.sciencedirect.com/science/article/pii/S0921510797000688.

[49] B. L. Mordike and T. Ebert. "Magnesium: Properties — applications — potential". In: *Materials Science and Engineering: A* 302.1 (2001), pp. 37–45. ISSN: 0921-5093. DOI: https://doi.org/10.1016/S0921-5093(00)01351-4. URL: https://www.sciencedirect.com/science/article/pii/S0921509300013514.

[50] Gerald S. Cole. "Issues that Influence Magnesium's Use in the Automotive Industry". In: *Materials Science Forum* 419-422 (Mar. 2003), pp. 43–50. ISSN:

1662-9752. DOI: 10.4028/www.scientific.net/MSF.419-422.43. URL: https://www.scientific.net/MSF.419-422.43 (visited on 01/29/2023).

[51] E. Aghion, B. Bronfin, and D. Eliezer. "The role of the magnesium industry in protecting the environment". In: *Journal of Materials Processing Technology* 117.3 (2001), pp. 381–385. ISSN: 0924-0136. DOI: https://doi.org/10.1016/S0924-0136(01)00779-8. URL: https://www.sciencedirect.com/science/article/pii/S0924013601007798.

[52] *Magnesium | Description, Properties, & Compounds | Britannica*. en. Jan. 2023. URL: https://www.britannica.com/science/magnesium (visited on 01/31/2023).

[53] R. Hull and Bacon. *Introduction to Dislocations*. en. Elsevier, 2011. ISBN: 978-0-08-096672-4. DOI: 10.1016/C2009-0-64358-0. URL: https://linkinghub.elsevier.com/retrieve/pii/C20090643580 (visited on 01/29/2023).

[54] A Luque, M Ghazisaeidi, and W A Curtin. "Deformation modes in magnesium (0 0 0 1) and $(0\,,1\,,\bar{1}\,,1)$ single crystals: simulations versus experiments". In: *Modelling and Simulation in Materials Science and Engineering* 21.4 (June 2013), p. 045010. ISSN: 0965-0393, 1361-651X. DOI: 10.1088/0965-0393/21/4/045010. URL: https://iopscience.iop.org/article/10.1088/0965-0393/21/4/045010 (visited on 01/29/2023).

[55] J. F. Nye. *Physical Properties of Crystals: Their Representation by Tensors and Matrices*. Oxford, New York: Oxford University Press, July 1985. ISBN: 978-0-19-851165-6.

[56] Zhaoxuan Wu and W. A. Curtin. "The origins of high hardening and low ductility in magnesium". en. In: *Nature* 526.7571 (Oct. 2015), pp. 62–67. ISSN: 0028-0836, 1476-4687. DOI: 10.1038/nature15364. URL: http://www.nature.com/articles/nature15364 (visited on 01/29/2023).

[57] Feng Kang et al. "The activation of ⟨c + a⟩ non-basal slip in Magnesium alloys". en. In: *Journal of Materials Science* 47.22 (Nov. 2012), pp. 7854–7859. ISSN: 0022-2461, 1573-4803. DOI: 10.1007/s10853-012-6344-z. URL: http://link.springer.com/10.1007/s10853-012-6344-z (visited on 01/29/2023).

[58] J. Geng et al. "The structure of ⟨ $c + a$ ⟩ type dislocation loops in magnesium". en. In: *Philosophical Magazine Letters* 94.6 (June 2014), pp. 377–386. ISSN: 0950-0839, 1362-3036. DOI: 10.1080/09500839.2014.916423. URL: http://www.tandfonline.com/doi/abs/10.1080/09500839.2014.916423 (visited on 01/29/2023).

[59] S. Sandlöbes et al. "Ductility improvement of Mg alloys by solid solution: Ab initio modeling, synthesis and mechanical properties". In: *Acta Materialia* 70 (2014), pp. 92–104. ISSN: 1359-6454. DOI: https://doi.org/10.1016/j.actamat.2014.02.011. URL: https://www.sciencedirect.com/science/article/pii/S1359645414000949.

[60] Kuiying Chen and Kevin P. Boyle. "Elastic Properties, Thermal Expansion Coefficients, and Electronic Structures of Mg and Mg-Based Alloys". en. In: *Metallurgical and Materials Transactions A* 40.11 (Nov. 2009), pp. 2751–2760. ISSN: 1073-5623, 1543-1940. DOI: 10.1007/s11661-009-9954-6. URL: http://link.springer.com/10.1007/s11661-009-9954-6 (visited on 01/29/2023).

[61] F. Wang et al. "In situ observation of collective grain-scale mechanics in Mg and Mg–rare earth alloys". In: *Acta Materialia* 80 (2014), pp. 77–93. ISSN: 1359-6454. DOI: https://doi.org/10.1016/j.actamat.2014.07.048. URL: https://www.sciencedirect.com/science/article/pii/S1359645414005667.

[62] Zongrui Pei et al. "Rapid theory-guided prototyping of ductile Mg alloys: from binary to multi-component materials". In: *New Journal of Physics* 17.9 (Sept.

2015), p. 093009. ISSN: 1367-2630. DOI: 10.1088/1367-2630/17/9/093009. URL: https://iopscience.iop.org/article/10.1088/1367-2630/17/9/093009 (visited on 01/29/2023).

[63] William Art Counts et al. "Using Ab Initio Calculations in Designing bcc MgLi-X Alloys for Ultra-Lightweight Applications". en. In: *Advanced Engineering Materials* 12.12 (Dec. 2010), pp. 1198–1205. ISSN: 14381656. DOI: 10.1002/adem.201000225. URL: https://onlinelibrary.wiley.com/doi/10.1002/adem.201000225 (visited on 01/29/2023).

[64] Anubhav Jain et al. "Commentary: The Materials Project: A materials genome approach to accelerating materials innovation". en. In: *APL Materials* 1.1 (July 2013), p. 011002. ISSN: 2166-532X. DOI: 10.1063/1.4812323. URL: http://aip.scitation.org/doi/10.1063/1.4812323 (visited on 01/31/2023).

[65] Charles S. Barrett. "A Low Temperature Transformation in Lithium". In: *Physical Review* 72.3 (Aug. 1947). Publisher: American Physical Society, pp. 245–245. DOI: 10.1103/PhysRev.72.245. URL: https://link.aps.org/doi/10.1103/PhysRev.72.245 (visited on 01/29/2023).

[66] Martin H. Sadd. *Elasticity : Theory, Applications, and Numerics*. eng. 2nd ed. Amsterdam: Academic Press, Jan. 2009. ISBN: 978-0-12-374446-3.

[67] S.F. Pugh. "XCII. Relations between the elastic moduli and the plastic properties of polycrystalline pure metals". en. In: *The London, Edinburgh, and Dublin Philosophical Magazine and Journal of Science* 45.367 (Aug. 1954), pp. 823–843. ISSN: 1941-5982, 1941-5990. DOI: 10.1080/14786440808520496. URL: http://www.tandfonline.com/doi/abs/10.1080/14786440808520496 (visited on 01/30/2023).

[68] Olivia Pavlic et al. "Design of Mg alloys: The effects of Li concentration on the structure and elastic properties in the Mg-Li binary system by first principles calculations". en. In: *Journal of Alloys and Compounds* 691 (Jan. 2017),

pp. 15–25. ISSN: 09258388. DOI: 10.1016/j.jallcom.2016.08.217. URL: https://linkinghub.elsevier.com/retrieve/pii/S0925838816326159 (visited on 06/07/2023).

[69] Tokuteru Uesugi et al. "<I>Ab Initio</I> Calculation on the Structure and Elastic Properties of a Magnesium-Lithium Alloy". en. In: *MATERIALS TRANSACTIONS* 42.7 (2001), pp. 1167–1171. ISSN: 1345-9678, 1347-5320. DOI: 10.2320/matertrans.42.1167. URL: https://www.jstage.jst.go.jp/article/matertrans/42/7/42_7_1167/_article (visited on 02/08/2023).

[70] Richard H. Taylor, Stefano Curtarolo, and Gus L. W. Hart. "Ordered magnesium-lithium alloys: First-principles predictions". en. In: *Physical Review B* 81.2 (Jan. 2010), p. 024112. ISSN: 1098-0121, 1550-235X. DOI: 10.1103/PhysRevB.81.024112. URL: https://link.aps.org/doi/10.1103/PhysRevB.81.024112 (visited on 01/31/2023).

[71] Chao Ping Liang and Hao Ran Gong. "Phase stability, mechanical property, and electronic structure of Mg–Li system". In: *Journal of Alloys and Compounds* 489.1 (Jan. 2010), pp. 130–135. ISSN: 0925-8388. DOI: 10.1016/j.jallcom.2009.09.032. URL: https://www.sciencedirect.com/science/article/pii/S0925838809017769.

[72] M.J. Phasha and P.E. Ngoepe. "An alternative DFT-based model for calculating structural and elastic properties of random binary HCP, FCC and BCC alloys: Mg–Li system as test case". en. In: *Intermetallics* 21.1 (Feb. 2012), pp. 88–96. ISSN: 09669795. DOI: 10.1016/j.intermet.2011.09.015. URL: https://linkinghub.elsevier.com/retrieve/pii/S0966979511003165 (visited on 02/08/2023).

[73] Shyue Ping Ong et al. "LiFePO $_2$ Phase Diagram from First Principles Calculations". en. In: *Chemistry of Materials* 20.5 (Mar. 2008), pp. 1798–1807.

ISSN: 0897-4756, 1520-5002. DOI: 10.1021/cm702327g. URL: https://pubs.acs.org/doi/10.1021/cm702327g (visited on 01/31/2023).

[74] Anubhav Jain et al. "Formation enthalpies by mixing GGA and GGA + U calculations". en. In: *Physical Review B* 84.4 (July 2011), p. 045115. ISSN: 1098-0121, 1550-235X. DOI: 10.1103/PhysRevB.84.045115. URL: https://link.aps.org/doi/10.1103/PhysRevB.84.045115 (visited on 01/31/2023).

[75] Stefano Curtarolo et al. "AFLOW: An automatic framework for high-throughput materials discovery". en. In: *Computational Materials Science* 58 (June 2012), pp. 218–226. ISSN: 09270256. DOI: 10.1016/j.commatsci.2012.02.005. URL: https://linkinghub.elsevier.com/retrieve/pii/S0927025612000717 (visited on 01/31/2023).

[76] James E. Saal et al. "Materials Design and Discovery with High-Throughput Density Functional Theory: The Open Quantum Materials Database (OQMD)". en. In: *JOM* 65.11 (Nov. 2013), pp. 1501–1509. ISSN: 1047-4838, 1543-1851. DOI: 10.1007/s11837-013-0755-4. URL: http://link.springer.com/10.1007/s11837-013-0755-4 (visited on 01/31/2023).

[77] Félix Mouhat and François-Xavier Coudert. "Necessary and sufficient elastic stability conditions in various crystal systems". en. In: *Physical Review B* 90.22 (Dec. 2014), p. 224104. ISSN: 1098-0121, 1550-235X. DOI: 10.1103/PhysRevB.90.224104. URL: https://link.aps.org/doi/10.1103/PhysRevB.90.224104 (visited on 01/09/2023).

[78] Ahmed Rassem Wazzan and Lawrence Baylor Robinson. "Elastic Constants of Magnesium-Lithium Alloys". en. In: *Physical Review* 155.3 (Mar. 1967), pp. 586–594. ISSN: 0031-899X. DOI: 10.1103/PhysRev.155.586. URL: https://link.aps.org/doi/10.1103/PhysRev.155.586 (visited on 01/31/2023).

[79] F.H. Herbstein and B.L. Averbach. "The structure of lithium-magnesium solid solutions—I". en. In: *Acta Metallurgica* 4.4 (July 1956), pp. 407–413. ISSN: 00016160. DOI: 10.1016/0001-6160(56)90031-1. URL: https://

linkinghub.elsevier.com/retrieve/pii/0001616056900311 (visited on 01/31/2023).

[80] D.W. Levinson. "On the lattice parameter of Mg-Li alloys". en. In: *Acta Metallurgica* 3.3 (May 1955), pp. 294–295. ISSN: 00016160. DOI: 10.1016/0001-6160(55)90069-9. URL: https://linkinghub.elsevier.com/retrieve/pii/0001616055900699 (visited on 01/31/2023).

[81] William Art Counts et al. "Ab Initio Guided Design of bcc Ternary Mg-Li-X (X = Ca, Al, Si, Zn, Cu) Alloys for Ultra-Lightweight Applications". en. In: *Advanced Engineering Materials* 12.7 (May 2010), pp. 572–576. ISSN: 14381656. DOI: 10.1002/adem.200900308. URL: https://onlinelibrary.wiley.com/doi/10.1002/adem.200900308 (visited on 01/29/2023).

[82] Manfred Hayk. *What is the Thermal Infrared Range? And What are NIR, SWIR, MWIR and LWIR?* June 2021. URL: https://www.ametek-land.com/pressreleases/blog/2021/june/thermalinfraredrangeblog (visited on 01/31/2023).

[83] Richard Dalven. *Electronic Structure of PbS, PbSe, and PbTe*. 1974.

[84] Hans Zogg. "Photovoltaic lead-chalcogenide on silicon infrared sensor arrays". en. In: *Optical Engineering* 33.5 (May 1994), p. 1440. ISSN: 0091-3286. DOI: 10.1117/12.165808. URL: http://opticalengineering.spiedigitallibrary.org/article.aspx?doi=10.1117/12.165808 (visited on 02/13/2023).

[85] A. Rogalski and W. Kaszuba. "PbS1-x,Sex, (Ox 1) photovoltaic detectors: carrier lifetimes and resistance-area product". In: *Infrared Physics* 23.1 (Jan. 1983), pp. 23–32. ISSN: 0020-0891. DOI: 10.1016/0020-0891(83)90062-3. URL: https://www.sciencedirect.com/science/article/pii/0020089183900623.

[86] Tapas K. Chaudhuri. "A solar thermophotovoltaic converter using Pbs photovoltaic cells". en. In: *International Journal of Energy Research* 16.6 (Aug.

1992), pp. 481–487. ISSN: 0363907X, 1099114X. DOI: 10.1002/er.4440160605. URL: https://onlinelibrary.wiley.com/doi/10.1002/er.4440160605 (visited on 02/13/2023).

[87] Shihab Bin Hafiz et al. "Colloidal quantum dots for thermal infrared sensing and imaging". en. In: *Nano Convergence* 6.1 (Dec. 2019), p. 7. ISSN: 2196-5404. DOI: 10.1186/s40580-019-0178-1. URL: https://nanoconvergencejournal.springeropen.com/articles/10.1186/s40580-019-0178-1 (visited on 12/21/2020).

[88] Madison K. Brod, Michael Y. Toriyama, and G. Jeffrey Snyder. "Orbital Chemistry That Leads to High Valley Degeneracy in PbTe". en. In: *Chemistry of Materials* 32.22 (Nov. 2020), pp. 9771–9779. ISSN: 0897-4756, 1520-5002. DOI: 10.1021/acs.chemmater.0c03740. URL: https://pubs.acs.org/doi/10.1021/acs.chemmater.0c03740 (visited on 01/08/2021).

[89] Su-Huai Wei and Alex Zunger. "Electronic and structural anomalies in lead chalcogenides". en. In: *Physical Review B* 55.20 (May 1997), pp. 13605–13610. ISSN: 0163-1829, 1095-3795. DOI: 10.1103/PhysRevB.55.13605. URL: https://link.aps.org/doi/10.1103/PhysRevB.55.13605 (visited on 07/30/2021).

[90] Xie Zhang, Jimmy-Xuan Shen, and Chris G. Van de Walle. "Anomalous Auger Recombination in PbSe". en. In: *Physical Review Letters* 125.3 (July 2020), p. 037401. ISSN: 0031-9007, 1079-7114. DOI: 10.1103/PhysRevLett.125.037401. URL: https://link.aps.org/doi/10.1103/PhysRevLett.125.037401 (visited on 01/08/2021).

[91] Min Zhu et al. "Unique Bond Breaking in Crystalline Phase Change Materials and the Quest for Metavalent Bonding". en. In: *Advanced Materials* 30.18 (May 2018), p. 1706735. ISSN: 09359648. DOI: 10.1002/adma.201706735. URL: https://onlinelibrary.wiley.com/doi/10.1002/adma.201706735 (visited on 05/10/2022).

[92] Matthias Wuttig et al. "Incipient Metals: Functional Materials with a Unique Bonding Mechanism". en. In: *Advanced Materials* 30.51 (Dec. 2018), p. 1803777. ISSN: 09359648. DOI: 10.1002/adma.201803777. URL: https://onlinelibrary.wiley.com/doi/10.1002/adma.201803777 (visited on 05/10/2022).

[93] Stefan Maier et al. "Discovering Electron-Transfer-Driven Changes in Chemical Bonding in Lead Chalcogenides (PbX, where X = Te, Se, S, O)". en. In: *Advanced Materials* 32.49 (Dec. 2020), p. 2005533. ISSN: 0935-9648, 1521-4095. DOI: 10.1002/adma.202005533. URL: https://onlinelibrary.wiley.com/doi/10.1002/adma.202005533 (visited on 05/10/2022).

[94] Ludovica Guarneri et al. "Metavalent Bonding in Crystalline Solids: How Does It Collapse?" en. In: *Advanced Materials* 33.39 (Oct. 2021), p. 2102356. ISSN: 0935-9648, 1521-4095. DOI: 10.1002/adma.202102356. URL: https://onlinelibrary.wiley.com/doi/10.1002/adma.202102356 (visited on 05/10/2022).

[95] Gerasimos Konstantatos et al. "Hybrid graphene–quantum dot phototransistors with ultrahigh gain". en. In: *Nature Nanotechnology* 7.6 (June 2012), pp. 363–368. ISSN: 1748-3387, 1748-3395. DOI: 10.1038/nnano.2012.60. URL: http://www.nature.com/articles/nnano.2012.60 (visited on 12/16/2020).

[96] Gerasimos Konstantatos and Edward H. Sargent. "Solution-Processed Quantum Dot Photodetectors". en. In: *Proceedings of the IEEE* 97.10 (Oct. 2009), pp. 1666–1683. ISSN: 0018-9219. DOI: 10.1109/JPROC.2009.2025612. URL: http://ieeexplore.ieee.org/document/5247124/ (visited on 12/21/2020).

[97] Judy Z. Wu. "Explore uncooled quantum dots/graphene nanohybrid infrared detectors based on quantum dots/graphene heterostructures". en. In: *Infrared Technology and Applications XLVI*. Ed. by Gabor F. Fulop et al. Online Only, United States: SPIE, Apr. 2020, p. 7. ISBN: 978-1-5106-3591-3 978-1-5106-3592-0. DOI: 10.1117/12.2556930. URL: https://www.

spiedigitallibrary.org/conference-proceedings-of-spie/11407/2556930/Explore-uncooled-quantum-dots-graphene-nanohybrid-infrared-detectors-based-on/10.1117/12.2556930.full (visited on 12/21/2020).

[98] Yun Liu, Nolan Peard, and Jeffrey C. Grossman. "Bandlike Transport in PbS Quantum Dot Superlattices with Quantum Confinement". en. In: *The Journal of Physical Chemistry Letters* 10.13 (July 2019), pp. 3756–3762. ISSN: 1948-7185, 1948-7185. DOI: 10.1021/acs.jpclett.9b01282. URL: https://pubs.acs.org/doi/10.1021/acs.jpclett.9b01282 (visited on 08/28/2021).

[99] Agnieszka Gocalińska et al. "Size-Dependent Electron Transfer from Colloidal PbS Nanocrystals to Fullerene". en. In: *The Journal of Physical Chemistry Letters* 1.7 (Apr. 2010), pp. 1149–1154. ISSN: 1948-7185, 1948-7185. DOI: 10.1021/jz100116t. URL: https://pubs.acs.org/doi/10.1021/jz100116t (visited on 07/30/2021).

[100] William Clodius. "Multi-spectral band selection for satellite-based systems". In: Orlando, Fl: SPIE, Apr. 1998. URL: https://www.osti.gov/servlets/purl/674570 (visited on 12/08/2021).

[101] E. L. Dereniak. *Infrared Detectors and Systems | Wiley*. URL: https://www.wiley.com/en-us/Infrared+Detectors+and+Systems-p-9780471122098 (visited on 02/01/2023).

[102] R. Clark Jones. "A Method of Describing the Detectivity of Photoconductive Cells". en. In: *Review of Scientific Instruments* 24.11 (Nov. 1953), pp. 1035–1040. ISSN: 0034-6748, 1089-7623. DOI: 10.1063/1.1770585. URL: http://aip.scitation.org/doi/10.1063/1.1770585 (visited on 10/26/2021).

[103] Maral Vafaie et al. "Colloidal quantum dot photodetectors with 10-ns response time and 80% quantum efficiency at 1,550 nm". en. In: *Matter* 4.3 (Mar. 2021), pp. 1042–1053. ISSN: 25902385. DOI: 10.1016/j.matt.2020.

12.017. URL: https://linkinghub.elsevier.com/retrieve/pii/S259023852030686X (visited on 02/17/2023).

[104] Brent Cook et al. "Inkjet Printing Multicolor Pixelated Quantum Dots on Graphene for Broadband Photodetection". en. In: *ACS Applied Nano Materials* 2.5 (May 2019), pp. 3246–3252. ISSN: 2574-0970, 2574-0970. DOI: 10.1021/acsanm.9b00539. URL: https://pubs.acs.org/doi/10.1021/acsanm.9b00539 (visited on 02/17/2023).

[105] Antoni Rogalski, Piotr Marcin Martyniuk, and Malgorzata Kopytko. "Type-II superlattice photodetectors versus HgCdTe photodiodes". en. In: *Sensors, Systems, and Next-Generation Satellites XXIII*. Ed. by Steven P. Neeck, Toshiyoshi Kimura, and Philippe Martimort. Strasbourg, France: SPIE, Oct. 2019, p. 40. ISBN: 978-1-5106-3005-5 978-1-5106-3006-2. DOI: 10.1117/12.2538538. URL: https://www.spiedigitallibrary.org/conference-proceedings-of-spie/11151/2538538/Type-II-superlattice-photodetectors-versus-HgCdTe-photodiodes/10.1117/12.2538538.full (visited on 02/22/2023).

[106] Michael A. Kinch. *State-of-the-art infrared detector technology*. en. Bellingham, Washington, USA: SPIE Press, 2014. ISBN: 978-1-62841-289-5.

[107] Mao-Kun Zhang et al. "Graphene/Quantum Dot Heterostructure Photodetectors: From Material to Performance". en. In: *Advanced Optical Materials* 10.24 (Dec. 2022), p. 2201889. ISSN: 2195-1071, 2195-1071. DOI: 10.1002/adom.202201889. URL: https://onlinelibrary.wiley.com/doi/10.1002/adom.202201889 (visited on 02/17/2023).

[108] Yu. I. Ravich, B. A. Efimova, and V. I. Tamarchenko. "Scattering of Current Carriers and Transport Phenomena in Lead Chalcogenides II. Experiment". en. In: *Physica Status Solidi (b)* 43.2 (Feb. 1971), pp. 453–469. ISSN: 03701972, 15213951. DOI: 10.1002/pssb.2220430202. URL: https://

onlinelibrary.wiley.com/doi/10.1002/pssb.2220430202 (visited on 10/10/2021).

[109] Yu. I. Ravich, B. A. Efimova, and V. I. Tamarchenko. "Scattering of Current Carriers and Transport Phenomena in Lead Chalcogenides". en. In: *Physica Status Solidi (b)* 43.1 (Jan. 1971), pp. 11–33. ISSN: 03701972, 15213951. DOI: 10.1002/pssb.2220430102. URL: https://onlinelibrary.wiley.com/doi/10.1002/pssb.2220430102 (visited on 10/10/2021).

[110] Matteo Cagnoni, Daniel Führen, and Matthias Wuttig. "Thermoelectric Performance of IV-VI Compounds with Octahedral-Like Coordination: A Chemical-Bonding Perspective". en. In: *Advanced Materials* 30.33 (Aug. 2018), p. 1801787. ISSN: 09359648. DOI: 10.1002/adma.201801787. URL: https://onlinelibrary.wiley.com/doi/10.1002/adma.201801787 (visited on 05/10/2022).

[111] Jean-Yves Raty et al. "A Quantum-Mechanical Map for Bonding and Properties in Solids". en. In: *Advanced Materials* 31.3 (Jan. 2019), p. 1806280. ISSN: 0935-9648, 1521-4095. DOI: 10.1002/adma.201806280. URL: https://onlinelibrary.wiley.com/doi/10.1002/adma.201806280 (visited on 05/10/2022).

[112] Alexander L. Efros and Louis E. Brus. "Nanocrystal Quantum Dots: From Discovery to Modern Development". en. In: *ACS Nano* 15.4 (Apr. 2021), pp. 6192–6210. ISSN: 1936-0851, 1936-086X. DOI: 10.1021/acsnano.1c01399. URL: https://pubs.acs.org/doi/10.1021/acsnano.1c01399 (visited on 09/20/2022).

[113] A. Efros and A. Efros. "Interband absorption of light in a semiconductor sphere". In: *Soviet physics: Semiconductors* (1982). URL: https://www.semanticscholar.org/paper/Interband-absorption-of-light-in-a-semiconductor-Efros-Efros/f9c15cd95fca148d0c0488fd0fe45476725e1cfa (visited on 02/01/2023).

[114] S. Schmitt-Rink, D. A. B. Miller, and D. S. Chemla. "Theory of the linear and nonlinear optical properties of semiconductor microcrystallites". en. In: *Physical Review B* 35.15 (May 1987), pp. 8113–8125. ISSN: 0163-1829. DOI: 10.1103/PhysRevB.35.8113. URL: https://link.aps.org/doi/10.1103/PhysRevB.35.8113 (visited on 12/03/2021).

[115] Hossein Beygi et al. "Surface chemistry of as-synthesized and air-oxidized PbS quantum dots". en. In: *Applied Surface Science* 457 (Nov. 2018), pp. 1–10. ISSN: 01694332. DOI: 10.1016/j.apsusc.2018.06.152. URL: https://linkinghub.elsevier.com/retrieve/pii/S0169433218317197 (visited on 12/16/2020).

[116] Changming Fang et al. "Energetics of Polar and Nonpolar Facets of PbSe Nanocrystals from Theory and Experiment". en. In: *ACS Nano* 4.1 (Jan. 2010), pp. 211–218. ISSN: 1936-0851, 1936-086X. DOI: 10.1021/nn9013406. URL: https://pubs.acs.org/doi/10.1021/nn9013406 (visited on 12/16/2020).

[117] Clive R. Bealing et al. "Predicting Nanocrystal Shape through Consideration of Surface-Ligand Interactions". en. In: *ACS Nano* 6.3 (Mar. 2012), pp. 2118–2127. ISSN: 1936-0851, 1936-086X. DOI: 10.1021/nn3000466. URL: https://pubs.acs.org/doi/10.1021/nn3000466 (visited on 12/28/2020).

[118] Donghun Kim et al. "Impact of Stoichiometry on the Electronic Structure of PbS Quantum Dots". en. In: *PHYSICAL REVIEW LETTERS* (2013), p. 5.

[119] Moonsub Shim and Philippe Guyot-Sionnest. "Permanent dipole moment and charges in colloidal semiconductor quantum dots". en. In: *The Journal of Chemical Physics* 111.15 (Oct. 1999), pp. 6955–6964. ISSN: 0021-9606, 1089-7690. DOI: 10.1063/1.479988. URL: http://aip.scitation.org/doi/10.1063/1.479988 (visited on 02/07/2023).

[120] Bogdan Diaconescu et al. "Measurement of Electronic States of PbS Nanocrystal Quantum Dots Using Scanning Tunneling Spectroscopy: The Role of Par-

ity Selection Rules in Optical Absorption". en. In: *Physical Review Letters* 110.12 (Mar. 2013), p. 127406. ISSN: 0031-9007, 1079-7114. DOI: 10.1103/PhysRevLett.110.127406. URL: https://link.aps.org/doi/10.1103/PhysRevLett.110.127406 (visited on 02/28/2022).

[121] Stephen W. Clark, Jeffrey M. Harbold, and Frank W. Wise. "Resonant Energy Transfer in PbS Quantum Dots". en. In: *The Journal of Physical Chemistry C* 111.20 (May 2007), pp. 7302–7305. ISSN: 1932-7447, 1932-7455. DOI: 10.1021/jp0713561. URL: https://pubs.acs.org/doi/10.1021/jp0713561 (visited on 12/16/2020).

[122] G. Allan and C. Delerue. "Confinement effects in PbSe quantum wells and nanocrystals". en. In: *Physical Review B* 70.24 (Dec. 2004), p. 245321. ISSN: 1098-0121, 1550-235X. DOI: 10.1103/PhysRevB.70.245321. URL: https://link.aps.org/doi/10.1103/PhysRevB.70.245321 (visited on 09/14/2022).

[123] Nuri Yazdani et al. "Size, Ligand, and Defect-Dependent Electron–Phonon Coupling in Chalcogenide and Perovskite Nanocrystals and Its Impact on Luminescence Line Widths". en. In: *ACS Photonics* 7.5 (May 2020), pp. 1088–1095. ISSN: 2330-4022, 2330-4022. DOI: 10.1021/acsphotonics.0c00034. URL: https://pubs.acs.org/doi/10.1021/acsphotonics.0c00034 (visited on 07/30/2021).

[124] C. Delerue, M. Lannoo, and G. Allan. "Concept of dielectric constant for nanosized systems". en. In: *Physical Review B* 68.11 (Sept. 2003), p. 115411. ISSN: 0163-1829, 1095-3795. DOI: 10.1103/PhysRevB.68.115411. URL: https://link.aps.org/doi/10.1103/PhysRevB.68.115411 (visited on 09/16/2022).

[125] Nuri Yazdani et al. "Hole Mobility in Nanocrystal Solids as a Function of Constituent Nanocrystal Size". en. In: *The Journal of Physical Chemistry Letters* 5.20 (Oct. 2014), pp. 3522–3527. ISSN: 1948-7185, 1948-7185. DOI: 10.

1021/jz5015086. URL: https://pubs.acs.org/doi/10.1021/jz5015086 (visited on 08/25/2021).

[126] Jun Yang and Frank W. Wise. "Effects of Disorder on Electronic Properties of Nanocrystal Assemblies". en. In: *The Journal of Physical Chemistry C* 119.6 (Feb. 2015), pp. 3338–3347. ISSN: 1932-7447, 1932-7455. DOI: 10.1021/jp5098469. URL: https://pubs.acs.org/doi/10.1021/jp5098469 (visited on 08/25/2021).

[127] Yuan Yu et al. "Chalcogenide Thermoelectrics Empowered by an Unconventional Bonding Mechanism". en. In: *Advanced Functional Materials* 30.8 (Feb. 2020), p. 1904862. ISSN: 1616-301X, 1616-3028. DOI: 10.1002/adfm.201904862. URL: https://onlinelibrary.wiley.com/doi/10.1002/adfm.201904862 (visited on 12/04/2022).

[128] Yudong Cheng et al. "Understanding the Structure and Properties of Sesqui-Chalcogenides (i.e., V $_2$ VI $_3$ or Pn $_2$ Ch $_3$ (Pn = Pnictogen, Ch = Chalcogen) Compounds) from a Bonding Perspective". en. In: *Advanced Materials* 31.43 (Oct. 2019), p. 1904316. ISSN: 0935-9648, 1521-4095. DOI: 10.1002/adma.201904316. URL: https://onlinelibrary.wiley.com/doi/10.1002/adma.201904316 (visited on 05/10/2022).

[129] B. Kiran et al. "(PbS) $_{32}$: A baby crystal". en. In: *The Journal of Chemical Physics* 136.2 (Jan. 2012), p. 024317. ISSN: 0021-9606, 1089-7690. DOI: 10.1063/1.3672166. URL: http://aip.scitation.org/doi/10.1063/1.3672166 (visited on 03/17/2021).

[130] Jean-Yves Raty and Matthias Wuttig. "The interplay between Peierls distortions and metavalent bonding in IV–VI compounds: comparing GeTe with related monochalcogenides". en. In: *Journal of Physics D: Applied Physics* 53.23 (June 2020), p. 234002. ISSN: 0022-3727, 1361-6463. DOI: 10.1088/1361-6463/ab7e66. URL: https://iopscience.iop.org/article/10.1088/1361-6463/ab7e66 (visited on 12/04/2022).

[131] Yudong Cheng, Sophia Wahl, and Matthias Wuttig. "Metavalent Bonding in Solids: Characteristic Representatives, Their Properties, and Design Options". en. In: *physica status solidi (RRL) – Rapid Research Letters* 15.3 (Mar. 2021), p. 2000482. ISSN: 1862-6254, 1862-6270. DOI: 10.1002/pssr.202000482. URL: https://onlinelibrary.wiley.com/doi/10.1002/pssr.202000482 (visited on 12/04/2022).

[132] Roald Hoffmann. "How Chemistry and Physics Meet in the Solid State". en. In: *Angewandte Chemie International Edition in English* 26.9 (Sept. 1987), pp. 846–878. ISSN: 0570-0833, 1521-3773. DOI: 10.1002/anie.198708461. URL: https://onlinelibrary.wiley.com/doi/10.1002/anie.198708461 (visited on 06/09/2022).

[133] Jian-xin Ma et al. "The geometric and electronic properties of the PbS, PbSe and PbTe (001) surfaces". en. In: *Surface Science* 551.1-2 (Feb. 2004), pp. 91–98. ISSN: 00396028. DOI: 10.1016/j.susc.2003.12.003. URL: https://linkinghub.elsevier.com/retrieve/pii/S0039602803014845 (visited on 12/16/2020).

[134] L. P. Bouckaert, R. Smoluchowski, and E. Wigner. "Theory of Brillouin Zones and Symmetry Properties of Wave Functions in Crystals". en. In: *Physical Review* 50.1 (July 1936), pp. 58–67. ISSN: 0031-899X. DOI: 10.1103/PhysRev.50.58. URL: https://link.aps.org/doi/10.1103/PhysRev.50.58 (visited on 09/23/2021).

[135] C. J. Bradley. "The mathematical theory of symmetry in solids : representation theory for point groups and space groups / by C.J. Bradley and A.P. Cracknell." eng. In: (Jan. 2010). Publisher: Clarendon Press. ISSN: 9780191576898.

[136] Hermann Weyl. "The theory of groups and quantum mechanics / by Hermann Weyl ; translated from the 2d rev. German ed. by H.P. Robertson." eng. In: (Jan. 1950). Publisher: Dover Publications. ISSN: 0486602699.

[137] George F. Koster. "Properties of the thirty-two point groups / George F. Koster [and others]." eng. In: (Jan. 1963). Publisher: M.I.T. Press.

[138] Michael Tinkham. *Group theory and quantum mechanics*. English. Dover Books on Chemistry Ser. Mineola, N.Y.: Dover Publications, 2003. ISBN: 978-1-62198-593-8 978-0-486-43247-2 978-0-486-13166-5. URL: http://app.knovel.com/hotlink/toc/id:kpGTQM000L/group-theory-and (visited on 02/15/2023).

[139] Zamin Mamiyev and Narmina O. Balayeva. "PbS nanostructures: A review of recent advances". en. In: *Materials Today Sustainability* 21 (Mar. 2023), p. 100305. ISSN: 25892347. DOI: 10.1016/j.mtsust.2022.100305. URL: https://linkinghub.elsevier.com/retrieve/pii/S258923472200197X (visited on 02/15/2023).

[140] A. Otero-de-la-Roza, Erin R. Johnson, and Víctor Luaña. "Critic2: A program for real-space analysis of quantum chemical interactions in solids". en. In: *Computer Physics Communications* 185.3 (Mar. 2014), pp. 1007–1018. ISSN: 00104655. DOI: 10.1016/j.cpc.2013.10.026. URL: https://linkinghub.elsevier.com/retrieve/pii/S0010465513003718 (visited on 02/07/2023).

[141] *VASP - Vienna Ab initio Simulation Package*. URL: https://www.vasp.at/ (visited on 01/31/2023).